UNIVERSITY OF CALIFORNIA, SAN DIEGO

# Quantitative Diffusion Magnetic Resonance Imaging of the Brain: Validation, Acquisition, and Analysis

A dissertation submitted in partial satisfaction of the requirements of the degree Doctor of Philosophy

in

Cognitive Science

by

Nathan S. White

Committee in charge:

Professor Marta Kutas, Chair
Professor Anders Dale, Co-chair
Professor Rick Buxton
Professor Terry Jernigan
Professor Eric Halgren

2010

The Dissertation of Nathan S. White is approved, and it is acceptable in quality and form for publication on microfilm and electronically:

_____

_____

_____

_____
Co-chair

_____
Chair

University of California, San Diego

2010

# DEDICATION

This dissertation is dedication to my parents who taught me never to give up on myself and to always remember the important things in life.

TABLE OF CONTENTS

LIST OF FIGURES

## ACKNOWLEDGEMENTS

It is my pleasure to acknowledge all those that have contributed to this dissertation. I want to start first and foremost by thanking the chair of my committee and principal advisor, Professor Marta Kutas, for her unwavering support and guidance throughout my entire academic career at UCSD. Without her mentorship and generosity over the years, none of this work would have been possible. I truly cannot thank her enough for everything she has done for me.

I also want to thank my technical advisor Professor Anders Dale who has been the cornerstone of my academic growth over the last five years. Ander's technical guidance and intellectual brilliance have been fundamental to the formation of this dissertation. He's taught me many lessons over the years and I consider his mentorship invaluable. I have nothing but the utmost respect for Anders and I look forward to continued research with him.

I am also indebted to the support of the other members of my committee. In particular, Professor Rick Buxton for his expertise in magnetic resonance imaging principles, and Professor's Eric Halgren and Terry Jernigan for their respective expertise on magnetic resonance imaging applications in brain science. Their input and helpful discussions have also played a key role in the formation of this dissertation.

Last but not least I want to thank all my friends and family that have supported me in life: my father Alan White, my mother, Marja White, my two brothers Ben and Elijah White, and of course the love of my life Kate McNulty. At the end of the day it's been you Kate that's given me the love and support when I needed it most.

Chapter 5, in full, has recently been accepted to the journal PLoS One: *Quantitative Histological Validation of Diffusion MRI Fiber Orientation Distributions in the Rat Brain*, Trygve B. Leergaard, Nathan S. White, Alex de Crespigny, Ingeborg Bolstad, Helen

D'Arceuil, Jan G. Bjaalie, and Anders M. Dale, 2009. The dissertation author was a shared primary investigator and first author of this paper (along with Trygve B. Leergaard).

Chapter 6, in full, is a reprint of the material as it appears in Human Brain Mapping: *Optimal Diffusion MRI Acquisition for Fiber Orientation Density Estimation: An Analytic Approach*, Nathan S. White, and Anders M. Dale, 2009. The dissertation author was the primary investigator and first author of this paper.

Chapter 7, in full, is a reprint of the material as it will appear in the January issue of Magnetic Resonance in Medicine, 2010, entitled: *PROMO: Real-time Prospective Motion Correction in MRI using Image-based Tracking.* Nathan White, Cooper Roddey, Ajit Shankaranarayanan, Eric Han, Dan Rettmann, Juan Santos, Josh Kuperman, and Anders Dale. The dissertation author was the primary investigator and first author of this paper.

Chapter 8, in full, is part of a presentation at the 17$^{th}$ Annual Meeting of the International Society of Magnetic Resonance in Medicine (ISMRM) in 2009, entitled: *"Restriction Spectrum Imaging (RSI): A New Approach for Resolving Complex Tissue Microstructures with Diffusion MRI"*, Nathan White, Trygve B. Leergaard, Alex de Crespigny, and Anders Dale. The dissertation author was the primary investigator and first author of this abstract, and the material is currently being prepared for submission for publication.

# VITA

| | |
|---|---|
| 1999 | Bachelor of Science, Boston University. |
| 2002 | Medical Product Development Certificate Program<br>University of California, Irvine – Extension |
| 1999 - 2003 | Staff Research Associate, University of California, Irvine |
| 2003 - 2004 | Research Assistant, Massachusetts General Hospital,<br>Harvard University |
| 2010 | Doctor of Philosophy, University of California, San Diego |

## US PATENTS

"Dynamic motion estimation using hidden markov model processing and implementations in motion insensitive magnetic resonance imaging (MRI) and other applications." Nathan S. White, Anders M. Dale. US provisional patent application: SD 2006-154. Filed April 13, 2006.

## SELECTED PUBLICATIONS

N.S. White, A.M. Dale. Optimal diffusion MRI acquisition for fiber-orientation density estimation: an analytic approach. Hum Brain Mapp. 2009 Nov;30(11):3696-703

Trygve B. Leergaard[†], Nathan S. White[†], Alex de Crespigny, Ingeborg Bolstad, Helen D'Arceuil, Jan G. Bjaalie, Anders M. Dale. Quantitative histological validation of diffusion MRI fiber orientation distributions in the rat brain. PLoS One. 2009. *In press*. [†] shared first author.

Nathan White, Cooper Roddey, Ajit Shankaranarayanan , Eric Han, Dan Rettmann, Juan Santos, Josh Kuperman, and Anders Dale. PROMO: real-time prospective motion correction in MRI using image-based tracking. Magn Reson Med. 2009. *In press*.

N.S. White,T.B. Leergaard, I. Bolstad, J.G. Bjallie, H.D'Arceuil, A. de Crespigny, A.M. Dale. Quantitative Histological Validation of Fiber-orientation Distributions Based on High-angular Resolution Diffusion Imaging. ISMRM, May 2008, Toronto, Canada.

A. Shankaranarayanan, E. T. Han, C. Roddey, N. White, R. Busse, J. Kuperman, J. Santos, D. Rettmann, E. Schmidt and A. Dale. Motion insensitive 3D T2 and T1-weighted imaging with a real-time, image-based PROspective MOtion correction technique (3D PROMO) and automated re-acquisition of motion-corrupted k-space segments. ISMRM, May 2008, Toronto, Canada.

J.C. Roddey, A. Shankaranarayanan, E. T. Han, N.S. White, A.M. Dale. Motion insensitive imaging using 3D PROspective MOtion (PROMO) correction with region-of-interest tracking. ISMRM, May 2008, Toronto, Canada.

N. S. White, A. Shankaranarayanan, E. T. Han, A. Gaddipati, C. Roddey, and A. M. Dale. Prospective Motion Correction using Non-linear Predictive Filtering. Joint Annual Meeting ISMRM-ESMRMB, May 2007

Shankaranarayanan, C. Roddey, N. White, E. T. Han, D. Rettmann, J. Santos, E. Schmidt, A. Dale. Motion Insensitive 3D Imaging using a Novel Real-Time Image-based 3D PROspective MOtion Correction Method (3D PROMO). Joint Annual Meeting ISMRM-ESMRMB, May 2007

White, N.S., Alkire, M.T., Haier, R.J. A voxel-based morphometric study of non-demented adults with down syndrome. NeuroImage 2003 Sep;20(1):393-403

White, N.S., Alkire, M.T. Impaired thalamocortical connectivity in humans during general anesthetic-induced unconsciousness. NeuroImage 2003 Jun;19(2):402-411

# FIELDS OF STUDY

Major Fields: Biomedical Engineering, Magnetic Resonance Imaging, Cognitive Science.

Studies in Biomedical Signal Processing
Professors Paolo Bonato and Carlo J. De Luca

Studies in Magnetic Resonance Imaging
Professor Anders M. Dale

Studies in Cognitive Neuroscience
Professors Marta Kutas and Dr. Michael T. Alkire

ABSTRACT OF DISSERTATION

# Quantitative Diffusion Magnetic Resonance Imaging of the Brain: Validation, Acquisition, and Analysis

by

Nathan S. White

Doctor of Philosophy in Cognitive Science

University of California, San Diego, 2010

Professor Marta Kutas, Chair

Professor Ander Dale, Co-chair

Owing to its exquisitely sensitive contrast mechanism, diffusion magnetic resonance imaging is a powerful non-invasive approach for studying the microstructural properties of the human brain in vivo. Magnetic resonance images are made sensitive to the microscopic displacements of water molecules that take place in brain tissue as part of the natural, physical diffusion process. Tissue water is used as an intrinsic probe, revealing important clues into the subtle architectural features of normal and pathologic brain tissue. Typical inferences include the intravoxel orientation distribution of neuronal fibers and changes in diffusion resulting

from cell swelling in acute stroke. However, despite the many important advances made in the field of diffusion magnetic resonance imaging over the past decade, quantitative inference in the human brain remains somewhat limited due to the lack of direct quantitative validation against realistic biological architectures and practical limitations in data collection due to sub-optimal design parameters and artifacts caused by patient motion during scanning. In addition, current methods to resolve neuronal fiber orientations are unable to disambiguate fiber structures at different microscopic length (size) scales. In this dissertation I present a series of studies addressing each of these important limitations, starting with a general real-time image-based technique for motion correction in magnetic resonance images and ending with a series of studies on inferring complex fiber orientations from diffusion data, addressing issues such as quantitative histological validation, optimal acquisition, and improved multi-scale analysis.

# Chapter 1

# Introduction

## 1.1 Introduction

The human brain is an immensely complex organ, containing over 10 billion neurons with each neuron forming roughly 10,000 connections with other neurons. Biomedical imaging has become a powerful approach to sort through this maze of information and provide insight into the intrinsically complex functional and structural properties of the brain. Magnetic resonance imaging (MRI) in particular is an increasingly popular imaging modality because it allows for non-invasive, in vivo assessment of the entire brain in a matter of minutes. By using the natural diffusion-driven displacements of water molecules as an intrinsic probe, magnetic resonance imaging of water diffusion, called diffusion MRI, provides researchers and clinicians with an unparalleled view of the fine architectural features of both normal and pathologic brain tissue.

Yet despite the tremendous advances made in the field of diffusion MRI over the last decade, a number of important research questions remain unanswered. Specifically, how well can the microscopic displacements of water molecules, as assessed with diffusion MRI, be used to estimate complex neuronal fiber orientations compared with gold standard histological techniques, especially in regions with complex tissue geometries? Furthermore, can these

measures be obtained in a reasonable amount of time on today's clinical MRI machines, and if so, what is the most efficient way to do so? Are there any alternative analysis strategies for obtaining more informative quantitative biomarkers of tissue microstructure from diffusion MRI measures? And finally, given the well-known practical limitations of patient head motion during MRI scans, especially during scans that are made sensitive to the microscopic motion of tissue water, are there more efficient methods for mitigating the detrimental effects of patient motion during MRI scans in general? The work presented in this dissertation will provide at least some preliminary answers to all these questions.

## 1.2 Research Summary

This dissertation is divided into three main parts. In Part I (Chapters 2-4) I provide a basic overall introduction to the field of diffusion nuclear magnetic resonance (NMR) and magnetic resonance imaging (MRI) (Chapter 2), the fundamental physical principles governing the approach (Chapter 3), and a brief synopsis of some of the most current state-of-the-art diffusion MRI techniques (Chapter 4). Having established the requisite historical and technical background on the subject, in Part II (Chapter 5-7) I present the work that I view as the major contribution of this dissertation.

In the first chapter of Part II (Chapter 5) my colleagues and I quantitatively compared and validated the extent to which complex neuronal fiber orientations can be derived from diffusion MRI measures using gold standard histological techniques in ex vivo rat brain tissue. Having validated the measures, in the next chapter (Chapter 6) we address the question of what is the most efficient clinical MRI scan protocol that can be used to derive these neuronal fiber orientations in vivo. Finally, in the last chapter of Part II (Chapter 7), my colleagues and

I describe a novel real-time motion compensation technique for obtaining MRI scans in vivo that are insensitive to patient motion during the scan acquisition.

In the final Part III (Chapter 8) of this dissertation, I describe a novel and preliminary analysis strategy for diffusion MRI scans that can be used to resolve and disambiguate neuronal fiber orientations at various microscopic length-scales. I view this later work as an initial step towards bridging the gap between the classic material science application of diffusion NMR to quantify the morphology of various porous materials (pore sizes, spacing, etc), and today's wide-spread application of diffusion MRI to resolve the orientation structure of brain tissue in vivo.

## 1.3 Original Contributions

In his doctoral dissertation at Harvard University and Massachusetts Institute of Technology, David Tuch wrote a wonderful brief history of diffusion nuclear magnetic resonance and magnetic resonance imaging, which inspired me to start with a similar introduction to this dissertation (Chapter 2).

Chapter 5 was performed in conjunction with colleagues at the University of Oslo, Norway (Trygve B. Leergaard, Ingeborg Bolstad, and Jan G. Bjaalie), and Harvard University (Alex de Crespigny and Helen D'Arceuil). Alex de Crespigny and Helen D'Arceuil collected the original datasets, while Trygve B. Leergaard, Ingeborg Bolstad, and Jan G. Bjaalie, conducted the stereological analysis of the histology data. I conducted the MR image analysis and Trygve B. Leergaard and I shared responsibility for production of the manuscript, which appears in the journal PLoS One, entitled: "*Quantitative Histological Validation of diffusion MRI Fiber Orientation Distributions*".

Chapter 6 is a theoretical paper conceived by my advisor (Anders Dale) and I, which can be found published in the journal Human Brain Mapping, entitled: *"Optimal Diffusion MRI Acquisition for Fiber Orientation Density Estimation: An Analytic Approach"*.

Chapter 7 was performed in collaboration with colleagues at General Electric Inc. (Ajit Shankaranarayanan, Eric Han, and Dan Rettmann), and Stanford University (Juan Santos), as well as members of our own lab (Cooper Roddey and Josh Kuperman). Ther spiral navigator pulse-sequence and real-time communication code was written by Ajit Shankaranarayanan, Eric Han, Dan Rettmann, and Juan Santos. The motion tracking procedure was originally conceived and tested by my advisor (Anders Dale) and I. Cooper Roddey was responsible for the C implementation of the motion tracking code, and Josh Kuperman help collect much of the imaging data. I was responsible for production of the manuscript, which can be found in the journal Magnetic Resonance in Medicine, entitled: *"PROMO: Real-Time Prospective Motion Correction in MRI Using Image-based Tracking"*.

Chapter 8 is an extension of the abstract I submitted to the 17$^{th}$ Annual Meeting of the International Society of Magnetic Resonance in Medicine in 2009, entitled: *"Restriction Spectrum Imaging (RSI): A new Method for Resolving Complex Tissue Microstructures in Diffusion MRI"*.

# Chapter 2

# A Historical Note

## 2.1 Brownian Motion

In his seminal paper entitled “A brief account of microscopical observations made in the months of June, July, and August 1827 on the particles contained in the pollen of plants, and on the general existence of active molecules in organic and inorganic bodies”, the Scottish botanist Robert Brown reported observing the seemingly “random oscillatory motion” of pollen grains of *Clarkia pulchella* suspended in water when viewed under the microscope (1). While he initially hypothesized this peculiar behavior must somehow be specific to the male sexual cells of plants, similar observations made later using inorganic materials such as fragments of glass and very small rocks compelled him to conclude that this seemingly random dance was rather a general property of all particles suspended in solution. The physical basis of such Brownian motion remained a mystery until the mid to late $19^{th}$ century, when a general kinetic theory of matter began to emerge, the pioneers of which included the minds of Rudolf Claussius, James Maxwell and Ludwig Boltzmann. Together, they proposed the radical idea that such Brownian motion was actually driven by thermal energy, and vis-à-vis particle motions in solution are manifest as heat.

It wasn't until the early part of the 20th century when Albert Einstein, apparently unaware of Brown's earlier observations and eager to prove the existence of all atoms, derived the important statistical laws governing such a kinetic theory (2). His laws, which were also independently formulated by Marian Smoluchowski around the same time (3), not only accounted for the temperature and viscosity of the solution, but also the size of the particles. In his work Einstein combined what was known about thermodynamics and statistical mechanics at the time to obtain the first experimentally testable theory for Brownian motion. Some four years later in 1909 the French physicist Jean Baptist Perrin performed the seminal experiments validating Einstein's theory and proving once and for all the existence of atoms, work which later earned him the Nobel Prize in physics 1926. The macroscopic behavior of Brownian motion as formulated by Einstein is the physical process known today as diffusion.

## 2.2 Diffusion NMR

The phenomenon of nuclear magnetic resonance (NMR) was first discovered in 1946 by the seminal works of Block, Hanson and Packard (4), and Purcell, Torrey, and Pound (5). Together they observed that when certain atomic nuclei[1] are placed in a magnetic field, they begin to align with and rotate around the applied magnetic field with a frequency of precession proportional to the field strength, the so called "Larmor frequency". Block, Hanson and Packard demonstrated how the oscillating nuclei absorb electromagnetic energy when delivered at the Larmor frequency, while Purcell, Torrey, and Pound demonstrated how the nuclei re-emit this energy when in the process of returning to their equilibrium state. Four years later, Hahn published a seminal paper (6) on the formation of NMR spin echos, in which

[1] Specifically, any nucleus with an odd number of protons and or neutrons which results in an intrinsic magnetic moment and angular momentum called "spin".

he showed how the phase incoherence of precessing nuclei in the presence of magnetic field inhomogeneities could be recovered using a 180° radio-frequency (RF) pulse. In so doing, Hahn noted that only part of the signal could be recovered due to the diffusion of spins to a different location along the magnetic field. Car and Purcell (7) later quantified the expected NMR spin echo attenuation due to discrete changes in spin position, and this was extended to continuous diffusion description by Torrey (8), in what is now know as the Block-Torrey equation.

In 1965, Stejskal and Tanner developed an experimental framework to directly read out the diffusion function using a pair of pulsed gradient magnetic fields before and after application of Hahn's 180° refocusing pulse (9). This opened the door for a wide range of studies over the next twenty years aimed at studying the molecular self-diffusion properties of both non-biological (10-13) and biological materials (14-17). In the early 1990's Cory (18) and Callaghan (19) began to observe diffraction-like effects in porous materials at high diffusion wavelengths, as predicted by the original diffusion propagator formalism of Stejskal (11). These diffraction-like effects demonstrated how the morphology of porous materials (pore size, shape, etc) could be inferred through NMR "q-space" measurements (20).

## 2.3 Diffusion MRI

In 1973 a chemist at the State University of New York at Stony Brook named Paul Lautebur published a short paper in the journal *Nature*[2] entitled "Image formation by induced local interactions: examples employing nuclear magnetic resonance" (21). In it, he described how to separate NMR signals from different spatial locations in the sample by superimposing

[2] The paper was originally rejected by the editor for not having a sufficiently broad appeal for acceptance into the journal *Nature*.

a small magnetic field gradient on top of the main magnetic field. Owing to the Larmor principle, this procedure thus labeled the position of the nuclei with their variable resonant frequencies. Armed with this simple, yet elegant Fourier encoding strategy, Lautebur was able to demonstrate the formation of NMR images, which today are known throughout the medical community as magnetic resonance images, or MRIs.

Soon after Lauebur's discovery, in 1977 Peter Mansfield at the University of Nottingham in England, developed a technique for rapid magnetic resonance imaging called echo-planar imaging (EPI), which required only one signal excitation per image, reducing the scan time by orders of magnitude (22). Then, following the formal conceptualization and demonstration of diffusion MRI by Taylor and Bushell (23), Denis LeBihan collected the first diffusion images obtained in vivo on both healthy human subjects and patients with neurological disorders using a whole-body 0.5T scanner (24). Years later Michael Moseley and others (25,26) at the University of San Francisco published a historical paper which demonstrated the important clinical significance of diffusion MRI in detecting early cerebral infarct associated with acute stroke.

## 2.4 References

1. Brown R. A brief account on microscopical observations on the particles contained in the pollen of plants and on the general existence of active molecules in organic and inorganic bodies. 1828.

2. Einstein A. Über die von der molekularkinetischen Theorie der Wärme geforderte Bewegung von in ruhenden Flüssigkeiten suspendierten Teilchen. Annalen der Physik 1905;322(8):549-560.

3. Smoluchowski M. Zur kinetischen Theorie der Brownschen Molekularbewegung und der Suspensionen. Ann Phys 1906;326(14):756-780.

4. Bloch F, Hansen WW, Packard M. Nuclear induction. Physical Review 1946;69(3-4):127.

5. Purcell EM, Torrey HC, Pound RV. Resonance Absorption by Nuclear Magnetic Moments in a Solid. Physical Review 1946;69(1-2):37.

6. Hahn EL. Spin Echoes. Physical Review 1950;80(4):580.

7. Carr HY, Purcell EM. Effects of Diffusion on Free Precession in Nuclear Magnetic Resonance Experiments. Physical Review 1954;94(3):630.

8. Torrey HC. Bloch Equations with Diffusion Terms. Physical Review 1956;104(3):563.

9. Stejskal EO, Tanner JE. Spin diffusion measurements: spin echoes in the presence of a time-dependent field gradient. The Journal of Chemical Physics 1965;42(1):288-292.

10. Woessner DE. NMR spin-echo self-diffusion measurements on fluids undergoing restricted diffusion. J Phys Chem 1963;67(6):1365-1367.

11. Stejskal EO. Use of spin echoes in a pulsed magnetic-field gradient to study anisotropic, restricted diffusion and flow. The Journal of Chemical Physics 1965;43(10):3597-3603.

12. Tanner JE, Stejskal EO. Restricted self-diffusion of protons in colloidal systems by the pulsed-gradient, spin-echo method. The Journal of Chemical Physics 1968;49(4):1768-1777.

13. Murday JS, Cotts RM. Self-Diffusion Coefficient of Liquid Lithium. The Journal of Chemical Physics 1968;48(11):4938-4945.

14. Tanner JE. Self diffusion of water in frog muscle. Biophysical Journal 1979;28(1):107-116.

15. Finch ED, Harmon JF, Muller BH. Pulsed NMR measurements of the diffusion constant of water in muscle. Arch Biochem Biophys 1971;147(1):299-310.

16. Cleveland G, Chang D, Hazlewood C, Rorschach H. Nuclear magnetic resonance measurement of skeletal muscle: anisotrophy of the diffusion coefficient of the intracellular water. Biophysical Journal 1976;16(9):1043-1053.

17. Cooper RL, Chang DB, Young AC, Martin CJ, Ancker-Johnson B. Restricted Diffusion in Biophysical Systems: Experiment. Biophysical Journal 1974;14(3):161-177.

18. Cory DG, Garroway AN. Measurement of translational displacement probabilities by NMR: an indicator of compartmentation. Magn Reson Med 1990;14(3):435-444.

19. Callaghan, Macgowan, Packer, Zelaya FO. High-resolution q-space imaging in porous structures. Journal of magnetic resonance 1990;90:177-182.

20. Callaghan PT, Coy A, MacGowan D, Packer KJ, Zelaya FO. Diffraction-like effects in NMR diffusion studies of fluids in porous solids. Nature 1991;351(6326):467-469.

21. Lauterbur PC. Image formation by induced local Interactions: examples employing nuclear magnetic resonance. Nature 1973;242(5394):190-191.

22. Mansfield P. Multi-planar image formation using NMR spin echoes. Journal of Physics C: Solid State Physics 1977;10(3):L55-L58.

23. Taylor DG, Bushell MC. The spatial mapping of translational diffusion coefficients by the NMR imaging technique. Physics in Medicine and Biology 1985;30(4):345-349.

24. Le Bihan D, Breton E, Lallemand D, Grenier P, Cabanis E, Laval-Jeantet M. MR imaging of intravoxel incoherent motions: application to diffusion and perfusion in neurologic disorders. Radiology 1986;161(2):401-407.

25. Moseley ME, Cohen Y, Mintorovitch J, Chileuitt L, Shimizu H, Kucharczyk J, Wendland MF, Weinstein PR. Early detection of regional cerebral ischemia in cats: comparison of diffusion- and T2-weighted MRI and spectroscopy. Magn Reson Med 1990;14(2):330-346.

26. Moseley ME, Kucharczyk J, Mintorovitch J, Cohen Y, Kurhanewicz J, Derugin N, Asgari H, Norman D. Diffusion-weighted MR imaging of acute stroke: correlation with T2-weighted and magnetic susceptibility-enhanced MR imaging in cats. AJNR Am J Neuroradiol 1990;11(3):423-429.

# Chapter 3

# Diffusion MRI Principles

## 3.1 Introduction

In diffusion MRI (dMRI), the microscopic translational motion of water molecules occurring as part of the physical diffusion process is used as an intrinsic probe that can reveal fine geometric and microstructural features of both normal and diseased tissue. In this chapter, I provide a brief review of the basic physical principles of dMRI, starting with molecular diffusion physics and ending with the classic MR experiment through which diffusion is measured, namely the pulsed field gradient spin echo (PGSE) experiment of Stejskal and Tanner (1). The concept of the "diffusion coefficient" and "diffusion propagator" is introduced as well as the distinction between "hindered" and "restricted" diffusion processes in neural tissue. Terms such as the "b-value" and "q-space" are also introduced.

## 3.2 Molecular Diffusion Physics

### 3.2.1 Diffusion coefficient

The basic statistical laws of Brownian motion were laid out in the early 20$^{th}$ century with the seminal works of Einstein (2) and Smoluchowski (3). Together, albeit through

different means, they introduced the important statistical concept of the "displacement distribution" of diffusing particles. The displacement distribution is a macroscopic descriptor of the diffusion process that quantifies the statistical likelihood of observing a given particle displacement over some finite diffusion time Δ. They showed that in a free medium, the displacement distribution is Gaussian with a mean-square displacement given by

$$\left\langle r^2 \right\rangle = 2dD\Delta, \qquad [3.1]$$

where $d = \{1, 2, 3\}$ is the physical dimension of the diffusion space, and $D$ is the classical diffusion coefficient appearing in Fick's first law (4). The diffusion coefficient takes into account the temperature and viscosity of the medium as well as the mass of the particles on their average displacement. The Einstein-Smoluchowski relation in Eq. [3.1] asserts that if one were to release all the particles at some origin in three-dimensional space ($d$ = 3) at time zero, after some time Δ, one can expect to find about 68% of them (or one standard deviation) within a sphere of radius $r = \sqrt{6D\Delta}$, centered at the origin. Note that the physics of diffusion makes no distinction between the diffusing particles and the suspended medium, and thus the same diffusion theory applies for particles diffusing in their own medium, such as water diffusing in water – a process known as self-diffusion.

### 3.2.2 Water diffusion in neural tissue

At normal brain temperatures (37° C), the diffusion coefficient $D$ of free water is approximately $3 \times 10^{-3}$ mm$^2$ s$^{-1}$, which translates into a root mean-squared displacement $r$ along one dimension of approximately 17 μm in 50 ms. However, in neural tissue, during their

diffusion-driven displacements, water molecules constantly collide with, bounce off, and interact with various obstacles, such as neuronal fibers, cell membranes, and large macromolecules. The net effect of these obstacles is to not only reduce their overall root mean-squared displacement compared to free water, but to cause their displacement distribution to vary as a function of direction in which it is measured. Thus, while free water diffusion is *isotropic*, water diffusion in neuronal tissue is *anisotropic* with a displacement distribution that is no longer Gaussian. Yet it is this complex diffusion behavior and directional anisotropy that ultimately provides the inferential power through which subtle geometric and microstructural features can be derived from the diffusion measures. That is to say, if the water displacement distributions were trivial, they wouldn't carry much information about their local environment.

### 3.2.3 Hindered and restricted diffusion

A single volume element (voxel) in a typical diffusion MR image is on the order of ~10-30 $mm^3$, and will therefore contain thousands if not hundreds of thousands of cells and various tissue components depending on its location in the brain. As mentioned above, water diffusion in this space is highly complex and will depend on many factors including the viscosity, composition, geometry, and permeability of each compartment (axons, dendrites, cell bodies, etc.). At very short times scales, viscosity and composition play the dominant role in the diffusion displacements, while at long time scales geometry and permeability start to dominate, as the diffusing molecules are allowed time to probe their environment. It is generally thought that the reduced mean-squared displacement of water molecules in neural tissue compared to free water can be attributed to increased viscosity, macromolecular crowding, and restriction effects for intracellular water (5)

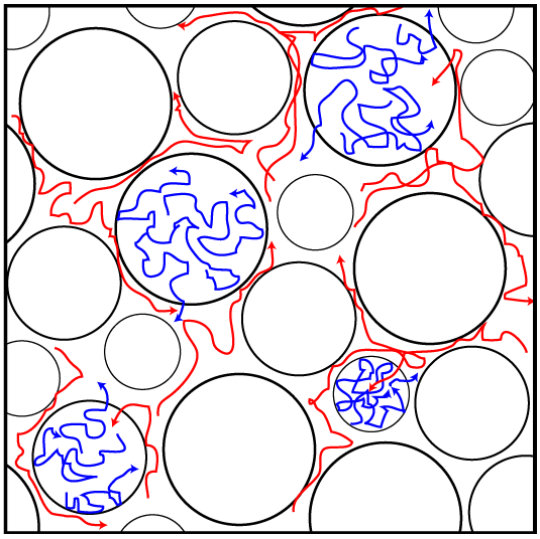

**Figure 3.1**. Diffusion in biological tissue is impeded by tissue components. In the extracellular space (red), tissue components provide an overall hindrance to water diffusion resulting in an increased tortuosity of their paths. In the intracellular space (blue), water diffusion is mainly restricted by cell membranes, although some effect of exchange between the compartments may persist.

and increased tortuosity effects for extracellular water (6-8). An increased tortuosity to water diffusion in the extracellular space is consistent with the view that cellular components provide an overall *hindrance* to diffusing molecules in this space, rather than a *restriction*, which makes sense given the prevailing notion of the brain's extracellular space as an important communication channel between nerve cells allowing water, nutrients, electrolytes, etc. to navigate between cells without getting trapped per se. Cell membranes on the other hand provide restrictions to diffusing water such that their mean-squared displacement becomes invariant to the diffusion time at long $\Delta$ (neglecting for the moment the effect of exchange). Thus, at long $\Delta$, the mean-squared displacement of intracellular water provides information on compartment sizes (9), and has been used as a surrogate measure of axon diameters (10). However, so far, evidence of restricted diffusion in vivo remains elusive (11,12), which may be due in part to the effects of exchange (12) and in part due to hardware limitations of most clinical MRI scanners.

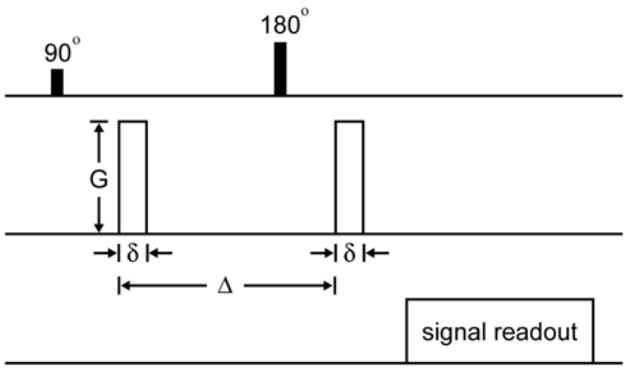


**Figure 3.2**. Stejskal-Tanner pulsed gradient spin echo (PGSE) experiment.

## 3.3 Diffusion MRI Measurement

### 3.3.1 Pulsed gradient spin echo experiment

The classic diffusion MRI experiment is the pulsed gradient spin echo (PGSE) experiment pioneered by Stejskal and Tanner in 1965 (1). The basic idea is to magnetically label the hydrogen protons (spins) carried by water molecules at some initial time zero and then try to undo the effects of the label at some later time Δ. The extent to which the label *can't* be reversed is related to their net displacement, and thus can be used to measure the apparent diffusion coefficient (ADC) in tissue. The term "apparent diffusion coefficient" was originally introduced by Le Bihan (13) to highlight the fact that the measured diffusion coefficient in neural tissue may include contributions from other biological processes such as perfusion.

To measure diffusion, the PGSE experiment builds on the classic Hahn spin-echo sequence (14) to include a pair of gradient pulses with a magnitude *G* and duration δ before and after the 180° refocusing RF pulse (Fig 3.2). After an initial 90° pulse excites the spins into phase (Fig. 3.3a), the first gradient pulse is applied, which encodes the position of the spins along the gradient with a particular phase offset relative to each other (Fig. 3.3b).

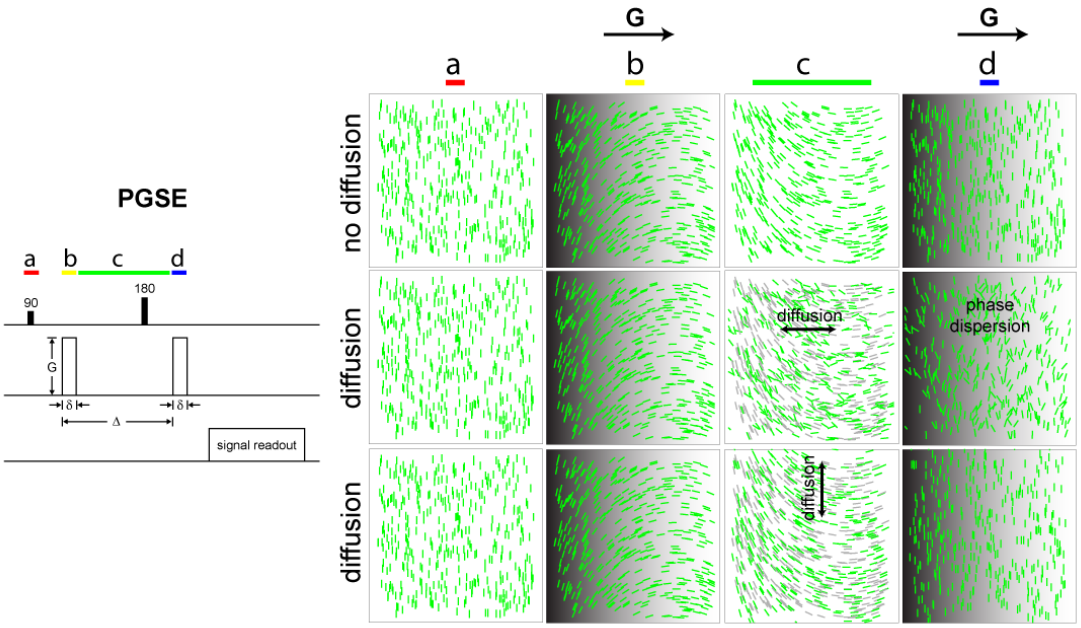


**Figure 3.3**. Spin phase distribution for the PGSE experiment during three hypothetical situations: 1) no diffusion (top row), 2) diffusion parallel to the applied diffusion gradients (middle row), and 3) diffusion perpendicular to the applied diffusion gradients (bottom row). Only diffusion parallel to the gradients during the diffusion time Δ result in a net phase dispersion and an associated signal attenuation.

Then, the spins are allowed to diffuse, during which time a 180° pulse is used to invert their phase and set up the formation of a spin echo (Fig. 3.3c). However, prior to the echo readout, and at time Δ after the start of the first gradient pulse, a second gradient pulse is applied with same magnitude and duration as the first gradient pulse (Fig. 3.3d). This second pulse will "rewind" the phase of the first, provided the spins remained in their original location at the time of encoding. If not, and the spins moved incoherently (i.e. diffused) to a different location along the gradient, then a net phase incoherence will result, reducing the echo amplitude and causing a net signal attenuation. Note that a coherent flow along the gradient would result in a net phase offset, rather than an overall phase dispersion. Note also that the echo attenuation results only from the vector component of diffusion that takes place along the gradient direction (Fig 3.3).

The degree of signal attenuation for a single isotropic Gaussian spin ensemble with diffusion coefficient *D* is given by the well-known Stejskal-Tanner equation (1)

$$S / S_0 = e^{-\gamma^2 G^2 \delta^2 (\Delta - \delta/3) D} = e^{-bD}, \qquad [3.2]$$

where $S / S_0$ is the normalized signal attenuation, $S_0$ is the signal measured in the absence of any gradients ($G = 0$), $\gamma$ is the gyromagnetic ratio of protons, and $b = \gamma^2 G^2 \delta^2 \left(\Delta - \delta/3\right)$ is called the diffusion weighting factor, or "b-value" (13). Conceptually, the b-value controls the overall degree of diffusion sensitivity (expected degree of signal loss), which is dependent on the strength of the initial phase labeling $\gamma^2 G^2 \delta^2$, and the effective time allotted for the spins to diffuse $\left(\Delta - \delta / 3\right)$.

### 3.3.2 Fourier relationship and the ensemble average propagator

The classic Stejskal-Tanner equation in Eq. [3.2] allows one to relate the signal attenuation to the diffusion coefficient of a Gaussian diffusing ensemble of spins through use of the b-value. However, recall that the Gaussian assumption can easily be violated in neuronal tissue due to restriction effects and heterogeneity of tissue components. Recognizing the importance of generalizing their result to the more general case of non-Gaussian diffusion, Stejskal-Tanner also provided an elegant relationship between the spin displacement probability density function $\bar{P}\left(r, \Delta\right)$, also called the "ensemble average propagator" to the normalized signal attenuation (1)

$$S / S_0 = \int \bar{P}(r,\Delta) e^{i\gamma\delta G r} dr, \qquad [3.3]$$

where $\bar{P}(r,\Delta)$ is the probability a spin will experience a net displacement $r$ in time $\Delta$. The average propagator in Eq. [3.3] makes no assumptions on the form of the diffusion process, and reduces to the classic Stejskal-Tanner in Eq. [3.2] when the spin displacement distribution is Gaussian.

### 3.3.3 *q*-Space formalism

Building on the classic pulsed-field gradient spin-echo (PGSE) experiment of Stejskal and Tanner (1), Callaghan (15) and Cory and Garroway (16) proposed to rewrite Eq. [3.3] as a Fourier transform ($F$) with respect to the reciprocal wavevector $q = \gamma G \delta (2\pi)^{-1}$

$$\begin{aligned} S(q) / S_0 &= \int \bar{P}(r,\Delta) e^{-i2\pi q \cdot r} dr \\ &= F\left\{\bar{P}(r,\Delta)\right\}. \end{aligned} \qquad [3.4]$$

This allows one to conceptualize the acquired data as a "q-space" image of the displacement distribution, whose reconstruction can be obtained through simple Fourier inversion of the normalized diffusion signal. However, the Fourier relationship in Eq. [3.3] relies on a few key assumptions. First, the width of the gradient pulses δ is considered to be infinitesimally short, such that the area of the gradient pulse is time-independent and can be approximated as $G\delta$. This condition is called the "narrow pulse field approximation". Second, the diffusion time Δ must be sufficiently longer than δ (Δ>>δ), such that nearly all the spin diffusion takes place during the diffusion time and not during the gradient pulses (cf. Fig 3.2). These assumptions

will be called into question in Chapter 4 when reviewing certain diffusion MRI analysis techniques.

## 3.4 References


1. Stejskal EO, Tanner JE. Spin diffusion measurements: spin echoes in the presence of a time-dependent field gradient. The Journal of Chemical Physics 1965;42(1):288-292.

2. Einstein A. Über die von der molekularkinetischen Theorie der Wärme geforderte Bewegung von in ruhenden Flüssigkeiten suspendierten Teilchen. Annalen der Physik 1905;322(8):549-560.

3. Smoluchowski M. Zur kinetischen Theorie der Brownschen Molekularbewegung und der Suspensionen. Ann Phys 1906;326(14):756-780.

4. Fick A. Concerns diffusion and concentration gradient. Ann Phys Lpz 1855;170(59).

5. Hazlewood CF, Rorschach HE, Lin C. Diffusion of water in tissues and MRI. Magn Reson Med 1991;19(2):214-216.

6. Nicholson C, Phillips JM. Ion diffusion modified by tortuosity and volume fraction in the extracellular microenvironment of the rat cerebellum. J Physiol 1981;321:225-257.

7. Nicholson C, Chen KC, Hrabetova S, Tao L. Diffusion of molecules in brain extracellular space: theory and experiment. Prog Brain Res 2000;125:129-154.

8. Sykova E, Nicholson C. Diffusion in brain extracellular space. Physiol Rev 2008;88(4):1277-1340.

9. Cohen Y, Assaf Y. High b-value q-space analyzed diffusion-weighted MRS and MRI in neuronal tissues - a technical review. NMR Biomed 2002;15(7-8):516-542.

10. Bar-Shir A, Cohen Y. High b-value q-space diffusion MRS of nerves: structural information and comparison with histological evidence. NMR Biomed 2008;21(2):165-174.

11. Le Bihan D, Turner R, Douek P. Is water diffusion restricted in human brain white matter? An echo-planar NMR imaging study. Neuroreport 1993;4(7):887-890.

12. Nilsson M, Latt J, Nordh E, Wirestam R, Stahlberg F, Brockstedt S. On the effects of a varied diffusion time in vivo: is the diffusion in white matter restricted? Magn Reson Imaging 2009;27(2):176-187.

13. Le Bihan D, Breton E, Lallemand D, Grenier P, Cabanis E, Laval-Jeantet M. MR imaging of intravoxel incoherent motions: application to diffusion and perfusion in neurologic disorders. Radiology 1986;161(2):401-407.

14. Hahn EL. Spin Echoes. Physical Review 1950;80(4):580.

15. Callaghan, Macgowan, Packer, Zelaya FO. High-resolution q-space imaging in porous structures. Journal of magnetic resonance 1990;90:177-182.

16. Cory DG, Garroway AN. Measurement of translational displacement probabilities by NMR: an indicator of compartmentation. Magn Reson Med 1990;14(3):435-444.

# Chapter 4

# Diffusion MRI Techniques

## 4.1 Introduction

Diffusion in biological tissue is a complex process. Equally complex is the process of inferring biological information from diffusion MRI (dMRI) measurements. In this chapter, I provide a brief overview of some of today's current state-of-the-art dMRI techniques, what they purport to measure, and some of their advantages and disadvantages. The main goal of this chapter is to provide the requisite background into the specific techniques referenced in the remaining chapters of this dissertation (Chapters 5-8), as well as to provide the motivation for such work.

## 4.2 Diffusion MRI Techniques

Generally speaking, most dMRI techniques fall within one of two categories. The first category of methods attempt to characterize some aspect of the diffusion process, either through measurement of the water displacement probability density function (PDF), also called the ensemble average propagator, or through measurement of the apparent diffusion coefficient (ADC). These methods can be either model-free or model-based. The second category of methods attempt to estimate microstructural features directly through application

of some type of biophysical model for water diffusion in neural tissue. Below I review some popular techniques in both categories.

### 4.2.1 Model-free methods

#### 4.2.1.1 *q*-Space imaging (QSI)

Building on the classical pulsed gradient spin echo experiment (PGSE) of Stejkal and Tanner (1), Callaghan (2) and Cory and Garroway (3) proposed the *q*-space framework to gain insight into the microscopic diffusion properties of complex materials. *q*-Space imaging (QSI) is a model-free (unbiased) method for obtaining the water displacement probability density function (PDF) through Fourier inversion of the normalized diffusion signal, without recourse to a mathematical model for the displacements. It was observed early on that the "diffraction" peaks of the *q*-space signal and the reconstructed displacement PDF for reflecting molecules trapped within simple geometries, such as spheres and cylinders, may (at sufficiently long $\Delta$) be used to derive information on the size and shape of the confinement (4-6). Kuchel and co-workers (7) found similar diffraction-like effects in suspensions of human red blood cells, which were indicative of their cell diameters and intracellular spacing. However, the diffraction peaks were not as sharp as in other porous materials, most likely due to the variability of cell sizes and the effects of exchange between intracellular and extracellular compartments. Diffraction-like peaks resulting from restricted diffusion have yet to be observed in vivo, but King *et al.* (8,9) and Assaf *et al.* (10) demonstrated that other quantities derived from the displacement PDF, such as the root mean-squared displacement or probability of zero displacement still reveal important structural parameters of CNS tissue, such as the compartment size. Today, there remains growing interest in using QSI for studying spinal cord trauma (11,12) and multiple sclerosis (13,14).

The main limitation of *q*-space imaging is an experimental one. Recall the Fourier relationship between the displacement PDF and normalized diffusion signal requires the diffusion sensitizing gradients have an infinitesimally short duration δ (the "narrow pulse field approximation"), and that all the spin diffusion takes place during the diffusion time Δ, rather than during the gradient pulses themselves, i.e. $\delta << \Delta$ (cf. Chapter 3). This subsequently requires very large amplitude gradient pulses with rapid rise times that even the most advanced whole-body (head) gradient systems cannot provide. For this reason, the classic *q*-space framework is primarily limited to ex vivo applications on small bore animal scanners with powerful gradient coils.

#### 4.2.1.2 Diffusion spectrum imaging (DSI)

Diffusion spectrum imaging (DSI) (15) is a model-free technique closely related to conventional QSI, but adapted for three-dimensional (3D) in vivo applications on clinical scanners. In DSI, the diffusion data are acquired on a Cartesian grid in *q*-space, and the 3D water displacement PDF, or "displacement spectrum", is reconstructed for each voxel using the inverse Fourier transform. Rather than use the reconstructed PDF for estimating microstructural features, it is often integrated in the radial direction to obtain a measure that reflects the overall likelihood of water diffusion along any arbitrary solid angle in 3D space. This derived quantity, called the water displacement orientation distribution function (ODF) (16) is often used as a surrogate measure of neuronal fiber orientations (15), and is gaining popularity for in vivo white matter fiber tracking applications (17).

Similar to QSI, the main advantage of DSI is that it provides a model-free description of the diffusion process without recourse to a mathematical model or prior description of the water displacement function. However, in order to resolve the displacement spectrum, DSI

requires collecting hundreds of images on a 3D Cartesian lattice in *q*-space, which increases scan time significantly (several hours for whole brain coverage), and precludes its application for routine clinical use. Also, at a more fundamental level, DSI applies the formalism of conventional QSI without satisfying any of its essential requirements. For example, it's not uncommon for a typical DSI acquisition to have relatively long gradient pulses ($\delta \approx 50$ms) that fill up almost the entire diffusion time, i.e. $\Delta \approx \delta$. This means that essentially all the molecular spin diffusion takes place during the gradient encoding, resulting in a displacement spectrum that reflects a quantity more in line with the center-of-mass propagator (18), rather than the ensemble average propagator. Deriving microstructural information from the displacement spectrum is therefore complicated and warrants careful interpretation (19). With that said, in light of the fact that the center-of-mass propagator can be viewed as a convolved (smoothed) version of the ensemble average propagator (18), the course-scale orientation structure of the displacement spectrum may still be well preserved, and thus the peaks of the ODF may still reflect the general orientation structure of the tissue.

#### 4.2.1.3 *q*-Ball imaging (QBI)

*q*-Ball imaging (QBI) is a model-free approach for recovering the diffusion ODF using measurements collected on the sphere in *q*-space (20). Such spherical acquisitions, also called high angular resolution diffusion imaging (HARDI) acquisitions, require far fewer measurements compared with the lattice sampling of DSI, and thus can reduce the scan time significatly. As such, the *q*-ball technique is generally considered more clinically applicable compared with DSI. While the original *q*-ball technique computes the ODF numerically (20), several recent works (21-24) have used spherical harmonic basis functions to compute the ODF analytically, resulting in a solution that is much faster and more robust to measurement

noise. Furthermore, by truncating the spherical harmonic series and setting an upper limit to the desired angular frequency of the recovered ODF, more specific and efficient reduced spherical encoding strategies can be performed. One important limitation of QBI is that the displacement spectrum itself is not measured, only its angular information via the diffusion ODF, and thus inferring quantitative microstructural parameters of the tissue is limited.

#### 4.2.1.4 Spherical harmonics (SH)

Spherical harmonic (SH) basis functions have also been used to provide a model-free description of the intravoxel apparent diffusion coefficient (ADC) (25,26). Similar to other model-free approaches, the advantage of using a spherical harmonic representation is that it makes no prior assumption on the three-dimensional shape of the ADC, which may become quite complex in voxels containing multiple fiber orientations. However, although this method is classified as being model-free, implicit in the assumption of reconstructing the ADC (albeit with any arbitrary shape), is that the water displacement distribution is treated as Gaussian when measured along an arbitrary solid angle in 3D. This Gaussian assumption is clearly violated if the diffusion measurements are sensitive enough (i.e. with sufficient diffusion weighting) to pick up the slow diffusing water component in the intracellular space which is non-Gaussian due to restricted diffusion (cf. Chapter 3).

### 4.2.2 Model-based Methods

#### 4.2.2.1 Diffusion tensor imaging (DTI)

Diffusion tensor imaging (DTI) (27) is by far the most popular diffusion MRI technique used today. As its name suggests, DTI is a model-based technique that posits a single 3D Gaussian distribution for the ADC, such that an effective diffusion tensor can be

estimated in each voxel. In regions of coherently organized microstructure with a high degree of diffusion anisotropy, such as the myelinated axons of large white matter fiber bundles (28), the principle eigenvector of the reconstructed tensor is a reliable indicator the principle mode of orientation. This observation opened the door for a whole new field of study aimed at mapping white matter fiber tracks throughout the brain (29,30). Scalar quantities derived from the tensor eigenvalues, such as the fractional anisotropy (FA) and mean diffusivity (31,32) also provide an important rotationally invariant scalar description of the diffusion process within voxels. These measures have found widespread application, from studying white matter deficits associated with various psychiatric disorders such as Schizophrenia (33-35), Alzheimer's disease (36,37), and addiction (38,39), to identifying tissue damage associate with the acute and chronic stages of stroke (40-42) and traumatic brain injury (43,44).

Despite its growing popularity and widespread acceptance in the field, DTI is limited by the simplifying assumption of a single Gaussian diffusing component in each voxel. Not only is the Gaussian model inadequate to model the slow and fast diffusing components resulting (presumably) from the intracellular and extracellular space, respectively, but a single tensor cannot capture the complex orientation structure present in heterogeneous tissue, for example in regions where white matter fiber bundles cross.

#### 4.2.2.2 Multi-tensor imaging

Multi-tensor imaging, or the multi-tensor model, is a natural extension to DTI which allows for a finite mixture of diffusion tensors to characterize the intravoxel ADC (16,45). The obvious advantage of multi-tensor imaging is it allows for two or more Gaussian diffusing components to be recovered, and therefore can be used to resolve or separate the orientations of crossing white matter fiber tracks (16,46).

The main disadvantage of the multi-tensor, or Gaussian mixture model, is the number of mixture components must be specified a priori, although some work have been performed using various information criterion to help with the model selection problem (47,48).

#### 4.2.2.3 Spherical deconvolution (SD)

Spherical deconvolution (SD), first purposed by Tournier and colleagues (49) in 2004, is a novel model-based analysis technique for dMRI that is becoming increasingly popular in recent years. Rather than try to model the ADC explicitly, in SD the signal is modeled as stemming from an unknown distribution of *fibers*, each with a fixed three-dimensional Gaussian ADC. Thus, the diffusion signal can be viewed as the convolution of the neuronal fiber orientation distribution (FOD) with the expected signal response from a single "canonical" fiber, or bundle of fibers. This is a slight, but important interpretive shift from previous dMRI techniques, in that the quantity of interest, i.e. the fiber orientation distribution, is estimated directly from the data, rather than hypothesized from the peaks of the ADC or ODF.

Various techniques for estimating the FOD via spherical deconvolution or related approaches exist today (21,50-54). Recent work also suggests that the FOD may outperform the ODF for fiber tracking applications (55), which may not be surprising in light of the view that the ODF is a convolved or "smoothed" version of the FOD (21,55). One disadvantage of the deconvolution approach is that the response function must be chosen a priori, although various data driven approaches for simultaneous estimation of the response function parameters and the FOD do exist (21,56). However, all these approaches make the assumption that the fiber distribution is composed of fiber elements with identical Gaussian diffusion characteristics, regardless of what that might be. However, the Gaussian assumption of water

diffusion for a single canonical nerve fiber does not hold under certain experimental conditions where the measurements become sensitive to the restricted water pool inside the cell.

#### 4.2.2.4 CHARMED model

Assaf *et al*. (57) proposed a "composite hindered and restricted model" (CHARMED) for the diffusion signal in white matter, where water in the extra- and intra-axonal space are modeled as Gaussian (hindered) and non-Gaussian (restricted), respectively. The CHARMED model assumes Neuman's analytic approximation (58) for restricted spins in cylinders under the condition where the narrow pulse field approximation of the *q*-space signal is violated (cf. Chapter 3). The advantage of CHARMED is that by fitting the model for restricted spins, inferences on the axon diameters can be extracted, a feature that incorporated into their new technique called "Axcaliber" (59). However, the Axcaliber method has only been applied ex vivo using small bore systems with extremely powerful gradient coils, and thus it remains unclear to what extent these findings will translate to the in vivo situation. The most recent study employing CHARMED on the human brain in vivo, showed the ability to separate hindered and restricted diffusion components along with their orientations, but did not use the data to infer axon diameter distributions (60).

## 4.3 Present Limitations and Motivation

There has growing interest in the field of diffusion MRI to resolve quantitative measures of tissue microstructure non-invasively. Of particular interest presently, is to use high dimensional diffusion MRI data to extract neuronal fiber orientation distributions (FOD) throughout the brain. While many promising methods have been purposed to estimate FODs

from diffusion measures, direct quantitative validation of the results remain missing. This lack of quantitative validation is addressed in Chapter 5 of this dissertation. Furthermore, provided diffusion MRI-derived FOD measures provide an accurate characterization of the underlying histoarchitecture, it is presently unclear how to optimize the experimental scan protocol on a clinical scanner to maximize the statistical efficiently for deriving the FODs. This is addressed in Chapter 6 of this dissertation. As all in vivo MRI applications are ultimately limited by patient motion, especially when sensitized to the microscopic displacements of water molecules as in diffusion MRI, a robust and efficient method to correct for these motion artifacts is highly desired. In Chapter 7 of this dissertation I describe a novel and general real-time method for obtaining motion insensitive MRI scans. Finally, in Chapter 8 of this dissertation I present some preliminary results of a novel method for deriving FODs at different microscopic length scales, addressing the assumption of a fixed scale ADC used by current spherical deconvolution methods.

## 4.4 References

1. Stejskal EO, Tanner JE. Spin diffusion measurements: spin echoes in the presence of a time-dependent field gradient. The Journal of Chemical Physics 1965;42(1):288-292.

2. Callaghan, Macgowan, Packer, Zelaya FO. High-resolution q-space imaging in porous structures. Journal of magnetic resonance 1990;90:177-182.

3. Cory DG, Garroway AN. Measurement of translational displacement probabilities by NMR: an indicator of compartmentation. Magn Reson Med 1990;14(3):435-444.

4. Coy A, Callaghan PT. Pulsed gradient spin echo nuclear magnetic resonance for molecules diffusing between partially reflecting rectangular barriers. The Journal of Chemical Physics 1994;101(6):4599-4609.

5. Callaghan PT, Coy A, MacGowan D, Packer KJ, Zelaya FO. Diffraction-like effects in NMR diffusion studies of fluids in porous solids. Nature 1991;351(6326):467-469.

6. Callaghan PT. Pulsed-gradient spin-echo NMR for planar, cylindrical, and spherical pores under conditions of wall relaxation. Journal of Magnetic Resonance, Series A 1995;113(1):53-59.

7. Kuchel PW, Coy A, Stilbs P. NMR "diffusion-diffraction" of water revealing alignment of erythrocytes in a magnetic field and their dimensions and membrane transport characteristics. Magn Reson Med 1997;37(5):637-643.

8. King MD, Houseman J, Roussel SA, van Bruggen N, Williams SR, Gadian DG. q-Space imaging of the brain. Magn Reson Med 1994;32(6):707-713.

9. King MD, Houseman J, Gadian DG, Connelly A. Localized q-space imaging of the mouse brain. Magn Reson Med 1997;38(6):930-937.

10. Assaf Y, Mayk A, Cohen Y. Displacement imaging of spinal cord using q-space diffusion-weighted MRI. Magn Reson Med 2000;44(5):713-722.

11. Nossin-Manor R, Duvdevani R, Cohen Y. q-Space high b value diffusion MRI of hemi-crush in rat spinal cord: evidence for spontaneous regeneration. Magn Reson Imaging 2002;20(3):231-241.

12. Nossin-Manor R, Duvdevani R, Cohen Y. Spatial and temporal damage evolution after hemi-crush injury in rat spinal cord obtained by high b-value q-space diffusion magnetic resonance imaging. J Neurotrauma 2007;24(3):481-491.

13. Assaf Y, Chapman J, Ben-Bashat D, Hendler T, Segev Y, Korczyn AD, Graif M, Cohen Y. White matter changes in multiple sclerosis: correlation of q-space diffusion MRI and 1H MRS. Magn Reson Imaging 2005;23(6):703-710.

14. Assaf Y, Ben-Bashat D, Chapman J, Peled S, Biton IE, Kafri M, Segev Y, Hendler T, Korczyn AD, Graif M, Cohen Y. High b-value q-space analyzed diffusion-weighted MRI: application to multiple sclerosis. Magn Reson Med 2002;47(1):115-126.

15. Wedeen VJ, Hagmann P, Tseng WY, Reese TG, Weisskoff RM. Mapping complex tissue architecture with diffusion spectrum magnetic resonance imaging. Magn Reson Med 2005;54:1377-1386.

16. Tuch DS. Diffusion MRI of Complex Tissue Structure. Cambridge, MA: Ph.D. Thesis, Massachusetts Institute of Technology; 2002. 218p p.

17. Wedeen VJ, Wang RP, Schmahmann JD, Benner T, Tseng WY, Dai G, Pandya DN, Hagmann P, D'Arceuil H, de Crespigny AJ. Diffusion spectrum magnetic resonance imaging (DSI) tractography of crossing fibers. Neuroimage 2008;41(4):1267-1277.

18. Mitra PP, Halperin BI. Effects of finite gradient-pulse widths in pulsed-field-gradient diffusion measurements. Journal of Magnetic Resonance, Series A 1995;113(1):94-101.

19. Basser PJ. Relationships between diffusion tensor and q-space MRI. Magn Reson Med 2002;47(2):392-397.

20. Tuch DS. Q-ball imaging. Magn Reson Med 2004;52:1358-1372.

21. Anderson AW. Measurement of fiber orientation distributions using high angular resolution diffusion imaging. Magn Reson Med 2005;54:1194-1206.

22. Descoteaux M, Angelino E, Fitzgibbons S, Deriche R. Regularized, fast, and robust analytical Q-ball imaging. Magn Reson Med 2007;58(3):497-510.

23. Hess CP, Mukherjee P, Han ET, Xu D, Vigneron DB. Q-ball reconstruction of multimodal fiber orientations using the spherical harmonic basis. Magn Reson Med 2006;56(1):104-117.

24. Canales-Rodriguez EJ, Melie-Garcia L, Iturria-Medina Y. Mathematical description of q-space in spherical coordinates: exact q-ball imaging. Magn Reson Med 2009;61(6):1350-1367.

25. Alexander DC, Barker GJ, Arridge SR. Detection and modeling of non-Gaussian apparent diffusion coefficient profiles in human brain data. Magn Reson Med 2002;48(2):331-340.

26. Frank LR. Characterization of anisotropy in high angular resolution diffusion-weighted MRI. Magn Reson Med 2002;47:1083-1099.

27. Basser PJ, Mattiello J, LeBihan D. MR diffusion tensor spectroscopy and imaging. BiophysJ 1994;66(1):259-267.

28. Moseley ME, Cohen Y, Kucharczyk J, Mintorovitch J, Asgari HS, Wendland MF, Tsuruda J, Norman D. Diffusion-weighted MR imaging of anisotropic water diffusion in cat central nervous system. Radiology 1990;176(2):439-445.

29. Mori S, van Zijl PC. Fiber tracking: principles and strategies - a technical review. NMR Biomed 2002;15(7-8):468-480.

30. Basser PJ, Pajevic S, Pierpaoli C, Duda J, Aldroubi A. In vivo fiber tractography using DT-MRI data. Magn Reson Med 2000;44(4):625-632.

31. Basser PJ, Pierpaoli C. Microstructural and physiological features of tissues elucidated by quantitative-diffusion-tensor MRI. J Magn Reson B 1996;111:209-219.

32. Pierpaoli C, Jezzard P, Basser PJ, Barnett A, Di Chiro G. Diffusion tensor MR imaging of the human brain. Radiology 1996;201:637-648.

33. Lim KO, Helpern JA. Neuropsychiatric applications of DTI - a review. NMR Biomed 2002;15(7-8):587-593.

34. Kanaan RA, Kim JS, Kaufmann WE, Pearlson GD, Barker GJ, McGuire PK. Diffusion tensor imaging in schizophrenia. Biol Psychiatry 2005;58(12):921-929.

35. Kumra S, Ashtari M, McMeniman M, Vogel J, Augustin R, Becker DE, Nakayama E, Gyato K, Kane JM, Lim K, Szeszko P. Reduced frontal white matter integrity in early-onset schizophrenia: a preliminary study. Biol Psychiatry 2004;55(12):1138-1145.

36. Bozzali M, Falini A, Franceschi M, Cercignani M, Zuffi M, Scotti G, Comi G, Filippi M. White matter damage in Alzheimer's disease assessed in vivo using diffusion tensor magnetic resonance imaging. J Neurol Neurosurg Psychiatry 2002;72(6):742-746.

37. Naggara O, Oppenheim C, Rieu D, Raoux N, Rodrigo S, Dalla Barba G, Meder JF. Diffusion tensor imaging in early Alzheimer's disease. Psychiatry Res 2006;146(3):243-249.

38. Arnone D, Abou-Saleh MT, Barrick TR. Diffusion tensor imaging of the corpus callosum in addiction. Neuropsychobiology 2006;54(2):107-113.

39. De Bellis MD, Van Voorhees E, Hooper SR, Gibler N, Nelson L, Hege SG, Payne ME, MacFall J. Diffusion tensor measures of the corpus callosum in adolescents with adolescent onset alcohol use disorders. Alcohol Clin Exp Res 2008;32(3):395-404.

40. Sorensen AG, Wu O, Copen WA, Davis TL, Gonzalez RG, Koroshetz WJ, Reese TG, Rosen BR, Wedeen VJ, Weisskoff RM. Human acute cerebral ischemia: detection of changes in water diffusion anisotropy by using MR imaging. Radiology 1999;212(3):785-792.

41. Sotak CH. The role of diffusion tensor imaging in the evaluation of ischemic brain injury - a review. NMR Biomed 2002;15(7-8):561-569.

42. Zelaya F, Flood N, Chalk JB, Wang D, Doddrell DM, Strugnell W, Benson M, Ostergaard L, Semple J, Eagle S. An evaluation of the time dependence of the anisotropy of the water diffusion tensor in acute human ischemia. Magn Reson Imaging 1999;17(3):331-348.

43. Rutgers DR, Fillard P, Paradot G, Tadie M, Lasjaunias P, Ducreux D. Diffusion tensor imaging characteristics of the corpus callosum in mild, moderate, and severe traumatic brain injury. AJNR Am J Neuroradiol 2008;29(9):1730-1735.

44. Wilde EA, McCauley SR, Hunter JV, Bigler ED, Chu Z, Wang ZJ, Hanten GR, Troyanskaya M, Yallampalli R, Li X, Chia J, Levin HS. Diffusion tensor imaging of acute mild traumatic brain injury in adolescents. Neurology 2008;70(12):948-955.

45. Alexander AL, Hasan KM, Lazar M, Tsuruda JS, Parker DL. Analysis of partial volume effects in diffusion-tensor MRI. Magn Reson Med 2001;45(5):770-780.

46. Tuch DS, Reese TG, Wiegell MR, Makris N, Belliveau JW, Wedeen VJ. High angular resolution diffusion imaging reveals intravoxel white matter fiber heterogeneity. Magn Reson Med 2002;48(4):577-582.

47. Behrens TE, Woolrich MW, Jenkinson M, Johansen-Berg H, Nunes RG, Clare S, Matthews PM, Brady JM, Smith SM. Characterization and propagation of uncertainty in diffusion-weighted MR imaging. Magn Reson Med 2003;50(5):1077-1088.

48. Hosey T, Williams G, Ansorge R. Inference of multiple fiber orientations in high angular resolution diffusion imaging. Magn Reson Med 2005;54(6):1480-1489.

49. Tournier JD, Calamante F, Gadian DG, Connelly A. Direct estimation of the fiber orientation density function from diffusion-weighted MRI data using spherical deconvolution. Neuroimage 2004;23:1176-1185.

50. Alexander DC. Maximum entropy spherical deconvolution for diffusion MRI. Inf Process Med Imaging 2005;19:76-87.

51. Dell'Acqua F, Rizzo G, Scifo P, Clarke RA, Scotti G, Fazio F. A model-based deconvolution approach to solve fiber crossing in diffusion-weighted MR imaging. IEEE Trans Biomed Eng 2007;54:462-472.

52. Jian B, Vemuri BC. A unified computational framework for deconvolution to reconstruct multiple fibers from diffusion weighted MRI. IEEE Trans Med Imaging 2007;26(11):1464-1471.

53. Kaden E, Knosche TR, Anwander A. Parametric spherical deconvolution: inferring anatomical connectivity using diffusion MR imaging. Neuroimage 2007;37(2):474-488.

54. Tournier JD, Calamante F, Connelly A. Robust determination of the fibre orientation distribution in diffusion MRI: non-negativity constrained super-resolved spherical deconvolution. Neuroimage 2007;35:1459-1472.

55. Descoteaux M, Deriche R, Knosche TR, Anwander A. Deterministic and probabilistic tractography based on complex fibre orientation distributions. IEEE Trans Med Imaging 2009;28(2):269-286.

56. Barmpoutis A, Jian B, Vemuri BC. Adaptive kernels for multi-fiber reconstruction. Inf Process Med Imaging 2009;21:338-349.

57. Assaf Y, Freidlin RZ, Rohde GK, Basser PJ. New modeling and experimental framework to characterize hindered and restricted water diffusion in brain white matter. Magn Reson Med 2004;52(5):965-978.

58. Neuman CH. Spin echo of spins diffusing in a bounded medium. The Journal of Chemical Physics 1974;60(11):4508-4511.

59. Assaf Y, Blumenfeld-Katzir T, Yovel Y, Basser PJ. AxCaliber: a method for measuring axon diameter distribution from diffusion MRI. Magn Reson Med 2008;59(6):1347-1354.

60. Assaf Y, Basser PJ. Composite hindered and restricted model of diffusion (CHARMED) MR imaging of the human brain. Neuroimage 2005;27(1):48-58.

# Chapter 5

# Histological Validation of Fiber Orientation Distributions

## 5.1 Abstract

Diffusion MRI (dMRI) is widely used to measure microstructural features of brain white matter, but commonly used dMRI measures have limited capacity to resolve the orientation structure of complex fiber architectures. While several promising new approaches have been proposed, direct quantitative validation of these methods against relevant histological architectures remains missing. In this study, we quantitatively compare neuronal fiber orientation distributions (FODs) derived from *ex vivo* dMRI data against histological measurements of rat brain myeloarchitecture using manual recordings of individual myelin stained fiber orientations. We show that accurate FOD estimates can be obtained from dMRI data, even in regions with complex architectures of crossing fibers with an intrinsic orientation error of approximately 5-6 degrees in these regions. The reported findings have implications for both clinical and research studies based on dMRI FOD measures, and provides an important biological benchmark for improved FOD reconstruction and fiber tracking methods.

## 5.2 Introduction

Diffusion magnetic resonance imaging (dMRI) (1,2) is a powerful tool increasingly applied in clinical and research settings for investigating structural properties of biological tissue *in vivo* (3,4). The basic concept of dMRI is to quantify the microscopic self diffusion of water along prescribed directions in three-dimensional (3D) space using a series of diffusion sensitive MR images (5). In biological tissue, the diffusion-driven displacements of water molecules are impeded by intra- and extra-cellular tissue components (6), and therefore their measured displacement distributions provide unique microstructural and architectural information in both normal and pathologic brain tissue (7).

The standard dMRI method is diffusion tensor imaging (DTI) (8), which uses a single 3D Gaussian distribution model for the measured apparent diffusion coefficient (ADC) in each imaging voxel. The shape and orientation of the Gaussian distribution is fully specified by its covariance matrix, or diffusion tensor (DT). In coherent, densely packed, white matter fiber bundles, the direction of fastest diffusion, given by the principal axis (or primary eigenvector) of DT, points along the main axis of the fiber bundle and is commonly used to map the trajectory of white matter fiber tracts in the brain (9-11). However, while the orientation of the DT has been validated in large fiber bundles with coherent fiber orientations in brain (12-15) and myocardial tissues (14,16,17) the tensor model cannot be used to resolve multiple fiber bundles within voxels containing more than one principal direction (18). Such complex fiber architectures frequently occur both in grey and white matter regions containing crossing or branching fiber tracks, and as a consequence of partial volume effects when different neighboring tissue architectures are included in the same voxel. In both cases, the ADC will have multiple diffusion peaks and the DT no longer provides an accurate mathematical description of the apparent diffusion patterns.

This limitation of DTI has prompted numerous efforts to develop dMRI techniques capable of resolving complex fiber architectures within voxels. Diffusion spectrum imaging (DSI) (19) is a popular model-free method that applies the classical formalism of "*q*-space" theory (20,21) to recover the three-dimensional (3D) diffusion propagator, or displacement spectrum in each voxel. The orientation structure of the diffusion propagator can be revealed by summing the propagator in the radial direction, yielding a measure that quantifies the overall likelihood of water diffusion in a given direction in 3D space. This derived function, called the water diffusion orientation distribution function (ODF) can be used as a surrogate measure of complex fiber orientations within voxels (19,22). A related model-free method called *q*-ball imaging (QBI) (23) provides an alternative approach for recovering the diffusion ODF in each voxel using less time intensive and reduced encoding (spherical) diffusion acquisition protocols.

While DSI and QBI are established model-free techniques for recovering important aspects of the water diffusion function in tissue (through measurement of the diffusion propagator or ODF), they do not provide a direct quantitative description of the underlying distribution of fibers or the intrinsic diffusion properties of these fibers (24). This additional level of inference requires a biophysical model for the diffusion properties of the tissue fibers. One popular model-based method is to model the diffusion function of the neuronal fibers with a single diffusion tensor, where the parallel and perpendicular diffusivity of the tensor is fixed for all fibers within the voxel. Under this model, the intrinsic neuronal fiber orientation distribution (FOD) can be estimated via spherical deconvolution of the diffusion signal with a tensor response function (24-29) or using more sophisticated Bayesian methods (30,31). Similar to the water diffusion ODF, the peaks of the FOD can reveal the orientation structure of complex fiber architectures within voxels and is gaining popularity for use in fiber tracking

applications (25,32). Yet another model-based approach is to impart a composite model for the restricted and hindered water inside and outside the myelinated axons to obtain estimates of white matter fiber orientations (33) and diameter distributions (34,35) within voxels.

To date, validation of the orientation structure of both the water diffusion ODF and underlying FOD have primarily involved numerical simulations in conjunction with qualitative comparison with known anatomical features (25-29,36-38), and comparisons with *ex vivo* biological (19,39-41) and non-biological (39,42-44) diffusion phantoms. Thus, there is a lack of direct quantitative validation against realistic biological fiber architectures, and this poses an important limitation to the further development of improved FOD methods and studies which seek to apply these methods for research and clinical purposes.

To amend this, we here quantitatively compare FOD measures derived from *ex vivo* dMRI data against histological measures of rat brain myeloarchitecture. We conclude that FOD measures derived from tomographic dMRI data provide an accurate characterization of underlying myelinated fiber orientation distributions, even in regions with complex fibers architectures where the application of DTI is limited.

## 5.3 Methods

### 5.3.1 Material and data acquisition

Adult male Sprague-Dawley rats were anesthetized (ketamine hydrochloride 50 mg/kg, and sodium pentobarbital 12 mg/kg, i.p.) and euthanized by transcardial perfusion with 4% paraformaldehyde. The isolated brains were immersed for 4 weeks at 4$^{o}$C in a solution of 1mM Gd-DTPA (Magnevist®, Bayer HealthCare Pharmaceuticals, Wayne, NJ, USA) in phosphate buffered saline, and positioned in a sealed plastic tube filled with Fomblin® LC8 liquid (Solvay Solexis, Thorofare, NJ, USA) (45). High b-value QSI data were

acquired using a 2D spin echo echo planar imaging (EPI) sequence on a 4.7T Bruker scanner equipped with a 3 cm solenoid receiver coil. QSI data were collected using a conventional DSI (Cartesian) acquisition scheme. Pulse-sequence parameters for the QSI acquisition were: TR/TE = 650/49 msec, $\Delta/\delta$ = 23/12 msec, 515 q-space directions, $|G|_{max}$ = 380 $mTm^{-1}$, b-max = 30452 $sec/mm^2$, matrix = 64x64x128, voxel size = 265 μm isotropic. Following MR imaging, the brain was coronally sectioned at 50 μm on a freezing microtome, at an angle closely matching the tomographic images. The right side of the brain was marked with a shallow razor-blade cut in the tissue to ensure correct orientation of the sections. One in four sections was stained for myelin using a standard procedure modified from Woelcke (46), yielding an effective through-plane spacing of 200 μm. High-resolution mosaic images were obtained through UPlanApo 20/0.70 and 40/0.85 dry objectives using a motorized Olympus BX52 microscope running the Neurolucida 7.0 software (Virtual Slice module, MBF Bioscience, Inc, Williston, VT, USA).

### 5.3.2 Registration

As any voxel-wise quantitative comparison requires accurate spatial registration of image data, several measures were taken to minimize the potential error of misalignment. First, care was taken during histological processing to ensure that the coronal sectioning angle matched the tomographic slice orientation. Trigonometric measurements of multiple corresponding anatomical landmarks confirmed that the angle of the histological section plane and tomographical slice orientation only differed by about 2 degrees (rotation around the mediolateral axis), thus allowing direct registration without resampling of the QSI slice orientation. Second, the selected ROIs (procedure described below) were confirmed to have 1) minimal nonlinear distortion in both the histological data (due to histological processing) and

QSI data, and 2) consistent myeloarchitecture across multiple coronal (through-plane) sections. Third, a careful and detailed manual registration protocol was performed for both ROIs. Corresponding anatomical landmarks (brain surface, genu and splenium of the corpus callosum, anterior commisure, the ventricular system, the oculomotor nerve, and several mesencephalic and brain stem nuclei) were identified on basis of general gray and white contrast and used to assign relative anterioposterior position coordinates across the whole brain for both image modalities. Then, for each ROI (one in the forebrain at the level of the genu of the corpus callosum, and the other in the brain stem at level of the superior colliculus, see Fig. 5.1), histological images were manually registered to corresponding QSI images. Groups of corresponding tomographical and histological images from a volume approximating a ~1 mm thick coronal brain section (corresponding to 4 QSI and 20 histological slices) through both ROIs were assembled as separate layers using the program Adobe Illustrator CS3 (Adobe Systems Inc. San Jose, CA, USA). Each layer was scaled appropriately depending upon the native voxel size. Finally, using the QSI images as a reference, the histological images were individually adjusted using affine transformations to match multiple local gray and white matter landmarks. This final alignment procedure was iterated until optimal spatial matching was achieved.

### 5.3.3 ROI selection

ROIs were selected on the basis of 1) color-coded DT maps, 2) 3D DT and FOD reconstructions, and 3) visual inspection of myeloarchitecture. The first ROI (ROI-1) was selected to contain relatively uniform white matter fiber orientations (Figs. 5.1A,B; 5.2A). To help find this location, a red-green-blue (RGB) map was created using the primary eigenvector $\mathbf{e}_1$ of the DT (”preferred” direction), where each vector element defined the red, green, and

blue components of each voxel, respectively. The brightness of this preferred RGB map was determined using a measure of the degree of linear anisotropy, defined as $C_l = (\lambda_1 - \lambda_2)/ \lambda_1$ (47), where $\lambda_1$, $\lambda_2$, and $\lambda_3$ are the first, second, and third eigenvalues of DT, respectively. Thus, a bright red color in the preferred RGB map indicates a high degree of linear anisotropy with left-right orientation (Fig. 5.1A,A'). The second ROI (ROI-2) was selected to contain complex crossing fiber orientations (Figs. 5.1C,D; 2B). To help find this location an RGB map of the third eigenvector $\mathbf{e}_3$ ("non-preferred" direction) was created and the brightness of this non-preferred RGB map was defined using a measure of the degree of planar anisotropy, defined as $C_p = (\lambda_2 - \lambda_3)/ \lambda_1$ (47). Voxels with a bright blue color would thus indicate a "disk-like" DT (indicative of crossing fibers) within the image plane ($\mathbf{e}_3$ points through-plane, Fig. 5.1D,D'). 3D DT and FOD reconstructions provided additional confirmation of apparent crossing fiber architectures that were highly consistent across animals. Finally, the myeloarchitecture in ROI-1 and ROI-2 were microscopically inspected in the original histological sections to confirm the neuroarchitectural patterns suggested by the tomographic data.

### 5.3.4 Computation of HIST-FODs

The HIST-FODs in ROI-1 and 2 were derived using a systematic random stereological approach adapted from (12). High-resolution histological images from two consecutive myelin stained sections (spaced at 200 μm) were assembled in separate layers in the Adobe Illustrator file used for image registration (see registration section above). A grid derived from the voxel matrix of the spatially corresponding QSI slice was superimposed onto the histological images. Each voxel domain was further subdivided using a 5x5 rectangular sampling grid. In four systematically positioned sample grids (Fig. 5.2A,B), individual myelin

fiber trajectories were traced as vector lines using Adobe Illustrator. The vector coordinates were exported to Matlab (The Mathworks, Inc. Natick, MA) and HIST-FODs were computed for each QSI voxel by calculating the angular histogram of the line plots (fiber vectors) with a bin size of 1° (360 points) from the four sub regions. To further increase the robustness of the HIST-FODs, corresponding angular histograms from two neighboring myelin sections spaced 200 μm apart were averaged together and the averaged histogram was smoothed with a Gaussian kernel with a FWHM of 8°. In this way, our histological sampling included a through-plane distance approximately corresponding to the depth of a single 265 □m QSI voxel. To quantify the intrinsic degree of fiber spreading within ROI-1 of the corpus callosum, Gaussian distributions were fit to the final angular histograms of each voxel, yielding an average FWHM of approximately 34º.

### 5.3.5 Computation of DT-FODs

Since the diffusion tensor (DT) is a model for the apparent diffusion coefficient (ADC), a direct comparison with the HIST-FODs would be misleading. Under the DT model, the fiber orientation is given by a single delta function pointed in the direction of the primary eigenvector. To generate DT equivalent FODs (DT-FODs), the resultant delta functions were convolved with a Gaussian smoothing kernel with a FWHM of 34°. This level of smoothing was chosen to match the intrinsic angular dispersion of fibers within the ROI-1 of the corpus callosum.

### 5.3.6 Computation of QSI-FODs

To estimate the QSI-FODs, we extend the traditional spherical deconvolution method in Reference (29) to arbitrary (multi-b-value) *q*-space acquisitions. A axially symmetric tensor model (48) was chosen for the single fiber response function with perpendicular ($\lambda_\perp = \lambda_2 = \lambda_3 = 4.0 \times 10^{-5}$ mm$^2$s$^{-1}$) and parallel diffusivities ($\lambda_\parallel = \lambda_1 = 3.5 \times 10^{-4}$ mm$^2$s$^{-1}$) estimated directly from the QSI data in ROI-1, similar to the approach used in (29). Tikhonov regularization was used to improve the conditioning of the inversion. The FOD solution was parameterized using radial-basis functions, as in Ref (26). The radial-basis functions themselves are parameterized by the desired FOD reconstruction points and the radial-basis function width parameter σ. For the 3D QSI-FOD reconstructions in Fig. 5.2, a 3$^{rd}$ order icosahedral tessellation of the sphere was chosen for the FOD reconstruction points (642 vertices) and σ was set to 20. For the 2D QSI-FOD reconstructions in Figs. 5.4 and 5.5, 360 equally spaced points on the unit circle was chosen for the FOD reconstruction points, and σ was set to 10. This value of σ was chosen because it optimized the correlations with the HIST-FODs in ROI-2. However, we tested a range of different values for σ (from 1 to 20) and found that the average correlations and angular error for the FOD peaks were largely robust to variations in this parameter.

## 5.4 Results

High b-value *q*-space imaging (QSI) data were acquired from fixed adult rat brains that had been immersed in a contrast enhancing gadolinium solution (Magnevist® (45)). Following tomographic imaging, coronal histological sections of the tissue were obtained and stained for myelin and high resolution digital images acquired. Tomographic and histological

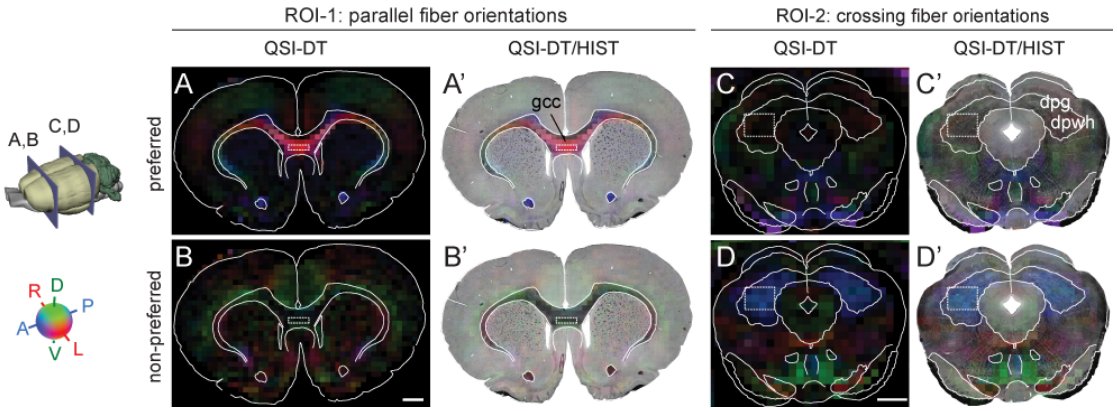


**Figure 5.1**. Anatomical ROIs containing coherent or crossing fiber orientations without anterior-to-posteriorly orientated fibers were identified using red-green-blue (RGB) maps of the preferred (**A,A**',**C**,**C**') and non-preferred (**B,B**',**D,D**') diffusion direction, indicated by the first and third eigenvector of the DT, respectively. Voxel colors indicate the direction of the respective eigenvectors (cf. color code insert, bottom left), while the voxel brightness is given by the degree of linear and planar diffusion anisotropy for the preferred and non-preferred maps, respectively. (**A**,**B**) Coronal RGB maps through the genu of the corpus callosum, and (**C**,**D**) coronal RGB maps through the brain stem at level of the superior colliculus (position indicated on the 3D rat brain insert). (**A**'-**D**') Overlay of RGB maps and corresponding myelin stained section images. The bright red color in (**A**,**A**') indicates a high degree of linear anisotropy with left-right orientation, consistent with coherent mediolaterally oriented commissural fibers in this region (see, also Fig. 5.2C). In the corresponding non-preferred map (**B**,**B**'), the same voxels are dark, indicating a lack of planar diffusion anisotropy. The bright blue color of the non-preferred map in (**D**,**D**') indicates a high degree of planar anisotropy (typical of crossing fibers, see, also Fig. 5.2D) within the coronal plane. In the corresponding preferred map (**C**,**C**') these voxels are dark, consistent with a lack of uniformly oriented fibers. For our quantitative analysis, we selected four voxels in a 1x4 grid in the bright red region in the corpus callosum (ROI-1; dotted white frame in **A**,**A**',**B**,**B**') and twelve voxels in a 3x4 grid in the bright blue region in the tectum (ROI-2; dotted white frame in **C**,**C**', **D**,**D**'). dpg, deep gray layer of the superior colliculus; dpwh, deep white layer of the superior colliculus; gcc, genu of the corpus callosum. Scale bars, 1 mm.

images from corresponding regions-of-interest (ROIs) were co-registered using affine transformations and quantitatively compared.

### 5.4.1 ROI specification

Our first objective was to identify suitable ROIs in which 3D FODs can be compared to inherently 2D, coronally sectioned histological data. We focused our analysis on two ROIs with little or no through-plane (anterioposteriorly oriented) fiber orientations containing 1)

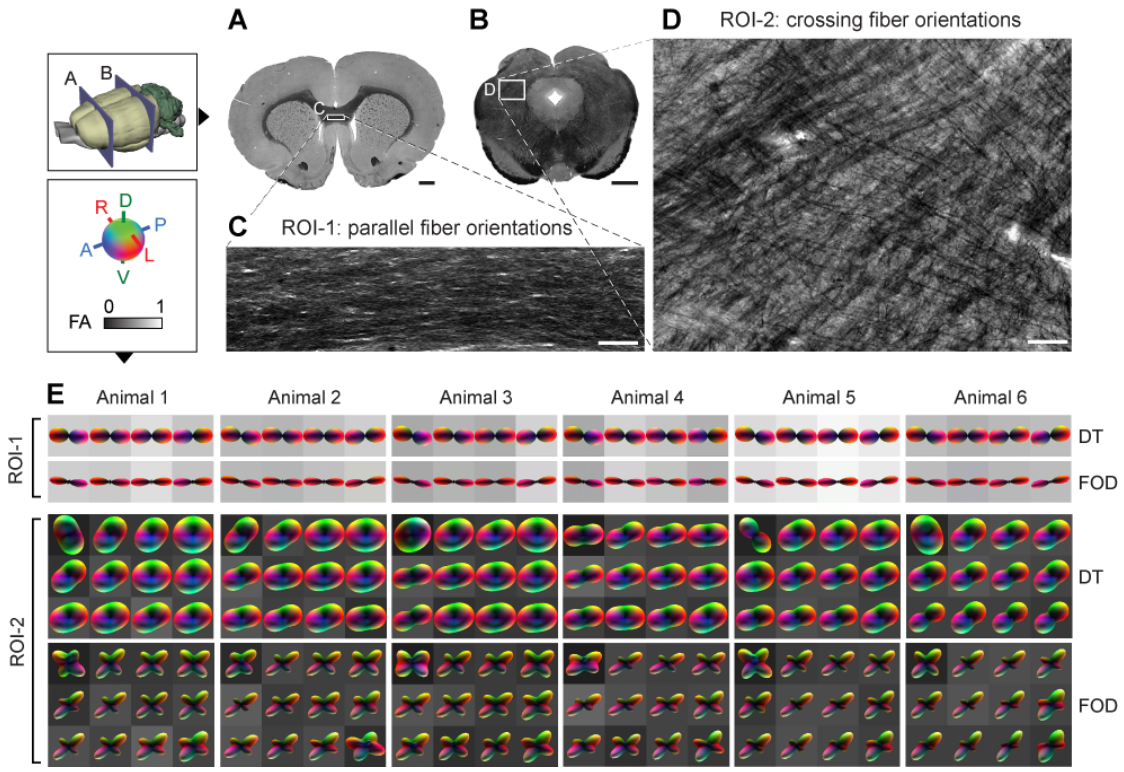


**Figure 5.2**. Three-dimensional DT and FOD reconstructions in brain regions with parallel and crossing fiber orientations. (**A-D**) Detailed visualization of the parallel (**A**,**C**) and crossing (**B**,**D**) myeloarchitecture in ROI-1 and -2. (**E**) Comparison of 3D DT and FOD reconstructions from ROI-1 and -2 across all six animal specimens. Reconstructions are overlaid on a gray scale map of the fractional anisotropy (FA) index (49) derived from the DT eigenvalues and quantifying the overall degree of diffusion anisotropy on a 0-1 scale (1 being highly anisotropic and 0 being isotropic). The high FA values and elongated DT and FOD profiles in ROI-1 are characteristic of coherent (parallel) fiber orientations, while the low FA values and disk-like DT profiles in ROI-2 are characteristic of crossing fibers, which is further evidenced by the FOD reconstructions and myeloarchitecture. All DT and FOD reconstructions are shown min-max normalized for reasons discussed in the main text. Scale bars, 1 mm (**A,C**) and 100 μm (**C,D**).

coherently oriented fibers, or 2) more complex crossing fiber architectures where the DT model is known to be insufficient. The ROIs were selected on the basis of color-coded DT maps, 3D reconstructions of the DT and FOD, and visual inspection of myelin stained histological sections (Figs. 5.1, 5.2). The first region selected (ROI-1) was a 1x4 voxel grid within an area of the anterior part (genu) of the corpus callosum containing high densities of within-plane mediolaterally oriented commissural fibers (50-52), apparent from red colored

voxels in the color-coded DT maps (Figs. 5.1A,B). Because the DT model has previously been validated in regions with uniform fiber orientations (12-15), this region was used primarily as a benchmark to confirm that both the DT and FOD provided accurate assays of myeloarchitecture in this region. The second region selected (ROI-2) was a 3x4 voxel grid within an area of the deep gray and white layers of the superior colliculus containing transversely oriented bundles of intratectal and tectal afferent and efferent projection fibers (53,54) (Figs. 5.1C,D; 5.2D). Here the color-coded DT maps showed planar "disk-like" diffusion profiles indicative of crossing fibers (Fig. 5.1D. blue color). In both ROIs, histological assessment confirmed predominantly contained structures with in-plane orientations (Fig. 5.2C,D), suitable for two-dimensional histological validation.

### 5.4.2 Qualitative comparison of DT, FOD and myeloarchitecture

Our second objective was to assess the resemblance of DT and FOD measurements with histological visualizations of myeloarchitecture in the selected ROIs. In ROI-1, 3D DT and FOD reconstructions across all six animals showed the expected "cigar-like" profiles with left-right orientation (Fig. 5.2E). In ROI-2, 3D DT reconstructions in all six animals confirmed the "disk-like" shape of the DT, and 3D FOD reconstructions indicated the expected crossing fiber patterns (Fig. 5.2E). The orientation of the FOD reconstructions were highly consistent across animals in both ROIs and with the morphology evidenced in the myelin stained sections (Fig. 5.2C,D). Taken together, these results demonstrate a high qualitative resemblance between 3D FOD measures and histological observations of crossing fibers which is highly consistent across several animals. To provide a more rigorous quantitative histological validation of this relationship, we continued to perform a detailed voxel-wise quantitative

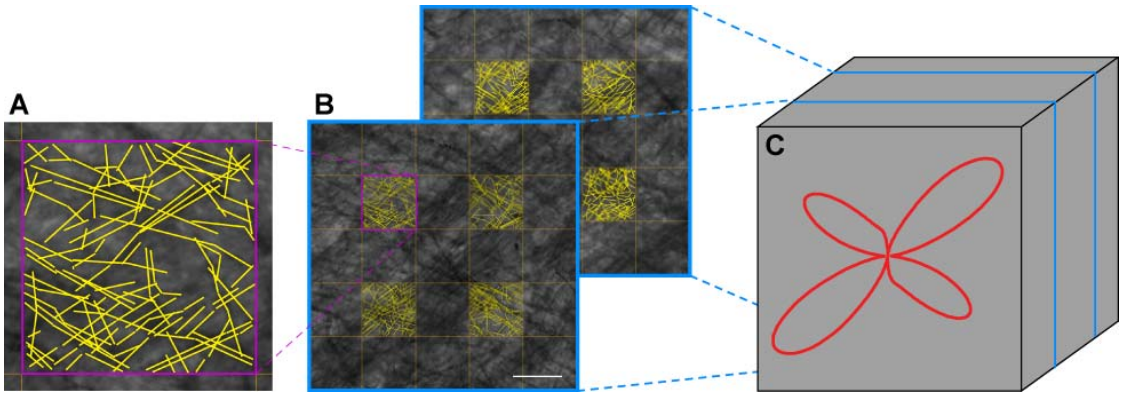


**Figure 5.3**. Computation of a single HIST-FOD from multiple myelin stained section images. (A) Myelin fiber orientations were manually traced as vector lines within 53x53 μm sample grids positioned above high-resolution images of myelin stained sections. (B) For each histological section, 4 sample grids were systematically positioned within a voxel domain. (C) For each QSI voxel, myelin fiber orientations were estimated from vector data collected from 8 sample grids across two histological sections spaced at 100 μm. This procedure was repeated for all voxels in both ROI-1 and 2. Scale bar, 50 μm.

comparison between these measures in ROI-1 and -2 in one of the animal specimens (animal 1).

### 5.4.3 Quantitative histological validation of FOD estimates

Our third objective was to quantitatively evaluate the correspondence between high b-value QSI-derived FOD measures (QSI-FODs) and myeloarchitecture in both ROI-1 and 2. As a benchmark for the comparisons we also included DT fiber orientation estimates (DT-FOD) in both regions (see also "Computation of DT-FODs" in the "Materials and Methods" section).

To validate the QSI-FODs, we used a voxel-wise stereological sampling approach to manually record several hundred myelin stained fiber orientations from multiple registered myelin stained histological images (Fig. 5.3A,B). The angular histogram of all fiber samples (or fiber counts in a given angular bin) within each voxel constitutes the empirical histology-derived FOD (HIST-FOD; Fig. 5.3C) used as the validation standard to compare against the

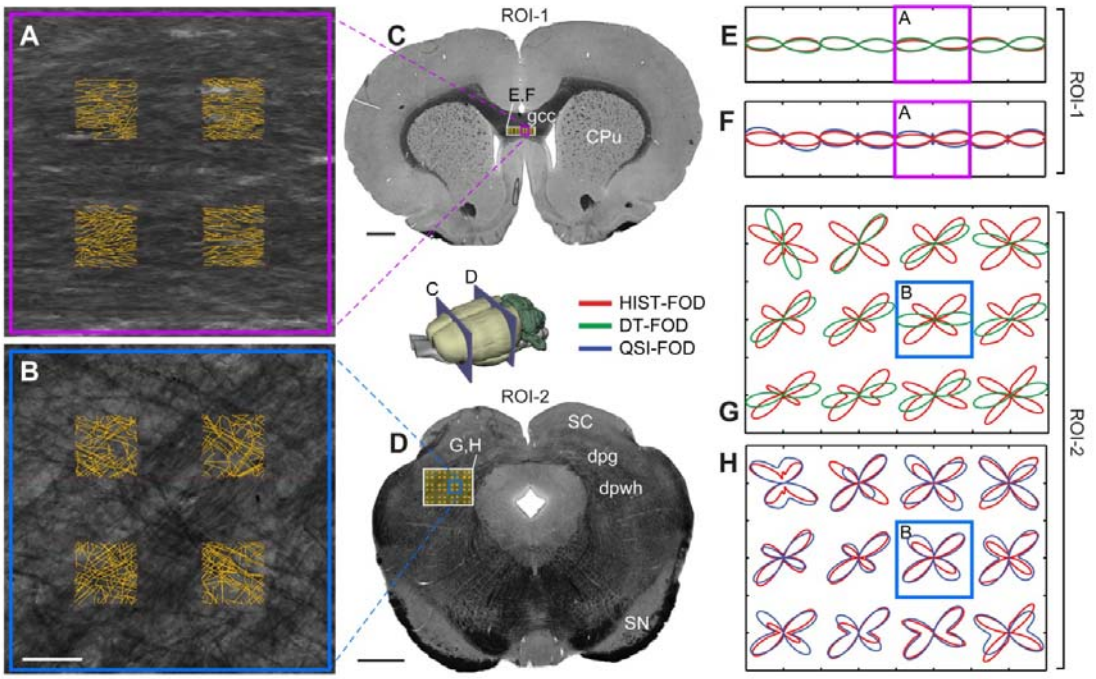


**Figure 5.4.** Comparison of FOD estimates against myeloarchitecture. (**A**,**B**) High resolution images of myeloarchitecture corresponding to one QSI voxel with overlay of 4 sample grids of manually-recorded fiber directions (yellow lines) used in part to compute HIST-FODs (8 total sample grids were used, cf. Fig. 5.2). Purple and blue frames indicate corresponding voxel locations across panels. (**C**,**D**) Coronal myelin sections through the genu of the corpus callosum (**C**) and superior colliculus (**D**) (levels indicated on 3D rat brain insert) showing the position of the 1x4 voxel ROI-1 and 3x4 voxel ROI-2 (white frames, cf. Fig 5.1). (**E**,**F** and **G**,**H**) Comparison of QSI-FODs and DT-FODs against corresponding HIST-FODs (**E**,**F**: ROI-1and **G**,**H**: ROI-2). gcc, genu of the corpus callosum; dpg, deep gray layer of the superior colliculus; dpwh, deep white layer of the superior colliculus. Scale bar, 50 μm **(B)** and 1mm (**C**,**D**).

DT- and QSI-FOD estimates. Prior to comparison, all fiber models were min-max normalized to remove the isotropic component and normalize the maximum amplitude of the respective distributions. The isotropic component was removed because in conventional QSI-FOD measures there is no way to separate the isotropic fiber orientation from the isotropic ADC, and thus if not removed, the QSI-FODs would have a (biased) larger isotropic component compared with the HIST-FODs.

We found that in ROI-1, which contained fibers with relatively homogeneous fiber orientations, both the QSI-FOD and DT-FODs correlated well with the HIST-FODs (average Pearson correlation coefficients r = 0.98; SD = 0.02 for QSI-FODs, and 0.99; SD = 0.01 for DT-FODs, $n$ = 4 voxels; Fig. 5.4E,F). By contrast, in ROI-2, which contained crossing fibers, the DT-FODs correlated poorly with HIST-FODs (average Pearson correlation coefficients r = 0.16; SD = 0.38; $n$ = 12 voxels), while QSI-FODs correlated substantially better (average Pearson correlation coefficients r = 0.86; SD = 0.07; Fig. 5.4GH). A non-parametric permutation-based 2-sample t-test revealed that the difference in correlation between the DT-FODs and QSI-FODs were not significant in ROI-1 ($p>>0.05$), but highly significant in ROI-2 ($p<0.0001$). These results quantitatively confirm that QSI-FODs provide accurate assays of the underlying myeloarchitecture in regions of both uniform and complex crossing fiber orientations.

We also quantitatively evaluated the orientation error of the QSI-FOD peaks in ROI-2 (Fig. 5.5). We found that the peak orientations of the QSI-FODs closely matched the peaks of the HIST-FODs, with an average angular error (across all 12 voxels) of 5.7°; SD 3.8° (Fig. 5.5). The average (acute) intersection angle of the HIST-FOD peaks was $\theta$ = 73°; SD = 8° (Fig. 5.5, Table 1). It should be noted that these results were obtained using a radial-basis function parameterization of the QSI-FODs with a width of $\sigma$ = 10 (see "Materials and Methods"), which maximized the correlation with the HIST-FODs in ROI-2. However, further testing revealed that the angular error and correlation were relatively robust to variations in $\sigma$. When testing a range of $\sigma$ between 1 and 20, the average angular error and correlation coefficient only varied between 5.4°-6.2° and 0.83 and 0.86, respectively (data not shown).

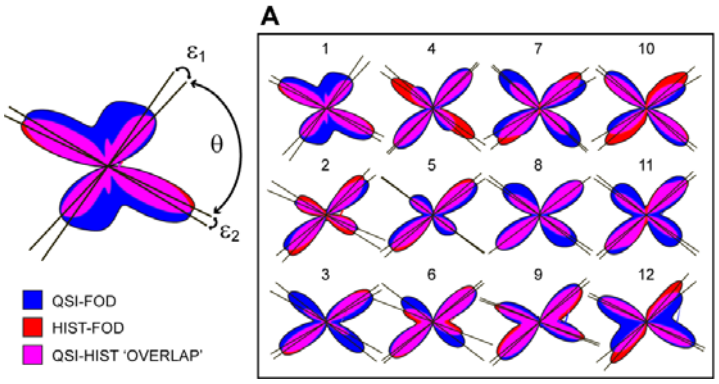


| Voxel # | Corr (r) | θ | $\varepsilon_1$ | $\varepsilon_2$ |
|---|---|---|---|---|
| 1 | 0.85 | 73° | 8° | 5° |
| 2 | 0.92 | 79° | 8° | 9° |
| 3 | 0.82 | 64° | 5° | 9° |
| 4 | 0.86 | 79° | 2° | 7° |
| 5 | 0.93 | 77° | 6° | 1° |
| 6 | 0.87 | 61° | 3° | 16° |
| 7 | 0.88 | 81° | 11° | 2° |
| 8 | 0.93 | 71° | 0° | 4° |
| 9 | 0.94 | 59° | 4° | 2° |
| 10 | 0.79 | 79° | 10° | 4° |
| 11 | 0.83 | 74° | 4° | 4° |
| 12 | 0.68 | 76° | 10° | 3° |

**Figure 5.5**. Quantitative comparison of fiber orientation distributions in ROI-2. (**A**) Superimposed HIST-FODs (red) and QSI-FODs (blue) are shown for each of the 12 voxels in ROI-2, together with peak orientations (black lines) for the respective fiber orientation distributions. Purple color indicates FOD overlap. (**B**) For quantitative analysis, the acute intersection angle of the HIST-FODs (θ), and the angular error of both FOD peaks ($\varepsilon_1$ and $\varepsilon_2$) are given for each of the 12 voxels together with the Pearson correlation coefficients (r) between the HIST- and QSI-FODs. The average Pearson correlation was r = 0.86; SD = 0.07, average intersection angle was θ = 73°; SD = 8°, average angular error ($\varepsilon_1$ and $\varepsilon_2$ combined) was 5.7°; SD = 3.8°.

## 5.5 Discussion

While methods for estimating neuronal fiber orientation distributions (FODs) in dMRI are becoming increasingly popular, the correspondence between FOD measures and realistic biological fiber architectures has been unclear. Using detailed manual recordings of individual myelin stained fiber orientations in *ex vivo* rat brain tissue we have shown that tomographic dMRI FOD estimates provide accurate assays of the underlying myeloarchitecture, even in regions with complex multi-directional crossing fiber architectures.

In this study, FODs were quantitatively validated using a voxel-wise approach against empirical FOD estimates derived from registered myelin stained images. As evident in Fig. 5.4F,E, QSI-FODs provided an accurate characterization of the underlying myelinated fiber orientation distribution in regions of both uniform ($r > 0.9$) and crossing fiber ($r > 0.8$)

architectures. A subsequent evaluation of the angular error of the QSI-FOD peaks in ROI-2 demonstrated an average angular error of approximately 5-6º, with an average (acute) fiber crossing angle of approximately 73° (Fig. 5.5). Because it seems reasonable to assume that some of this error is likely due to image registration and stereological errors (e.g., through-plane fiber contributions and sampling limitations), the actual intrinsic angular error of the QSI-FOD peaks is probably even less than 5-6º.

It should be noted that the FODs in this paper were computed from QSI data with high b-values and a large number of diffusion measurements (b-max = 30452 sec/mm$^2$, 515 diffusion measurements, see "Materials and Methods"). Thus, it remains to be determined to what extent similarly accurate assays of myeloarchitecture can be derived using more conservative spherical acquisition protocols as often employed on clinical 1.5T and 3.0T scanners for *in vivo* applications. However, numerous simulation studies (44,55) have demonstrated that FODs (with the ability to resolve crossing fibers down to about 45°) can be derived from spherical acquisition protocols using moderate b-values (b ~ 2000-4000 s/mm$^2$) and reasonable scan times (SNR ~30, scan time < 10 min). These simulation studies suggest that accurate FODs can be achieved in regions with complex architectures with use of reduced encoding spherical acquisition protocols. Hence, the validation benchmarks established in this paper will likely also have a high degree of translational value for the clinical situation.

The histological FODs were based on manually traced myelin fibers sampled from high-resolution digital images of 50 μm thick sections using a systematic random approach. Sampling occurred both within (using sampling bins) and across planes (one focal plane in two sections spaced at 200 μm) to ensure that a representative fraction of the myeloarchitecture was recorded per voxel volume. It should also be noted that water diffusion is influenced by the complete tissue microarchitecture and not only mylinated fibers (for

review, see Ref (6)), which will bias the dMRI measurements relative to the histological measurements. However, the high correlations measured suggest that the contribution of other tissue elements is relatively small in the regions investigated.

The QSI-FODs showed a remarkable consistency across animal specimens (Fig. 5.2E). We thus chose to restrict the quantitative validation to extensive, in depth anatomical analyses of fiber architectures in one specimen. In these analyses, FOD estimates within each voxel were derived from several hundred manually traced histological measurements across multiple coronal sections and several hundred QSI diffusion measurements. Thus, although the total number of voxels compared was relatively small (4 for ROI-1 and 12 for ROI-2), the statistical correlations were based on measurements derived from extremely high dimensional datasets. It should further be noted that the statistical correlations were only used to provide a quantitative metric of similarity at each voxel, and not as a statistical test of consistency or generalizability across animal specimens.

The voxel-wise histological validations were conducted in paraformaldehyde fixed tissue that had been immersed in contrast enhancing Magnevist® liquid (see "Materials and Methods"). Because this treatment is known to reduce the ADC (45), some care should be exercised when extrapolating these results to the *in vivo* case. However, it has been shown that fixation has relatively small effects on the overall amount of diffusion anisotropy, as the ADC is reduced equally in all directions (45). Therefore, the fixation process itself is not likely to have influenced the general orientation structure of the QSI-FOD measurements in this study.

We conclude that fiber orientation distributions derived from high dimensional diffusion MRI data provide accurate assays of the underlying myeloarchitecture, even in regions with complex crossing fiber architectures. These results have important implications for both clinical and research studies investigating structural aspects of biological tissues using

estimates of the fiber orientation distribution. Furthermore, this study provides an important biological benchmark for further improvement of fiber orientation reconstruction and tracking methods.

## 5.6 Acknowledgements

Funding for this work was provided by the following NIH grants: 1R01AG031224, 1U01AG024904-02, 5 U24 RR021382-04, U54 NS056883-01. Chapter 5, in full, has recently been accepted to the journal PLoS One: *Quantitative Histological Validation of Diffusion MRI Fiber Orientation Distributions in the Rat Brain,* Trygve B. Leergaard, Nathan S. White, Alex de Crespigny, Ingeborg Bolstad, Helen D'Arceuil, Jan G. Bjaalie, and Anders M. Dale, 2009. The dissertation author was a shared primary investigator and first author of this paper (along with Trygve B. Leergaard).

## 5.7 References

1. Merboldt K-D, Hanicke W, Frahm J. Self-diffusion NMR imaging using stimulated echoes. Journal of Magnetic Resonance (1969) 1985;64(3):479-486.

2. Taylor DG, Bushell MC. The spatial mapping of translational diffusion coefficients by the NMR imaging technique. Phys Med Biol 1985;30(4):345-349.

3. Le Bihan D. Molecular diffusion, tissue microdynamics and microstructure. NMR Biomed 1995;8(7-8):375-386.

4. Le Bihan D, Breton E, Lallemand D, Grenier P, Cabanis E, Laval-Jeantet M. MR imaging of intravoxel incoherent motions: application to diffusion and perfusion in neurologic disorders. Radiology 1986;161(2):401-407.

5. Stejskal EO, Tanner JE. Spin diffusion measurements: Spin echoes in the presence of a time-dependent field gradient. JChemPhys 1965;42:288.

6. Beaulieu C. The basis of anisotropic water diffusion in the nervous system - a technical review. NMR Biomed 2002;15(7-8):435-455.

7. Moseley ME, Kucharczyk J, Mintorovitch J, Cohen Y, Kurhanewicz J, Derugin N, Asgari H, Norman D. Diffusion-weighted MR imaging of acute stroke: correlation with T2-weighted and magnetic susceptibility-enhanced MR imaging in cats. AJNR Am J Neuroradiol 1990;11(3):423-429.

8. Basser PJ, Mattiello J, LeBihan D. MR diffusion tensor spectroscopy and imaging. BiophysJ 1994;66(1):259-267.

9. Assaf Y, Pasternak O. Diffusion tensor imaging (DTI)-based white matter mapping in brain research: a review. JMolNeurosci 2008;34(1):51-61.

10. Mori S, van Zijl PC. Fiber tracking: principles and strategies - a technical review. NMR Biomed 2002;15(7-8):468-480.

11. Johansen-Berg H, Behrens TE. Just pretty pictures? What diffusion tractography can add in clinical neuroscience. CurrOpinNeurol 2006;19(4):379-385.

12. Kaufman JA, Ahrens ET, Laidlaw DH, Zhang S, Allman JM. Anatomical analysis of an aye-aye brain (Daubentonia madagascariensis, primates: Prosimii) combining histology, structural magnetic resonance imaging, and diffusion-tensor imaging. AnatRecA DiscovMolCell EvolBiol 2005;287(1):1026-1037.

13. Dauguet J, Peled S, Berezovskii V, Delzescaux T, Warfield SK, Born R, Westin CF. Comparison of fiber tracts derived from in-vivo DTI tractography with 3D histological neural tract tracer reconstruction on a macaque brain. Neuroimage 2007;37(2):530-538.

14. Hsu EW, Muzikant AL, Matulevicius SA, Penland RC, Henriquez CS. Magnetic resonance myocardial fiber-orientation mapping with direct histological correlation. AmJPhysiol 1998;274(5 Pt 2):H1627-H1634.

15. Lin CP, Tseng WY, Cheng HC, Chen JH. Validation of diffusion tensor magnetic resonance axonal fiber imaging with registered manganese-enhanced optic tracts. Neuroimage 2001;14(5):1035-1047.

16. Holmes AA, Scollan DF, Winslow RL. Direct histological validation of diffusion tensor MRI in formaldehyde-fixed myocardium. Magn ResonMed 2000;44(1):157-161.

17. Scollan DF, Holmes A, Winslow R, Forder J. Histological validation of myocardial microstructure obtained from diffusion tensor magnetic resonance imaging. Am J Physiol 1998;275(6 Pt 2):H2308-2318.

18. Le Bihan D, Poupon C, Amadon A, Lethimonnier F. Artifacts and pitfalls in diffusion MRI. JMagn ResonImaging 2006;24(3):478-488.

19. Wedeen VJ, Hagmann P, Tseng WY, Reese TG, Weisskoff RM. Mapping complex tissue architecture with diffusion spectrum magnetic resonance imaging. Magn ResonMed 2005;54(6):1377-1386.

20. Cory DG, Garroway AN. Measurement of translational displacement probabilities by NMR: an indicator of compartmentation. Magn Reson Med 1990;14(3):435-444.

21. Callaghan PT, Coy A, MacGowan D, Packer KJ, Zelaya FO. Diffraction-like effects in NMR diffusion studies of fluids in porous solids. Nature 1991;351(6326):467-469.

22. Tuch DS. Diffusion MRI of Complex Tissue Structure. Cambridge, MA: Ph.D. Thesis, Massachusetts Institute of Technology; 2002. 218p p.

23. Tuch DS. Q-ball imaging. Magn ResonMed 2004;52(6):1358-1372.

24. Anderson AW. Measurement of fiber orientation distributions using high angular resolution diffusion imaging. Magn ResonMed 2005;54(5):1194-1206.

25. Kaden E, Knosche TR, Anwander A. Parametric spherical deconvolution: inferring anatomical connectivity using diffusion MR imaging. Neuroimage 2007;37(2):474-488.

26. Alexander DC. Maximum entropy spherical deconvolution for diffusion MRI. InfProcess MedImaging 2005;19:76-87.

27. Jian B, Vemuri BC. A unified computational framework for deconvolution to reconstruct multiple fibers from diffusion weighted MRI. IEEE Trans Med Imaging 2007;26(11):1464-1471.

28. Dell'Acqua F, Rizzo G, Scifo P, Clarke RA, Scotti G, Fazio F. A model-based deconvolution approach to solve fiber crossing in diffusion-weighted MR imaging. IEEE TransBiomedEng 2007;54(3):462-472.

29. Tournier JD, Calamante F, Gadian DG, Connelly A. Direct estimation of the fiber orientation density function from diffusion-weighted MRI data using spherical deconvolution. Neuroimage 2004;23(3):1176-1185.

30. Canales-Rodriguez EJ, Melie-Garcia L, Iturria-Medina Y, Martinez-Montes E, Aleman-Gomez Y, Lin CP. Inferring multiple maxima in intravoxel white matter fiber distribution. Magn Reson Med 2008;60(3):616-630.

31. Melie-Garcia L, Canales-Rodriguez EJ, Aleman-Gomez Y, Lin CP, Iturria-Medina Y, Valdes-Hernandez PA. A Bayesian framework to identify principal intravoxel diffusion profiles based on diffusion-weighted MR imaging. Neuroimage 2008;42(2):750-770.

32. Descoteaux M, Deriche R, Knosche TR, Anwander A. Deterministic and probabilistic tractography based on complex fibre orientation distributions. IEEE Trans Med Imaging 2009;28(2):269-286.

33. Assaf Y, Basser PJ. Composite hindered and restricted model of diffusion (CHARMED) MR imaging of the human brain. Neuroimage 2005;27(1):48-58.

34. Assaf Y, Blumenfeld-Katzir T, Yovel Y, Basser PJ. AxCaliber: a method for measuring axon diameter distribution from diffusion MRI. Magn Reson Med 2008;59(6):1347-1354.

35. Barazany D, Basser PJ, Assaf Y. In vivo measurement of axon diameter distribution in the corpus callosum of rat brain. Brain 2009;132(Pt 5):1210-1220.

36. Alexander DC. Maximum entropy spherical deconvolution for diffusion MRI. Inf Process Med Imaging 2005;19:76-87.

37. Zhan W, Yang Y. How accurately can the diffusion profiles indicate multiple fiber orientations? A study on general fiber crossings in diffusion MRI. J Magn Reson 2006;183(2):193-202.

38. Hess CP, Mukherjee P, Han ET, Xu D, Vigneron DB. Q-ball reconstruction of multimodal fiber orientations using the spherical harmonic basis. Magn Reson Med 2006;56(1):104-117.

39. Lin CP, Wedeen VJ, Chen JH, Yao C, Tseng WY. Validation of diffusion spectrum magnetic resonance imaging with manganese-enhanced rat optic tracts and ex vivo phantoms. Neuroimage 2003;19(3):482-495.

40. Descoteaux M, Angelino E, Fitzgibbons S, Deriche R. Regularized, fast, and robust analytical Q-ball imaging. Magn Reson Med 2007;58(3):497-510.

41. Campbell JS, Siddiqi K, Rymar VV, Sadikot AF, Pike GB. Flow-based fiber tracking with diffusion tensor and q-ball data: validation and comparison to principal diffusion direction techniques. Neuroimage 2005;27(4):725-736.

42. Perrin M, Poupon C, Rieul B, Leroux P, Constantinesco A, Mangin JF, Lebihan D. Validation of q-ball imaging with a diffusion fibre-crossing phantom on a clinical scanner. Philos Trans R Soc Lond B Biol Sci 2005;360(1457):881-891.

43. Cho KH, Yeh CH, Tournier JD, Chao YP, Chen JH, Lin CP. Evaluation of the accuracy and angular resolution of q-ball imaging. Neuroimage 2008;42(1):262-271.

44. Tournier JD, Yeh CH, Calamante F, Cho KH, Connelly A, Lin CP. Resolving crossing fibres using constrained spherical deconvolution: validation using diffusion-weighted imaging phantom data. Neuroimage 2008;42(2):617-625.

45. D'Arceuil H, de CA. The effects of brain tissue decomposition on diffusion tensor imaging and tractography. Neuroimage 2007;36(1):64-68.

46. Woelcke M. Eine neue Methode der Markscheidenfarbung. JPsycholNeurol 1942;51:199-202.

47. Westin CF, Maier SE, Mamata H, Nabavi A, Jolesz FA, Kikinis R. Processing and visualization for diffusion tensor MRI. Med Image Anal 2002;6(2):93-108.

48. Hsu EW, Mori S. Analytical expressions for the NMR apparent diffusion coefficients in an anisotropic system and a simplified method for determining fiber orientation. Magn ResonMed 1995;34(2):194-200.

49. Basser PJ, Pierpaoli C. Microstructural and physiological features of tissues elucidated by quantitative-diffusion-tensor MRI. JMagn ResonB 1996;111(3):209-219.

50. Heimer L, Ebner FF, Nauta WJ. A note on the termination of commissural fibers in the neocortex. Brain Res 1967;5(2):171-177.

51. Sargon MF, Mas N, Senan S, Ozdemir B, Celik HH, Cumhur M. Quantitative analysis of myelinated axons of commissural fibers in the rat brain. AnatHistolEmbryol 2003;32(3):141-144.

52. Wise SP, Jones EG. The organization and postnatal development of the commissural projection of the rat somatic sensory cortex. JComp Neurol 1976;168(3):313-343.

53. Albers FJ, Meek J, Nieuwenhuys R. Morphometric parameters of the superior colliculus of albino and pigmented rats. JComp Neurol 1988;274(3):357-370.

54. Edwards MA, Caviness VS, Jr., Schneider GE. Development of cell and fiber lamination in the mouse superior colliculus. JComp Neurol 1986;248(3):395-409.

55. White NS, Dale AM. Optimal diffusion MRI acquisition for fiber orientation density estimation: An analytic approach. Human Brain Mapping 2009:In press.

# Chapter 6

# Optimal MRI Acquisition for Fiber Orientation Distribution Estimation

## 6.1 Abstract

An important challenge in the design of diffusion MRI experiments is how to optimize statistical efficiency, i.e., the accuracy with which parameters can be estimated from the diffusion data in a given amount of imaging time. In model-based spherical deconvolution analysis, the quantity of interest is the fiber orientation density (FOD). Here, we demonstrate how the spherical harmonics (SH) can be used to form an explicit analytic expression for the efficiency of the minimum variance (maximally efficient) linear unbiased estimator of the FOD. Using this expression, we calculate optimal b-values for maximum FOD estimation efficiency with SH expansion orders of $L$ = 2, 4, 6, and 8 to be approximately $b$ = 1500, 3000, 4600, and 6200 sec$^2$/mm, respectively. However, the arrangement of diffusion directions and scanner-specific hardware limitations also play a role in determining the realizable efficiency of the FOD estimator that can be achieved in practice. We show how some commonly used methods for selecting diffusion directions are sometimes inefficient and propose a new method for selecting diffusion directions in MRI based on maximizing the statistical

efficiency. We further demonstrate how scanner-specific hardware limitations generally lead to optimal b-values that are slightly lower than the ideal b-values. In summary, the analytic expression for the statistical efficiency of the unbiased FOD estimator provides important insight into the fundamental tradeoff between angular resolution, b-value, and FOD estimation accuracy.

## 6.2 Introduction

Diffusion tensor imaging (DTI) is an established non-invasive MR technique for studying the microstructural properties of brain white matter (WM) tissue *in vivo* (1,2). In DTI, all information about the tissue microstructure is inferred from the eigensystem of the estimated water diffusion tensor at each voxel. Commonly, the primary eigenvector is used to indicate the principal direction of WM fiber bundles, and the eigenvalues, are used to describe features of the diffusion process, such as the degree of fractional anisotropy (FA) (3). However, a well-known limitation of DTI is its inability to resolve complex tissue microstructures (e.g. crossing or bending WM fibers) due to the reliance on a single Gaussian diffusion function in each voxel. This shortcoming has motivated the development of high angular resolution acquisition and processing methods capable of modeling the complex diffusion patterns observed in heterogenous fiber populations. These new "multi-fiber" methods generally fall within one of two categories. The first is based on modeling high angular features of the apparent diffusion coefficient (ADC) (4-8), while the second is based on estimating the water displacement probability density function (PDF) or related functions (9-15). Within the second class of methods are the model-free and model-based techniques. In this paper, we focus on optimizing the statistical efficiency of one of the most popular model-based techniques.

A number of model-free approaches have been used to describe diffusion in complex tissue microstructures. Diffusion spectrum imaging (DSI) provides a direct quantification of the water diffusion PDF by exploiting the Fourier relationship between the PDF and the normalized diffusion signal (14). The radial integral of the PDF, called the orientation density function (ODF), describes the likelihood of water diffusion along any direction in three-dimensional (3D) space and can be used to map multiple fiber orientations within voxels (14). However, DSI is limited by the prohibitively long scan times required to adequately sample q-space on the Cartesian grid necessary for Fourier inversion. However, the ODF can be numerically approximated using the Funk-Radon transform in a technique called Q-ball imaging (QBI) (13), or computed analytically using the diffusion orientation transform (DOT) (16). Both of these methods can be implemented using less sampling intensive spherical q-space acquisitions called high angular resolution diffusion imaging (HARDI) acquisitions (8,17,18).

While model-free methods provide important information regarding the water diffusion PDF they do not provide a quantitative description of the underlying distribution of fibers or diffusion properties within these fibers. Model-based methods, on the other hand, impose additional mathematical constraints on the diffusion process in order to estimate these quantities directly. One model-based approach is to impart a persistent angular structure (PAS) to the PDF prior to estimation (15). Another model-based approach is to estimate the fiber orientation density (FOD) through deconvolution of the HARDI signal with a single-fiber response function (9-12). Spherical deconvolution reconstruction of the FOD is an attractive approach to modeling HARDI data because it gives an estimate of a well-defined biological quantity, namely the density of fibers oriented along a particular direction in 3D space, which can be validated quantitatively against myeloarchitecture (19).

A significant challenge in the design and analysis of any HARDI experiment is to maximize the statistical efficiency, or equivalently, the accuracy with which microstructural information can be inferred from the diffusion measurements in a given amount of imaging time. While numerous promising techniques have been developed for estimating the FOD from HARDI measurements (9-12,20,21), a focused study into the optimal HARDI acquisition for FOD estimation has not been conducted to the best of our knowledge. Here, we expand on previous works using the spherical harmonic (SH) basis to derive a simple analytic expression for the efficiency of the maximally efficient linear unbiased estimator for the FOD. We then show how the actual efficiency of the FOD estimate differs from the ideal efficiency depending on the gradient sampling scheme of the acquisition and practical constraints on the pulse-sequence parameters due to scanner-specific hardware limitations. Finally, we discuss how these expressions can be used for optimizing the b-value and directional sampling of the HARDI acquisition.

## 6.3 Methods

### 6.3.1 Linear convolution model

In the following, we assume a linear convolution model for the observed diffusion signal. According to this model, the response to any arbitrary angular distribution of fibers is equal to the sum of the individual responses to each fiber. More formally, the measured diffusion signal $S(b,\mathbf{r})$ in each voxel is given by the spherical convolution

$$\frac{S(b,\mathbf{r})}{S_0} = \int_{\Omega} R(b,\mathbf{r},\mathbf{x})\, f(\mathbf{x}) d\mathbf{x} + n(b,\mathbf{r}), \qquad [6.1]$$

where $b$ is the diffusion weighting factor, or "b-value", $\mathbf{r}$ is a unit (column) vector indicating the direction of the applied diffusion gradient, $S_0$ is the signal measured with no diffusion weighting (i.e. $S_0 \equiv S(b=0)$), $R(\cdot,\cdot,\mathbf{x})$ is the signal response to a single *ideal* fiber with orientation given by the unit (column) vector $\mathbf{x}$, $f(\cdot)$ is a real-valued function of the unit sphere describing the fiber orientation density (FOD), $n(b,\mathbf{r})$ is additive measurement noise, and $\int_\Omega$ indicates integration of the unit sphere.

Note, in a typical HARDI experiment the data are collected using a discrete set of $M$ evenly distributed and unique diffusion directions $\{\mathbf{r}_i\}_{i=1}^{M}$ with constant (non-zero) b-value, together with one or more measurements with $b=0$ for normalization. Given $N$ desired FOD reconstruction points on the surface $\{\mathbf{x}_i\}_{i=1}^{N}$, Eq. [6.1] can be written in matrix form

$$\bar{\mathbf{s}} = \mathbf{R}\mathbf{f} + \bar{\mathbf{n}}, \qquad [6.2]$$

where $\bar{\mathbf{s}} = [S(b,\mathbf{r}_1)/S_0, \cdots, S(b,\mathbf{r}_M)/S_0]^T$ is a vector of normalized diffusion measurements, $\mathbf{f} = [f(\mathbf{x}_1), \cdots, f(\mathbf{x}_N)]^T$ is a vector representation of the FOD, and $\mathbf{R}$ is an $M \times N$ linear convolution matrix relating the FOD to the normalized measurement data. Assuming an axially symmetric tensor model (22) for the single-fiber response function, the $ij$-th entry of $\mathbf{R}$ can be written

$$(\mathbf{R})_{ij} = e^{-b\cdot\lambda_\perp} e^{-b(\lambda_\parallel - \lambda_\perp)(\mathbf{r}_i^T \mathbf{x}_j)^2}, \qquad [6.3]$$

where $\lambda_\perp$ and $\lambda_\parallel$ are the perpendicular and parallel diffusivities (ADC parameters) with respect to the fiber axis $\mathbf{x}_j$, with $\lambda_\parallel \geq \lambda_\perp$, and the inner product $\mathbf{r}_i^T \mathbf{x}_j$ is the cosine of the angle between the $i$-th measurement direction and $j$-th fiber axis. While the tensor model in Eq. [6.3] assumes the single-fiber response function is Gaussian, non-Gaussian or hybrid models of diffusion (23) can also be used within this framework without any loss of generality.

### 6.3.2 SH basis

The SH form a complete orthonormal basis for functions on the sphere much like the Fourier series form a complete orthonormal basis for functions in Euclidian space. In this section, we show how the convolution matrix $\mathbf{R}$ can be expressed in terms of the SH basis. While similar expressions appear in earlier works (10,12), the focus here is to extend this framework to derive an analytic expression for the efficiency of the minimum variance (maximally efficient) linear unbiased estimator for the FOD, which can subsequently be used for optimizing the HARDI acquisition.

We begin by expressing the response function in Eq. [6.3] as a sum of Legendre polynomials $P_l(\cdot)$. Following (10) (Appendix A, Equation 36) we can write

$$e^{-b\lambda_\perp} \cdot e^{-b(\lambda_\parallel - \lambda_\perp)(\mathbf{r}_i^T \mathbf{x}_j)^2} = e^{-b\lambda_\perp} \cdot \sum_{\substack{l=0 \\ (l \text{ even})}}^{\infty} A_l(b(\lambda_\parallel - \lambda_\perp)) \cdot P_l(\mathbf{r}_i^T \mathbf{x}_j), \qquad [6.4]$$

where the scalar coefficients can be computed by evaluating the integral

$$A_l(b(\lambda_{\|}-\lambda_{\perp})) = \frac{2l+1}{2}\cdot\int_{-1}^{1} e^{-b(\lambda_{\|}-\lambda_{\perp})\tau^2} P_l(\tau)d\tau\,. \qquad [6.5]$$

Notice, only even orders $l = 0, 2, \cdots, \infty$ are considered in the expansion in Eq. [6.4] as the response function is symmetric around the fiber axis $\mathbf{x}_j$. Applying the Addition Theorem of Spherical Harmonics, we can write $P_l(\mathbf{r}_i^T\mathbf{x}_j)$ in terms of the spherical harmonics $Y_l^m(\cdot)$ evaluated in the direction of each vector (24)

$$P_l(\mathbf{r}_i^T\mathbf{x}_j) = \frac{4\pi}{2l+1}\cdot\sum_{m=-l}^{l} Y_l^m(\mathbf{r}_i)\cdot Y_l^{m^*}(\mathbf{x}_j)\,, \qquad [6.6]$$

where $l$ and $m$ are the order and degree of the spherical harmonic function, respectively, and $^*$ denotes the complex conjugate. Substituting Eq. [6.6] into Eq. [6.4] yields and expression for the $ij$-th entry of $\mathbf{R}$ in terms of the SH

$$(\mathbf{R})_{ij} = e^{-b\lambda_{\perp}}\cdot\sum_{\substack{l=0\\(l\text{ even})}}^{\infty}\frac{4\pi}{2l+1}A_l(b(\lambda_{\|}-\lambda_{\perp}))\cdot\sum_{m=-l}^{l} Y_l^m(\mathbf{r}_i)\cdot Y_l^{m^*}(\mathbf{x}_j)\,. \qquad [6.7]$$

Enumerating all measurement and reconstruction points, the full convolution matrix can be written as a weighted superposition of matrices having the form

$$\mathbf{R} = \sum_{\substack{l=0\\(l\text{ even})}}^{\infty} z_l \sum_{m=-l}^{l}\mathbf{y}_l^m(\mathbf{r})\mathbf{y}_l^{m^H}(\mathbf{x})\,, \qquad [6.8]$$

where it follows from Eq. [6.7] that

$$z_l = e^{-b\lambda_\perp} \cdot \frac{4\pi}{2l+1} A_l(b(\lambda_\parallel - \lambda_\perp)), \quad [6.9]$$

and the vectors of SH are

$$\mathbf{y}_l^m(\mathbf{r}) = \left[ Y_l^m(\mathbf{r}_1); Y_l^m(\mathbf{r}_2); \cdots; Y_l^m(\mathbf{r}_M) \right], \quad [6.10]$$

$$\mathbf{y}_l^m(\mathbf{x}) = \left[ Y_l^m(\mathbf{x}_1); Y_l^m(\mathbf{x}_2); \cdots; Y_l^m(\mathbf{x}_N) \right], \quad [6.11]$$

where $^H$ now denotes conjugate transpose.

Equation [6.8] indicates that the convolution matrix can be represented by an infinite sum of even order SH, weighted by the coefficients $z_l$. This is analogous to representing a delta function as an infinite series of Fourier basis functions. In practice, however, the number of diffusion directions, *M*, limits the maximum order that can be used in the expansion and thus the series must be truncated. Truncation of the SH series limits the angular resolution of the FOD much like truncating the Fourier series limits the bandwidth of reconstructed Cartesian signals.

Consider, for example, a maximum order of $L = 2$, such that $l = 0, 2$. Expanding Eq. [6.8], we can write an expression for the truncated convolution matrix, denoted $\mathbf{R}_L$

$$\mathbf{R}_L = \sum_{l=0,2} z_l \sum_{m=-l}^{l} \mathbf{y}_l^m(\mathbf{r}) \mathbf{y}_l^{m^H}(\mathbf{x}), \qquad [6.12]$$

$$= \begin{bmatrix} \mathbf{y}_0^0(\mathbf{r}) & \mathbf{y}_2^{-2}(\mathbf{r}) & \cdots & \mathbf{y}_2^2(\mathbf{r}) \end{bmatrix} \cdot \begin{bmatrix} z_0 & 0 & \cdots & 0 \\ 0 & z_2 & & 0 \\ \vdots & & \ddots & \vdots \\ 0 & 0 & \cdots & z_2 \end{bmatrix} \cdot \begin{bmatrix} \mathbf{y}_0^{0^H}(\mathbf{x}) \\ \mathbf{y}_2^{-2^H}(\mathbf{x}) \\ \vdots \\ \mathbf{y}_2^{2^H}(\mathbf{x}) \end{bmatrix}, \qquad [6.13]$$

$$= \mathbf{Y}_L(\mathbf{r}) \mathbf{Z}_L \mathbf{Y}_L^H(\mathbf{x}), \qquad [6.14]$$

where $\mathbf{Y}_L(\mathbf{r})$, $\mathbf{Z}_L$, and $\mathbf{Y}_L^H(\mathbf{x})$ have dimensions $M \times p$, $p \times p$, and $p \times N$, respectively, and $p(L) = (L+1)(L+2)/2$ is the number of terms (free parameters) in the SH series. For $L = 2$, $p(2) = 6$ and thus *M* should be greater than or equal to six to avoid an under-determined set of equations. Therefore, the number of diffusion directions, in effect, determines the upper bound on the angular resolution of the FOD, such that $(L+1)(L+2)/2 \le M$.

Inspection of Eqs. [4.12-4.14] yields several interesting properties of the FOD reconstruction problem. First, the SH form a natural basis for *both* the diffusion signal and the FOD, as it can be shown that the matrices $\mathbf{Y}_L(\mathbf{r})$ and $\mathbf{Y}_L(\mathbf{x})$ are unitary in the limit of $M, N \to \infty$ (25)

$$\mathbf{Y}_L^H(\mathbf{r}) \mathbf{Y}_L(\mathbf{r}) = (M / 4\pi)\mathbf{I}, \quad \text{as} \quad M \to \infty, \qquad [6.15]$$

$$\mathbf{Y}_L^H(\mathbf{x}) \mathbf{Y}_L(\mathbf{x}) = (N / 4\pi)\mathbf{I}, \quad \text{as} \quad N \to \infty. \qquad [6.16]$$

Second, when expressed in terms of the SH basis, the diffusion signal is simply a weighted sum of the FOD signal and vice versa (i.e. $\mathbf{Z}_L$ is diagonal) where the weighting is a function of the b-value and ADC of the single-fiber response model.

### 6.3.3 Estimation

Using the truncated convolution matrix, we can rewrite the signal equation in Eq. [6.2] as

$$\bar{\mathbf{s}} = \mathbf{R}_L \mathbf{f} + \bar{\mathbf{n}} . \qquad [6.17]$$

Then, assuming the noise $\bar{\mathbf{n}}$ is white with mean zero and variance $\sigma_n^2$, an efficient unbiased estimate of the FOD is provided by the ordinary least-squares (OLS) solution to Eq. [6.17]

$$\hat{\mathbf{f}} = (\mathbf{R}_L^H \mathbf{R}_L)^{-1} \mathbf{R}_L^H \bar{\mathbf{s}} \qquad [6.18]$$

$$= \mathbf{Y}_L(\mathbf{x}) \mathbf{Z}_L^{-1} \mathbf{Y}_L^H(\mathbf{r}) \bar{\mathbf{s}} . \qquad [6.19]$$

The OLS estimator for a linear model perturbed by white noise is optimal in the sense that it has the minimum variance among all linear unbiased estimators of the FOD. Note, however, $\hat{\mathbf{f}}$ is technically an unbiased estimator of the projection of the true FOD into the subspace spanned by the columns of $\mathbf{Y}_L(\mathbf{x})$. If part of the true FOD lies outside this subspace, for example, $\hat{\mathbf{f}}$ has higher angular frequency features not captured by the columns of $\mathbf{Y}_L(\mathbf{x})$,

then $\hat{\mathbf{f}}$ will be a biased (smoothed) estimate of the true FOD. $\hat{\mathbf{f}}$ can also be viewed as the truncated SVD solution.

### 6.3.4 Ideal efficiency

As mentioned previously, the OLS estimator has the lowest variance among all linear unbiased estimators of the FOD. The goal here is to determine the MRI pulse-sequence parameters which maximize the statistical efficiency. The efficiency of an estimator, which can also be viewed as a measure of the expected accuracy of the estimator, is typically defined as the reciprocal of estimator per unit scan time

$$E = \langle \| \mathbf{f} - \hat{\mathbf{f}} \|^2 \rangle^{-1} / T \,, \qquad [6.20]$$

where $\langle \cdot \rangle$ is the expectation operator and $T$ is the total time required for the acquisition. For simplicity, and without loss of generality, in the remainder of this paper we set $T = 1$ (i.e. assuming a constant scan time). Combining Eq. [6.19] with Eq. [6.20], we get the following expression for the efficiency of the OLS FOD estimator

$$E = \langle \| \mathbf{f} - \mathbf{Y}_L(\mathbf{x}) \mathbf{Z}_L^{-1} \mathbf{Y}_L^H(\mathbf{r}) \overline{\mathbf{s}} \|^2 \rangle^{-1} \qquad [6.21]$$

Substituting the expression for the normalized signal in Eq. [6.17] into Eq. [6.21] and simplifying, we get

$$E = \langle \| \mathbf{Y}_L(\mathbf{x}) \mathbf{Z}_L^{-1} \mathbf{Y}_L^H(\mathbf{r}) \overline{\mathbf{n}} \|^2 \rangle^{-1} \qquad [6.22]$$

Finally, recalling $\bar{\mathbf{n}}$ is white noise with mean zero and variance $\sigma_n^2$, we get the following expression for the efficiency of the OLS FOD estimator $\hat{\mathbf{f}}$

$$E = \frac{1}{\text{trace}(\sigma_n^2 / s_0^2 \cdot \mathbf{Z}_L^{-2})} \quad [6.23]$$

$$= \frac{1}{\sigma_n^2 / s_0^2 \cdot \sum_l z_l^{-2}} \quad [6.24]$$

$$= \text{SNR}^2 \cdot \frac{1}{\sum_l z_l^{-2}}, \quad [6.25]$$

where the root mean squared (RMS) signal-to-noise ratio (SNR) is defined as $\text{SNR} \triangleq s_0 / \sigma_n$. Eq. [6.25] together with Eq. [6.9] demonstrate how the ideal efficiency of the FOD estimate is a function of the b-value, the ADC of the single-fiber response, and the SNR at $b = 0$.

### 6.3.5 Realizable efficiency

The expression for the efficiency of the OLS FOD estimator in Eq. [6.25] is ideal in the sense that it assumes a continuous sampling of measurement directions and FOD reconstruction points (i.e. as $M, N \to \infty$) and pulse-sequence parameter that are independent of the b-value. In practice, however, the "realizable" efficiency of the FOD estimate depends on the efficiency of gradient sampling vectors in $\mathbf{q}$ and the dependence of the echo-time (TE) and repetition time (TR) on the b-value. Taken together, we can write an expression for the realizable efficiency $\tilde{E}$ (per unit scan time) as

$$\tilde{E} \approx \frac{\left(\mathrm{SNR}_0 \cdot e^{-\mathrm{TE}(b)/\mathrm{T}_2}\right)^2}{\mathrm{TR}(b)} \cdot \frac{1}{M \cdot \sum_i \gamma_i^{-2}(\mathbf{r},\mathbf{x})} \qquad [6.26]$$

where $\mathrm{SNR}_0$ is the SNR in RMS units at TE = 0 and $b$ = 0, $\gamma_i(\mathbf{r},\mathbf{x})$ is the $i$-th singular value of the forward convolution matrix $\mathbf{R}(\mathbf{r},\mathbf{x})$ (given by Eq. [6.3]), and $i = 1, 2, \cdots, p$ is the spherical harmonic index for an $L$-th order series expansion. The first term on the left hand side of Eq. [6.26] can be viewed as a reduction in efficiency due to constraints imposed by the pulse-sequence and scanner hardware, while the second term on the right hand side of Eq. [6.26] can be viewed as the relative efficiency of the gradient sampling scheme. Note, the expression for the realizable efficiency $\tilde{E}$ in Eq. [6.26] is no longer analytic, and requires computing the singular values numerically.

## 6.4 Results and Discussion

Figure 6.1 shows a plot of the magnitude coefficients $|z_l|$ computed analytically using Eq. [6.9] for several different b-values and fixed ADC parameters ($\lambda_{\parallel} = 1.7 \times 10^{-3}$ $\mathrm{mm}^2/\mathrm{sec}$ and $\lambda_{\perp} = 0.2 \times 10^{-3}$ $\mathrm{mm}^2/\mathrm{sec}$). These ADC values are consistent with experimental estimates in the adult human brain (26), and are used throughout the remainder of this paper. Notice the characteristic "staircase" pattern for each plot in the figure, where each "step" corresponds to a different spherical harmonic order $l$. The heights of the steps

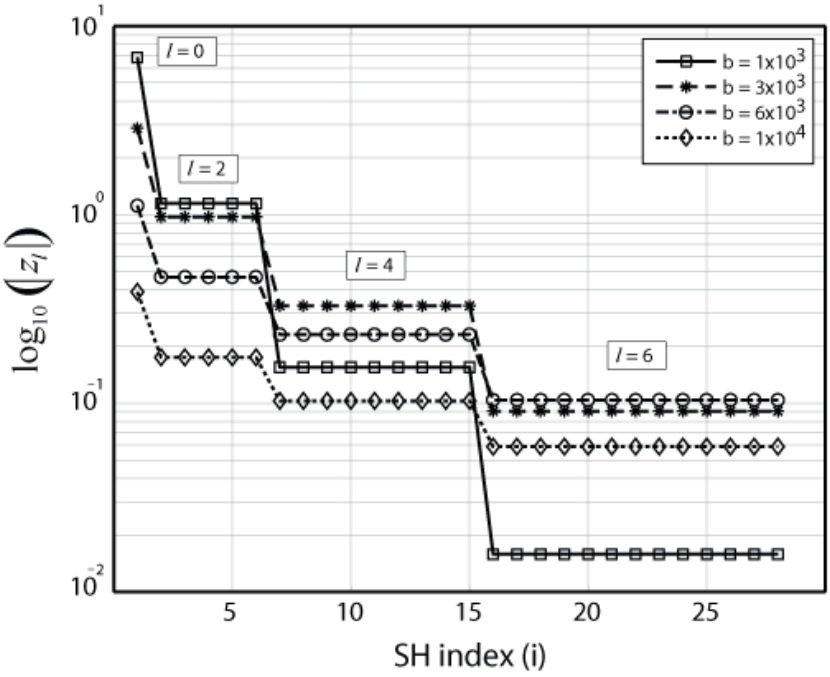


**Figure 6.1.** The magnitude of the coefficients $|z_l|$ are shown for four different b-values (sec$^2$/mm) with a maximum SH expansion order of $L = 6$. The height of each step reflects the relative power to estimate features of the FOD spanned by the corresponding SH basis vectors. As the b-value decreases, the relative power to estimate higher order angular frequency features of the FOD decreases.

reflect the relative power to estimate features of the FOD spanned by the corresponding SH basis vectors. In all cases, power decreases with increasing SH order, reflecting an overall reduction in the ability to estimate higher angular frequency features of the FOD, irrespective of the b-value. However, the rate at which power is lost is also dependent on the b-value, with lower b-values resulting in greater losses in power to estimate higher angular frequency components of the FOD.

Figure 6.1 can also be viewed as a plot of the analytic singular values of $\mathbf{R}_L$. Small singular values cause the inverse solution in Eq. [6.18] to become increasingly sensitive to small amounts of noise in the data. Several authors have introduced various linear and non-linear regularization techniques to better condition both the FOD and ODF reconstruction

problem, including Tikhonov regularization (27), Laplace-Beltrami regularization (21,28), non-negative least squares (11,20,29), and Maximum Entropy (9). These regularization techniques can decrease the mean squared error of the estimate, but this comes at a price of introducing estimator bias. The performance of each regularization method is critically dependent on whether the *a priori* constraints imposed on the solution are valid. The efficiency optimization approach presented here is valid for unbiased estimators where the estimation error is driven solely by the measurement error. The expression for the truncated SVD solution in Eq. [6.19] provides an optimum unbiased estimator of the projection of the true FOD into the subspace spanned by the columns of $\mathbf{Y}_L(\mathbf{x})$.

The overall efficiency of the unbiased FOD estimate in Eq. [6.25] takes into account the relative power to estimate *all* the angular frequency components of the FOD. Figure 6.2 shows a plot of the ideal FOD estimation efficiency $E$ as a function of b-value for $L$ = 2, 4, 6, and 8. Again, note the decrease in efficiency for estimating FODs with higher order series expansions (and thus greater angular resolutions). Also, note the optimal b-value which maximizes the efficiency depends on the expansion order, with higher order expansions requiring higher b-values. The optimal b-values which maximize the ideal efficiency of the FOD estimator using $L$ = 2, 4, 6, and 8 are $b$ = 1500, 3000, 4600, and 6200 sec$^2$/mm, respectively.

Figures 6.1 and 6.2 illustrate the fundamental relationship between angular resolution, b-value, and estimation efficiency. The theoretical angular resolution of a $L$-th order SH expansion can be quantified using the angular point spread function (PSF) (27). The full-width at half maximum (FWHM) of the main lobe of the PSF determines the upper bound on angular resolution and is inversely proportional to $L$. For $L$ = 2, 4, 6, and 8 the theoretical

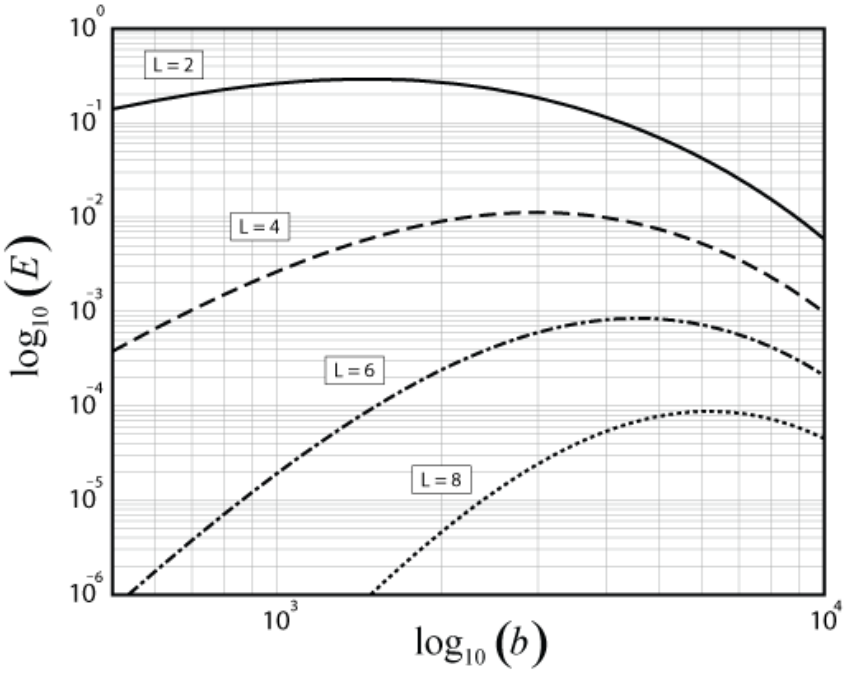


**Figure 6.2.** Relative ideal efficiency $E$ of the OLS FOD estimator is plotted as a function of b-value (sec$^2$/mm) for four different SH expansion orders $L$. Note that the exact value of the ideal efficiency is proportional to the SNR, and thus the relative efficiency measure plotted here is in arbitrary units assuming an SNR = 1. Optimal b-values which maximize the ideal efficiency for $L$ = 2, 4, 6, and 8 are $b$ = 1500, 3000, 4600, and 6200 sec$^2$/mm, respectively.

angular resolution of the FOD estimator is approximately 110º, 65º, 46º, and 36º, respectively (27). Thus, in practice, increasing $L$ would allow for resolving crossing fibers at increasingly finer separation angles, but as mentioned earlier, this comes at a price of decreasing efficiency. From Fig. 6.2 one can see that using an expansion order of $L$ = 6 at the optimal value of $b$ = 4600 is approximately 10 times less efficient than using an $L$ = 4 expansion at its optimal value of $b$ = 3000 ($1\times10^{-2}/9\times10^{-4} \approx 10$) and 300 times less efficient than using a tensor description for the FOD ($L$ = 2) at its optimal value of $b$ = 1500 ($3\times10^{-1}/9\times10^{-4} \approx 300$).

In addition to the expansion order $L$, the b-value also plays a critical role in determining the efficiency of the FOD estimator, especially when higher order expansions are used. For example, inspection of Fig. 6.2 reveals that the efficiency for estimating the

diffusion tensor ($L$ = 2) is fairly constant between $b$ = 500 and $b$ = 3000, but then falls off rapidly at higher b-values. However, the efficiency for estimating crossing fibers ($L \geq 4$) is more strongly dependent on the b-value. Scanning at $b$ = 1000 using $L$ = 4 would result in approximately 1/3 the efficiency of scanning at its optimum value of $b$ = 3000 ($3\times10^{-3}/1\times10^{-2} \approx 1/3$). This means one would have to collect three times as many diffusion directions, or equivalently, three times as many averages at $b$ = 1000 to achieve the same estimation accuracy as scanning at $b$ = 3000. On the other hand, scanning at $b$ = 2000 would only result in a 10% drop in efficiency when compared to $b$ = 3000 ($9\times10^{-3}/1\times10^{-2} \approx 9/10$).

While the expression for the ideal efficiency in Eq. [6.25] provides important insight into the FOD estimation problem, in practice, the realizable efficiency of the FOD estimator also depends on the arrangement of diffusion directions on the sphere (term on the right hand side of Eq. [6.26]) and scanner-specific hardware constraints (term on the left hand side of Eq. [6.26]). Two of the most commonly used methods for selecting diffusion directions in MRI are to 1) minimize the electrostatic energy of pairs of equal and opposite points on the sphere, called the electrostatic repulsion (ER) model (30), and 2) to minimize the 1/r potential, which we call the minimum potential (MP) model (Hardin, Slone, and Smith, Spherical Codes, published electronically at www.research.att.com/~njas/electrons/index.html). Shown in Fig. 6.3 are the relative efficiencies of both models for expansion orders $L$ = 2, 4, 6, and 8. Also included is the efficiency of an “optimized” set of diffusion directions generated by searching for sampling arrangements which maximize Eq. [6.26]. We refer to this new method for selecting diffusion directions as the "optimal efficiency" (OE) model. As illustrated in Fig. 6.3 some sampling arrangements of the MP model are highly inefficient for estimating the FOD with $L > 2$ (i.e. for reconstructing crossing fibers). The ER model, on the other hand, achieves

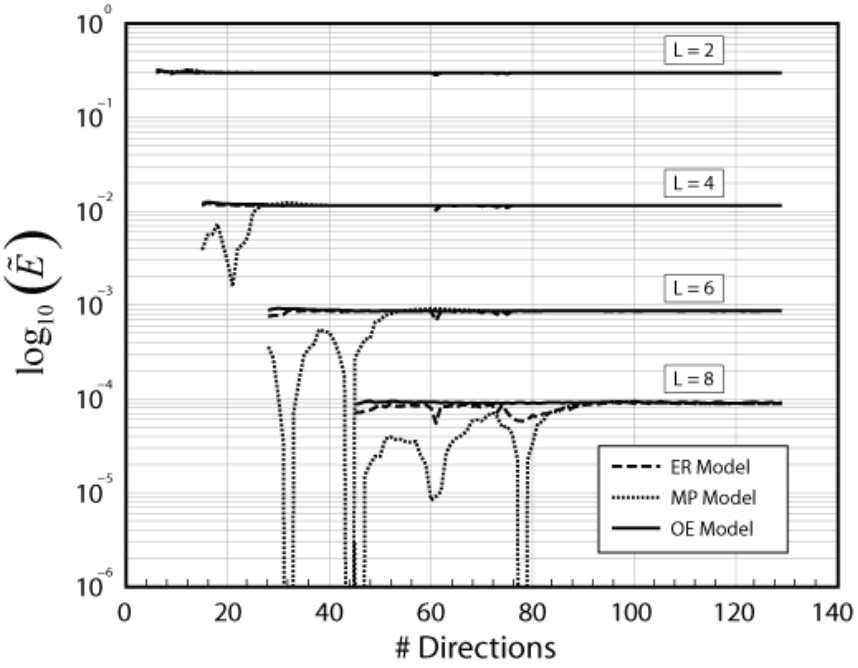


**Figure 6.3.** Effect of gradient sampling scheme on the realizable efficiency $\tilde{E}$ of the FOD estimator. Shown are the relative efficiencies of the electrostatic repulsion (ER) model, minimum potential (MP) model, and the newly proposed "optimal efficiency" (OE) model. For each order $L$, the efficiency is calculated using their respective optimal b-values and plotted in arbitrary units (term on the left hand side of Eq. [6.26] was set to 1). The FOD reconstruction vectors $\mathbf{x}$ were chosen using a 2-nd order icosahedral sampling of the sphere (162 vertices).

nearly optimal efficiency for $L \leq 6$, but has suboptimal efficiency for some sampling arrangements when using $L = 8$ and presumably for higher orders as well.

Another important factor in the realizable efficiency of the FOD estimator is the minimal TE and TR allowed for a given b-value. The effects of these scanner-specific hardware constraints on the FOD estimation efficiency are illustrated in Fig. 6.4. Shown in black are the efficiencies of a 51 direction acquisition (selected using the ER model) for multiple expansion orders using TE and TR values that are consistent with those prescribed on a General Electric Signa HDx 1.5T scanner (Waukesha, WI). Shown in gray are the efficiencies of this same acquisition using a fixed TE and TR calculated at $b = 500$ for reference. From Fig. 6.4 one can see that the general effect of adjusting the TE and TR is to

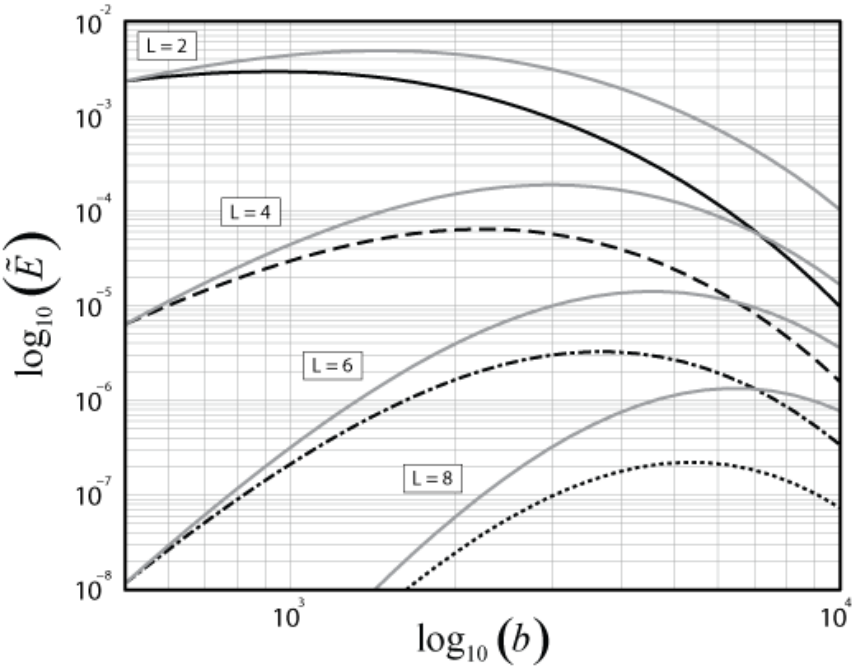


**Figure 6.4.** Effect of scanner-specific hardware constraints on the realizable efficiency $\tilde{E}$ of the FOD estimator. Black lines show the relative efficiencies of a 51 direction acquisition (selected using the ER model) using realistic TE and TR values that are consistent with those prescribed in practice. Gray lines show the relative efficiencies of the same acquisition using a fixed TE and TR calculated at $b = 500$. All efficiencies are calculated numerically using $SNR_0 = 1$, T2 = 80 msec., and a 2-nd order icosahedral sampling for the FOD reconstruction vectors $\mathbf{x}$.

reduce the efficiency at higher b-values which results in slightly lower b-values for optimal FOD estimation efficiency compared to the ideal case. For $L = 2, 4, 6, 8$ the optimal b-values which maximize the realizable efficiency on a Signa Hdx 1.5T system are approximately $b = 1000$, 2200, 3600, and 5200, respectively. Note that under these realistic conditions the relative efficiency for estimating crossing fibers using $L = 4$ at $b = 1000$ only now results in about half the efficiency of scanning at its optimum value of $b = 2200$ (compared to 1/3 the efficiency in the ideal case). Also, it should be noted that while the actual change in efficiency will vary depending on the scanner specifics, the general trend will remain the same, i.e., a reduction in the efficiency at higher b-values and a subsequent decrease in the optimal b-values required for maximally efficient FOD estimation.

## 6.5 Conclusion

Several authors have used the SH basis to derive analytic expressions for both the FOD and ODF reconstruction problem. Here, we extend this framework and derive a simple analytic expression for the efficiency of the maximally efficient (minimum variance) linear unbiased estimator of the FOD. This expression highlights the important fundamental relationship between angular resolution, b-value, and the expected accuracy of the FOD estimate per unit scan time. As expected, the FOD estimation efficiency decreases with increasing SH expansion order $L$ (increasing angular resolution) and the relative efficiencies at each order vary as a function of the b-value. b-values which maximize the efficiency under ideal conditions using $L$ = 2, 4, 6, and 8 are calculated to be approximately $b$ = 1500, 3000, 4600, and 6200 $sec^2/mm$, respectively.

However, the efficiency that can be realized in practice also depends on the arrangement of diffusion directions on the sphere and the scanner-specific hardware limitations. We demonstrate how some commonly used methods for selecting diffusion directions can lead to suboptimal FOD estimation efficiencies especially when higher order SH expansions are required, and we propose a new criterion for selecting diffusion directions based on optimizing the statistical efficiency. Finally, scanner-specific limitations on the TE and TR will tend to decrease the efficiency at higher b-values resulting in slightly lower b-values for optimal FOD estimation efficiency.

## 6.6 Acknowledgements

Funding for this work was provided by GE Healthcare Inc. Chapter 6, in full, is a reprint of the material as it appears in Human Brain Mapping: *Optimal Diffusion MRI*

*Acquisition for Fiber Orientation Density Estimation: An Analytic Approach*, Nathan S. White, and Anders M. Dale, 2009. The dissertation author was the primary investigator and first author of this paper.

## 6.7 References


1. Basser PJ, Mattiello J, LeBihan D. Estimation of the effective self-diffusion tensor from the NMR spin echo. J Magn Reson B 1994;103:247-254.

2. Basser PJ, Pierpaoli C. Microstructural and physiological features of tissues elucidated by quantitative-diffusion-tensor MRI. J Magn Reson B 1996;111:209-219.

3. Le Bihan D. Molecular diffusion, tissue microdynamics and microstructure. NMR Biomed 1995;8:375-386.

4. Frank LR. Characterization of anisotropy in high angular resolution diffusion-weighted MRI. Magn Reson Med 2002;47:1083-1099.

5. Ozarslan E, Mareci TH. Generalized diffusion tensor imaging and analytical relationships between diffusion tensor imaging and high angular resolution diffusion imaging. Magn Reson Med 2003;50(5):955-965.

6. Descoteaux M, Angelino E, Fitzgibbons S, Deriche R. Apparent diffusion coefficients from high angular resolution diffusion imaging: estimation and applications. Magn Reson Med 2006;56(2):395-410.

7. Zhan W, Gu H, Xu S, Silbersweig DA, Stern E, Yang Y. Circular spectrum mapping for intravoxel fiber structures based on high angular resolution apparent diffusion coefficients. Magn Reson Med 2003;49(6):1077-1088.

8. Alexander DC, Barker GJ, Arridge SR. Detection and modeling of non-Gaussian apparent diffusion coefficient profiles in human brain data. Magn Reson Med 2002;48(2):331-340.

9. Alexander DC. Maximum entropy spherical deconvolution for diffusion MRI. Inf Process Med Imaging 2005;19:76-87.

10. Anderson AW. Measurement of fiber orientation distributions using high angular resolution diffusion imaging. Magn Reson Med 2005;54:1194-1206.

11. Dell'Acqua F, Rizzo G, Scifo P, Clarke RA, Scotti G, Fazio F. A model-based deconvolution approach to solve fiber crossing in diffusion-weighted MR imaging. IEEE Trans Biomed Eng 2007;54:462-472.

12. Tournier JD, Calamante F, Gadian DG, Connelly A. Direct estimation of the fiber orientation density function from diffusion-weighted MRI data using spherical deconvolution. Neuroimage 2004;23:1176-1185.

13. Tuch DS. Q-ball imaging. Magn Reson Med 2004;52:1358-1372.

14. Wedeen VJ, Hagmann P, Tseng WY, Reese TG, Weisskoff RM. Mapping complex tissue architecture with diffusion spectrum magnetic resonance imaging. Magn Reson Med 2005;54:1377-1386.

15. Jansons KM, Alexander DC. Persistent Angular Structure: new insights from diffusion MRI data. Dummy version. Inf Process Med Imaging 2003;18:672-683.

16. Ozarslan E, Shepherd TM, Vemuri BC, Blackband SJ, Mareci TH. Resolution of complex tissue microarchitecture using the diffusion orientation transform (DOT). Neuroimage 2006;31(3):1086-1103.

17. Tuch DS, Reese TG, Wiegell MR, Makris N, Belliveau JW, Wedeen VJ. High angular resolution diffusion imaging reveals intravoxel white matter fiber heterogeneity. Magn Reson Med 2002;48(4):577-582.

18. Frank LR. Anisotropy in high angular resolution diffusion-weighted MRI. Magn Reson Med 2001;45(6):935-939.

19. White NS, Leergaard TB, Bolstad I, Bjaalie JG, D'Arceuil H, de Crespigny A, Dale AM. Quantitative histological validation of fiber-orientation distributions based on high-angular resolution diffusion imaging.; 2008; Proc 16th Annual Meeting of the ISMRM, Toronto, Canada.

20. Tournier JD, Calamante F, Connelly A. Robust determination of the fibre orientation distribution in diffusion MRI: non-negativity constrained super-resolved spherical deconvolution. Neuroimage 2007;35:1459-1472.

21. Sakaie KE, Lowe MJ. An objective method for regularization of fiber orientation distributions derived from diffusion-weighted MRI. Neuroimage 2007;34:169-176.

22. Hsu EW, Mori S. Analytical expressions for the NMR apparent diffusion coefficients in an anisotropic system and a simplified method for determining fiber orientation. Magn Reson Med 1995;34:194-200.

23. Assaf Y, Freidlin RZ, Rohde GK, Basser PJ. New modeling and experimental framework to characterize hindered and restricted water diffusion in brain white matter. Magn Reson Med 2004;52(5):965-978.

24. Arfken GB, H.J. W. Mathematical methods for physicists. San Diego: Academic Press; 2005.

25. Nelson PA, Kahana Y. Spherical harmonics, singular-value decomposition and the head-related transfer function. Journal of Sound and Vibration 2001;239:607-637.

26. Pierpaoli C, Jezzard P, Basser PJ, Barnett A, Di Chiro G. Diffusion tensor MR imaging of the human brain. Radiology 1996;201:637-648.

27. Hess CP, Mukherjee P, Han ET, Xu D, Vigneron DB. Q-ball reconstruction of multimodal fiber orientations using the spherical harmonic basis. Magn Reson Med 2006;56(1):104-117.

28. Descoteaux M, Angelino E, Fitzgibbons S, Deriche R. Regularized, fast, and robust analytical Q-ball imaging. Magn Reson Med 2007;58(3):497-510.

29. Jian B, Vemuri BC. Multi-fiber reconstruction from diffusion MRI using mixture of Wisharts and sparse deconvolution. Inf Process Med Imaging 2007;20:384-395.

30. Jones DK, Horsfield MA, Simmons A. Optimal strategies for measuring diffusion in anisotropic systems by magnetic resonance imaging. Magn Reson Med 1999;42:515-525.

# Chapter 7

# Real-time Motion Correction

## 7.1 Abstract

Artifacts caused by patient motion during scanning remain a serious problem in most MRI applications. The prospective motion correction technique attempts to address this problem at its source by keeping the measurement coordinate system fixed with respect to the patient throughout the entire scan process. In this study, a new image-based approach for prospective motion correction is described, which utilizes three orthogonal 2D spiral navigator acquisitions (SP-Navs) along with a flexible image-based tracking method based on the Extended Kalman Filter (EKF) algorithm for online motion measurement. The SP-Nav/EKF framework offers the advantages of image-domain tracking within patient-specific regions-of-interest and reduced sensitivity to off-resonance-induced corruption of rigid-body motion estimates. The performance of the method was tested using offline computer simulations and online in vivo head motion experiments. In vivo validation results covering a broad range of staged head motions indicate a steady-state error of the SP-Nav/EKF motion estimates of less than 10 % of the motion magnitude, even for large compound motions that included rotations over 15 degrees. A preliminary in vivo application in 3D inversion recovery spoiled gradient echo (IR-SPGR) and 3D fast spin echo (FSE) sequences demonstrates the effectiveness of the

SP-Nav/EKF framework for correcting 3D rigid-body head motion artifacts prospectively in high-resolution 3D MRI scans.

## 7.2 Introduction

Artifacts caused by patient motion during scanning remain a serious problem in most clinical and research MRI applications. In fast single-shot sequences, such as dynamic 2D echo-planar imaging (EPI), *between*-scan motion can introduce significant motion-related variance to the voxel-time courses and disrupt the spin excitation history of the acquisition (1,2). In multi-shot 2D and 3D sequences, *within*-scan patient motion results in *k*-space data inconsistencies, causing artifacts such as ghosting, blurring and ringing in the images themselves. Offline image registration can mitigate most between-scan motion artifacts in time-series data (3-5), but cannot correct for changes in the spin excitation history caused by through-plane motion. In addition, while some *within*-scan motion artifacts can be corrected retrospectively using knowledge of the motion history derived from either navigator scans (6,7) or overlapping *k*-space data (8,9), most of these methods are limited by the inability to 1) fully correct for through-plane motion in 2D sequences and 2) avoid *k*-space data inconsistencies caused by interpolation errors.

An alternative approach to motion correction, which shares none of these drawbacks, is modify the pulse-sequence online, in real-time, during the acquisition itself. Some of the first real-time methods used straight-line navigators to prospectively correct for linear translations of organs in the chest (10-12). Since then, navigators with more sophisticated *k*-space trajectories have been developed for higher order motion correction. Ward et al. used orbital (circular) navigators (O-Navs) (13) acquired in three orthogonal 2D planes for prospective correction of full 3D rigid-body motion artifacts in 2D EPI (14). To account for

motion outside the plane of each navigator (through-plane motion effects), multiple O-Navs are acquired in series where each O-Nav provides an adjustment to the subsequent O-Nav planes. Spherical navigators (S-Navs), which generalize the O-Nav trajectory to 3D shells in *k*-space, do not suffer from through-plane motion effects and can be used to estimate 3D rigid-body motion in a single navigator (15-17). However, the spherical technique works best for rotations along the navigator trajectory as apposed to rotations across them (15). In addition, a real-time application of the S-Nav remains missing due in part to the slow iterative procedure required to register S-Nav magnitude data (15). One of the most recent real-time navigator techniques, introduced by van der Kouwe (18), used an optimized "cloverleaf" *k*-space trajectory for prospective correction of 3D rigid-body motion in 3D spoiled gradient echo sequences. Compared to the orbital and spherical trajectories, the cloverleaf method offers the advantages of a more rapid *k*-space readout, together with improved translation estimation by including linear segments through the center of *k*-space (18).

In some applications, prospective motion correction can be achieved through self-navigation. Thesen et al. described a self-navigated approach for 2D EPI called “Prospective Acquisition CorrEction", or PACE, where each individual time-series volume is reconstructed online and registered to the first volume in the sequence (19). While the image-base tracking (registration) procedure in PACE provides accurate 3D rigid-body motion estimates, the correction itself is performed on a slow volume-by-volume basis, or approximately every four seconds (19). Zaitsev et al. (20) and Speck. et al. (21) developed an optical tracking device for improved real-time slice-by-slice correction in 2D EPI. In general, the advantage of optical tracking is that it does not require modification of the pulse-sequence. However, this comes at a price of requiring significant additional hardware to implement, including a MRI compatible

camera system mounted inside the scanner room and repeated calibration for optimal tracking performance (22).

In this study, we present an alternative image-based framework for prospective motion correction called "PROMO" (PROspective MOtion correction). The PROMO approach utilizes three orthogonal 2D spiral navigator acquisitions (SP-Navs) along with a flexible image-based tracking method based on the Extended Kalman Filter (EKF) algorithm (23,24) for real-time motion measurement. The Kalman filter framework for image-based tracking in MRI was introduced by White et al. (25), and applied in 3D spiral-navigated image sequences by Shankaranarayanan et al. (26,27) and Roddey et al. (28) and in MR spectroscopy by Keating et al. (29). Spincemaille et al. also recently introduced a novel application of the Kalman filter for real-time separation of cardiac and respiratory components in navigator data (30). Here, we describe the PROMO motion correction method in detail and provide some preliminary results in 3D inversion recovery spoiled gradient echo (IR-SPGR) and fast spin echo (FSE) sequences.

## 7.3 Methods

### 7.3.1 Spiral navigator acquisition

The navigator acquisition included three orthogonal low flip-angle, thick-slice, single-shot spiral acquisitions (SP-Navs) with the following pulse-sequence parameters: TE/TR = 3.4/14 ms, Flip ($\delta$) = 8$^{o}$ (to minimize the impact of signal saturation on the acquired 3D volume), BW = $\pm$ 125 kHz, field-of-view (FOV) = 32 cm, effective in-plane resolution = 10 x 10 mm, reconstruction matrix = 128 x 128, slice thickness = 10 mm. Spiral readouts were selected because they provide an efficient *k*-space coverage and allow for image-based

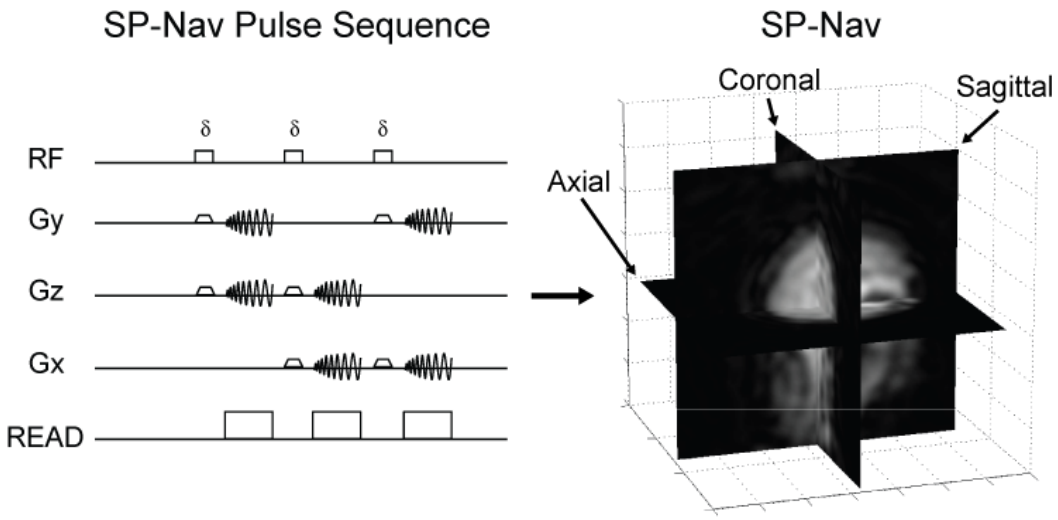


**Figure 7.1**. SP-Nav pulse-sequence and reconstructed image used for motion tracking.

tracking with reduced sensitivity to distortion. The off-resonance effect is somewhat mitigated by the optimization of spiral length since the requirement for the in-plane resolution of the navigators is not very high. Initial experiments were done without any trajectory measurement. However, it should be noted that in case of severe off-resonance ($> \pm 100$ Hz) the measurement errors will increase significantly. To avoid this, we perform center frequency correction (prescan software on the scanner) before every scan. The orientation convention adopted in this work defined the x-axis as the left-right direction, the y-axis as the anterior-posterior direction, and the z-axis as the inferior-superior direction with respect to the patient. The axial, sagittal, and coronal planes of each SP-Nav spanned the x-y, y-z, and the x-z axes, respectively. The SP-Nav pulse-sequence and example reconstructed image is shown in Fig. 7.1.

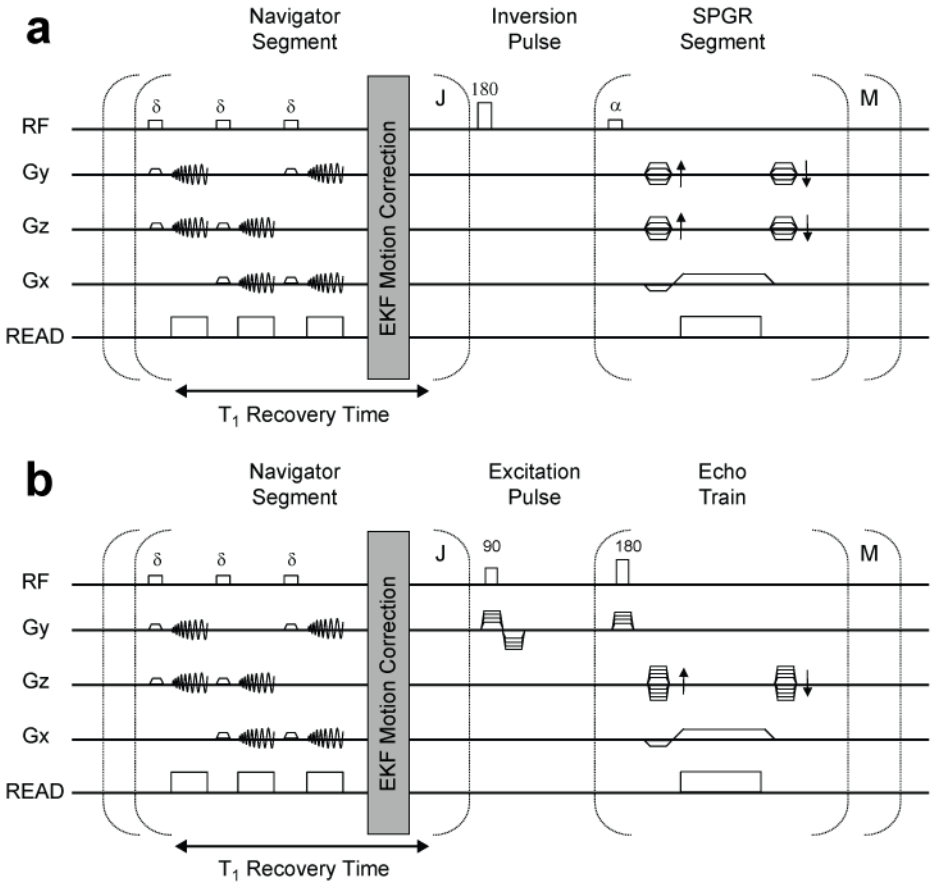


**Figure 7.2**. Spiral-navigated (**a**) 3D IR-SPGR and (**b**) 3D FSE pulse-sequence. A train of $J = 5$ SP-Navs are played out prior to each of the $M$ inversion or excitation pulses of the two sequences, respectively. Prospective motion correction is performed after each individual SP-Nav using the EKF algorithm.

### 7.3.2 Integration in 3D IR-SPGR and 3D FSE

SP-Navs were integrated into a 3D IR-SPGR and 3D FSE sequence (Fig. 7.2). To enable prospective correction without impacting scan time, multiple SP-Navs were played out during the intrinsic longitudinal ($T_1$) recovery time of the two sequences. Immediately after acquisition, each SP-Nav was reconstructed and used as input to the EKF motion tracking and correction algorithm (described next). The time required to collect a single SP-Nav was approximately 42 ms, followed by 6 ms for image reconstruction of all three planes. To allow ample time for estimation and feedback, the repetition time for each SP-Nav was programmed

for 100 ms. A total of J = 5 SP-Navs (~500 ms) were acquired during the $T_1$ recovery times of both sequences, which were programmed for approximately 700 ms and 1200 ms, respectively. For the IR-SPGR sequence, a recessed elliptical centric ky-kz ordering was used for the imaging segment (31), with an entire ky-kz plane acquired after each inversion pulse. The thickness of the IR pulse was twice that of the imaging slab. The IR-SPGR pulse-sequence parameters were: TE/TR = 3.9/8.7 ms, Inversion time (TI) = 270 ms, Flip ($\alpha$) = 8º, BW = $\pm$ 15.63 kHz, FOV = 24 cm, voxel size = 1.25 x 1.25 x 1.2 mm, # *k*-space segments (M) = 192. For the 3D FSE sequence, an eXtended Echo Train Acquisition (XETA) (32) was used with the following parameters: TE/TR = 110/2500 ms, Flip = 90º, BW = $\pm$ 31.25 kHz, FOV = 24 cm, voxel size = 1.25 x 1.25 x 1.2 mm, echo train length (ETL) = 90, M = 90. The overall scan times of the IR-SPGR and FSE sequences were 8 min and 4.5 min, respectively. All scans were collected using a 1.5T GE Signa HDx system (Waukesha, WI) using an 8-channel head coil.

## 7.3.3 EKF motion tracking and correction

### 7.3.3.1 Dynamic state space model

Real-time 3D rigid-body motion tracking and correction on the SP-Nav data was performed using the well-known EKF algorithm (23). The EKF itself provides recursive state estimates in nonlinear dynamic systems perturbed by Gaussian noise. The basic dynamic state-space model of the EKF, as implemented here, is shown in Fig. 7.3 and can be written as a set of system equations of the form

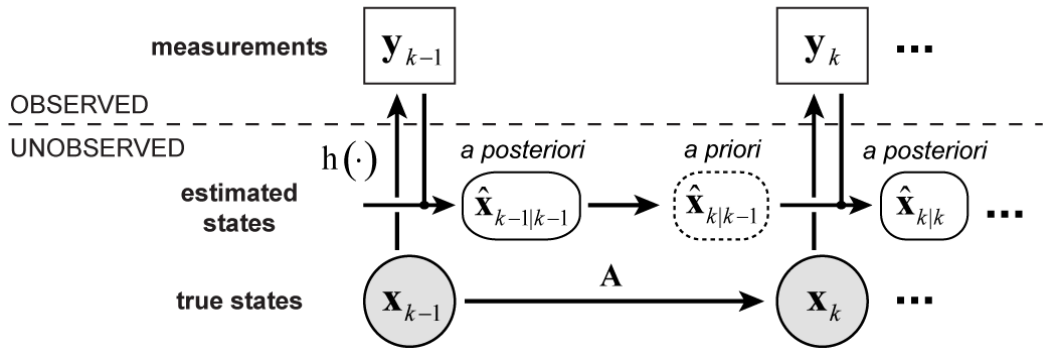


**Figure 7.3**. Dynamic state space model of the EKF. The *a priori* state is used to update the pulse-sequence at each time step.

$$\mathbf{x}_k = \mathbf{A}\mathbf{x}_{k-1} + \mathbf{w}; \quad P(\mathbf{w}) \sim N(0, \mathbf{Q}) \qquad [7.1]$$

$$\mathbf{y}_k = \mathrm{h}(\mathbf{x}_k) + \mathbf{v}; \quad P(\mathbf{v}) \sim N(0, \mathbf{R}). \qquad [7.2]$$

$\mathbf{x}_k$ is the (unobserved) state of the dynamic system at time-step *k* and $\mathbf{y}_k$ are the (observed) measurements. Also shown in Fig. 7.3 are the EKF state estimates, which are described in detail later.

For image-based motion tracking, $\mathbf{x}_k = [t_x, t_y, t_z, \theta_x, \theta_y, \theta_z]^T$ is a 6-dimensional vector of rigid-body motion parameters, where the first three and last three elements are translations and rotations in x-y-z space, respectively and $\mathbf{y}_k$ is an $N_v$-dimensional vector of voxel intensities of the *k*-th SP-Nav, where $N_v$ is the total number of voxels in all three navigator planes. The time evolution of the state vector is given by the 6 x 6 state transition matrix **A** and the Gaussian process noise by **w**, with mean zero and covariance **Q**. Because of the relatively unpredictable nature of patient head motions over the sampling interval of the SP-Navs, the dynamics are modeled using a simple random walk, with **A** as the identity

matrix. $\mathrm{h}(\cdot);\mathbb{R}^6 \to \mathbb{R}^N$ is a nonlinear vector-valued function of the current state called the measurement model, which describes how the states are observed through the noisy measurements. For image-based tracking, the measurement model $\mathrm{h}(\cdot)$ describes a 2D interpolation into a fixed reference navigator $\mathbf{y}_{\mathrm{ref}}$ (collected at the beginning of the scan) at the locations specified by $\mathbf{x}_k$. The exact mathematical form of $\mathrm{h}(\cdot)$ is provided in the Appendix. To improve the robustness of the tracking to potential variations in the mean signal level of each SP-Nav, the measurements $\mathbf{y}_k$ are forced to have unit norm at each time-step. The error in the measurement process is given by the Gaussian measurement noise **v**, with mean zero and covariance **R**. In the dynamic state-space model above, the noise processes are time-invariant and statistically independent (i.e. $E(\mathbf{w}\mathbf{v}^T) = 0$).

From a Bayesian point of view, the *a posteriori* filtering density $P\left(\mathbf{x}_k \middle| \mathbf{y}_{0:k}\right)$ of the state given the complete history of observations $\mathbf{y}_{0:k} = \{\mathbf{y}_0, \mathbf{y}_1, \ldots, \mathbf{y}_k\}$ constitutes the complete solution to the motion tracking problem. The EKF algorithm provides recursive estimates of the conditional mean of the *a posteriori* filtering density $\hat{\mathbf{x}}_{k|k} = E\left[\mathbf{x}_k \middle| \mathbf{y}_{0:k}\right] = \int \mathbf{x}_k P\left(\mathbf{x}_k \middle| \mathbf{y}_{0:k}\right) d\mathbf{x}_k$ using a two-stage recursion of *prediction* and *correction* at each time-step. Here, $\hat{\mathbf{x}}_{k|k}$ refers to the corrected, or *a posteriori* state estimate at time-step *k*, given *all* the measurements up to and including $\mathbf{y}_k$. For prospective motion correction in MRI, an additional scanner *update* step is included in the recursion.

#### 7.3.3.2 Prediction

In the prediction step, the state transition matrix **A** and assumed process noise covariance **Q** are used to predict the state and error covariance at each time-step. With **A** as the identity matrix, the predicted state and error covariance become

$$\hat{\mathbf{x}}_{k|k-1} = \hat{\mathbf{x}}_{k-1|k-1} \quad [7.3]$$

$$\hat{\mathbf{P}}_{k|k-1} = \hat{\mathbf{P}}_{k-1|k-1} + \mathbf{Q}, \quad [7.4]$$

where $\hat{\mathbf{x}}_{k|k-1}$ is the predicted or *a priori* state estimate at time-step *k*, given the *a posteriori* state estimate $\hat{\mathbf{x}}_{k-1|k-1}$ at the previous time-step *k*-1 (see Fig. 7.3). $\hat{\mathbf{P}}_{k|k-1} = E\left[\left(\mathbf{x}_k - \hat{\mathbf{x}}_{k|k-1}\right)\left(\mathbf{x}_k - \hat{\mathbf{x}}_{k|k-1}\right)^T\right]$ is *a priori* state estimation error covariance at time-step *k*, given the *a posteriori* state estimation error covariance $\hat{\mathbf{P}}_{k-1|k-1}$ at *k*-1.

#### 7.3.3.3 Update

For prospective motion correction, the predicted state $\hat{\mathbf{x}}_{k|k-1}$ of the EKF is used to *update* the scanner pulse-sequence prior to collecting the measurements $\mathbf{y}_k$. This includes updating the slice, phase, and frequency encoding of the imaging volume as well as the navigators, given the 3D translations and rotations in $\hat{\mathbf{x}}_{k|k-1}$. A real-time communication system described in Ref (33) and implemented as in Ref (34), was used for efficient and near real-time communication of SP-Nav data, EKF state estimates, and associated meta data between the EKF module and the scanner pulse-sequence/receive chain.

#### 7.3.3.4 Correction

Immediately following the scanner update, the measurements $\mathbf{y}_k$ are acquired and used to *correct* the predicted state $\hat{\mathbf{x}}_{k|k-1}$ and error covariance $\hat{\mathbf{P}}_{k|k-1}$. The basic idea of EKF correction is to approximate the nonlinear function $\mathrm{h}(\cdot)$ using a Taylor series expansion around $\hat{\mathbf{x}}_{k|k-1}$ and apply the standard linear Kalman filter equations to the new linearized model. In this study, the first-order iterated EKF correction was implemented (23), which truncates the Taylor series to first-order and iterates the correction a total of *N* times. The first-order iterated EKF correction is analogous to performing an online Gauss-Newton optimization of the following nonlinear cost function (35)

$$\begin{aligned} C_i\left(\mathbf{x}_k\right) = &\left(\mathbf{y}_k - \mathrm{h}\left(\mathbf{x}_k\right)\right)^T \mathbf{R}^{-1}\left(\mathbf{y}_k - \mathrm{h}\left(\mathbf{x}_k\right)\right) \\ &+\left(\mathbf{x}_k - \hat{\mathbf{x}}^i_{k|k-1}\right)^T \hat{\mathbf{P}}_{k|k-1}{}^{-1}\left(\mathbf{x}_k - \hat{\mathbf{x}}^i_{k|k-1}\right) \end{aligned} \qquad [7.5]$$

for i = 0, 1, …, *N*. When *N* is set to zero, the first-order iterated EKF correction reduces to the standard EKF correction. Details of how the cost function $C_i\left(\mathbf{x}_k\right)$ is minimized given the online updates to the scanner pulse-sequence are provided in the Appendix.

The first term on the left hand side of Eq. [7.5] is the “data prediction error” while the second term on the right hand side of Eq. [7.5] is the “model estimation error”. Note, most offline intensity-based image registration algorithms are based on iteratively minimizing the “data prediction error”, or some variant of this function. The EKF can therefore be viewed as a generalization of traditional intensity-based image registration that incorporates an additional

model for the dynamics and is uniquely suited for online applications because 1) it is causal in nature and 2) does not require iterating the cost function (by setting $N = 0$), which is important in time-sensitive applications. Thus, in the limit of infinitely large process noise covariance **Q,** the "model estimation error" is effectively ignored when minimizing the cost, and the EKF is analogous to traditional image-based least-square registration with *N* iterations. The weighting of the "data prediction error" and "model estimation error" to the overall cost depends on both error terms **Q** and **R**. Selection of these priors is an important step in optimal EKF performance and is described next.

#### 7.3.3.5 Filter tuning

Because the EKF is unchanged by scaling $\mathbf{Q}$ and $\mathbf{R}$ by the same factor, it is often convenient to define a single scalar that controls the relative weighting of the "data prediction" and "model estimation errors". To do this, we factor $\mathbf{Q}$ and $\mathbf{R}$ into

$$\mathbf{Q} = \sigma_w^2 \cdot \bar{Q} \qquad [7.6]$$

$$\mathbf{R} = \sigma_v^2 \cdot \bar{R}, \qquad [7.7]$$

where $\sigma_w^2$ and $\sigma_v^2$ are scalars, and $\bar{Q}$ and $\bar{R}$ are matrices of unit norm containing the structure of the respective noise processes. The ratio $S = \sigma_v^2 / \sigma_w^2$ then controls the effective "bandwidth" of the filter, with increased tracking ability on the one hand (high weighting of data information with low values of $S$) and increased noise suppression on the other (high weighting of model information with high values of $S$). Throughout the remainder of this work, we refer to $S$ as the "smoothness factor".

The noise covariance structure, or entries of $\bar{Q}$ and $\bar{R}$, can be selected to utilize prior knowledge about the object's dynamics and measurement errors, respectively. Given the physical constraints of the patient inside the MRI environment, some of the off-diagonal entries of $\bar{Q}$ will likely be non-zero. However, for the sake of simplicity, we assume each motion parameter is independent, thus $\bar{Q}$ is diagonal and can be written

$$\bar{Q} = \mathrm{diag}\left(\begin{bmatrix} 1^2 & 1^2 & 1^2 & (\pi/180)^2 & (\pi/180)^2 & (\pi/180)^2 \end{bmatrix}^T\right), \qquad [7.8]$$

where the first three and last three elements have units $mm^2/TN^2$ and $rad^2/TN^2$, respectively, with TN being the time between the onset of two consecutive SP-Navs. In addition, we assume the measurement errors are white, thus $\bar{R}$ is diagonal, and the inverse can be written

$$\bar{R}^{-1} = \begin{bmatrix} d_1 & 0 & 0 & 0 \\ 0 & d_2 & 0 & 0 \\ 0 & 0 & \ddots & 0 \\ 0 & 0 & 0 & d_{N_v} \end{bmatrix}. \qquad [7.9]$$

The scalars along the diagonal of $\bar{R}^{-1}$ $0 \le \{d_i\}_{i=1}^{N_v} \le 1$ provide a means of weighting the contributions of each voxel to the motion estimate and thus setting the appropriate weights $d_i$ to zero provides a principled approach for motion tracking within *a priori* regions-of-interest (ROIs). This procedure is described next.

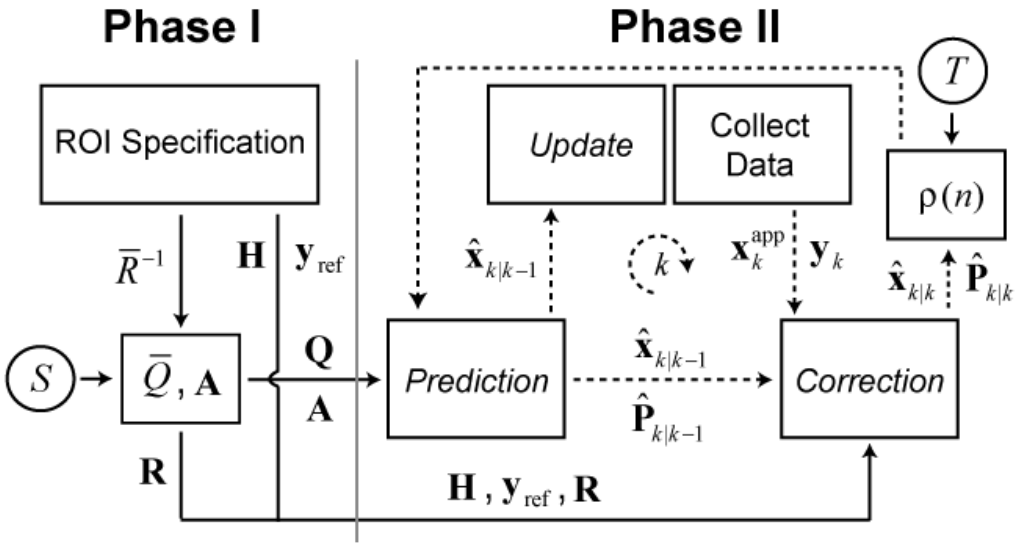


**Figure 7.4**. Online EKF schematic for patient-specific ROI tracking. $\mathbf{x}_k^{\text{app}}$ is the "applied" state used to collect the measurements $\mathbf{y}_k$ and is described in the Appendix.

### 7.3.3.6 ROI tracking

The advantage of image-based ROI tracking with the EKF is that the estimation can focus on a particular region (ROI) in object space while ignoring other regions that may corrupt the rigid-body motion estimates. In this study, a brain ROI is adapted to each patient to remove the effects of non-rigid motion of the neck and jaw. The general procedure is shown schematically in Fig. 7.4 and can be separated into two principal phases. During the first phase (Phase I), a train of 20 SP-Navs are played out in rapid succession immediately prior to the start of the "dummy" scans. During collection of this SP-Nav train, the EKF is used to register a fixed 3D proton density (PD) weighted head atlas to the patient. Once the registration is complete, the entries of $\bar{R}^{-1}$ (data weights) are set to the voxel values in a 3D binary brain mask, defined in atlas space. The construction of both the 3D head atlas and associated brain mask was performed offline and is described in detail in Ref (28). Immediately after the brain ROI is specified, a series of 4 dummy scans are acquired to allow equilibration of the

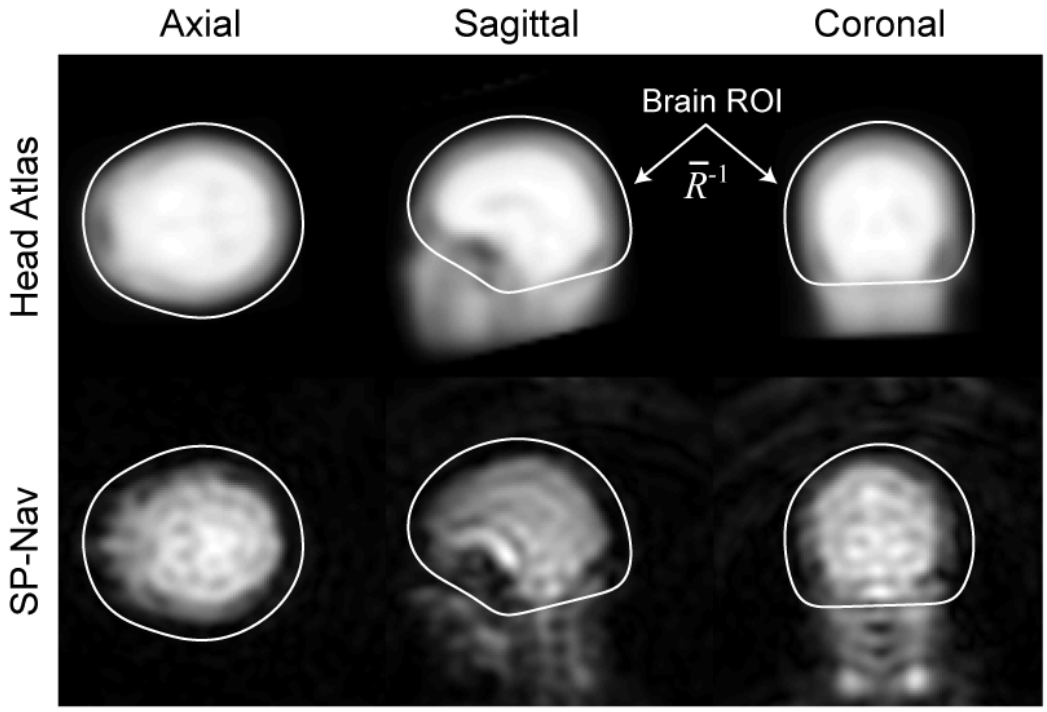


**Figure 7.5**. Results from Phase I of the EKF tracking procedure showing the SP-Nav reference image (bottom row), registered head atlas (top row), and brain ROI (white lines). All voxels outside of the brain ROI in the SP-Nav are ignored during tracking.

longitudinal magnetization. Once the dummy scans are complete, the final EKF parameters, such as the Jacobian **H** (see the Appendix for a description of the Jacobian and how it is calculated), reference navigator $\mathbf{y}_{\text{ref}}$ (which is set to the last SP-Nav prior to scan start) and covariance matrices **Q** and **R** are calculated and stored in memory. The entire duration of Phase I takes approximately 10 s. An example reference navigator, registered head atlas and brain ROI are shown in Fig. 7.5.

In the second phase (Phase II), the "tuned" EKF is run online for prospective motion correction during the scan. Because the SP-Navs are only acquired during the $T_1$ recovery period of the pulse-sequences, no correction is performed during the imaging segment itself, which typically lasts about 2 s. To account for this, motion corrupted *k*-space segments were

re-acquired at the end of the scan. To determine which segments needed to be re-acquired a simple “rescan metric” was defined

$$\rho(n) = \left\| \hat{\mathbf{x}}^{-}(n) - \hat{\mathbf{x}}^{+}(n) \right\|_2 , \qquad [7.10]$$

where $\hat{\mathbf{x}}^{-}(n)$ and $\hat{\mathbf{x}}^{+}(n)$ are used to denote the *a posteriori* motion estimates (in mm and deg) immediately prior and immediately after the collection of the *n*-th *k*-space segment, respectively. All *k*-space segments with $\rho(n)$ greater than or equal to a user-specified threshold *T* are then marked for rescanning. In this study, the rescan threshold was selected based on in vivo experiments performed during no motion and is described in the section titled “*In vivo validation experiment*”.

### 7.3.4 Offline simulation

Offline Monte Carlo simulations were used to test the performance of the EKF for motion tracking in the SP-Nav sequence. For each Monte Carlo run, a time-series of 10 SP-Navs was synthesized by interpolating into a single isotropic 3D SP-Nav volume (collected with similar acquisition parameters to the online 2D SP-Navs). To simulate online motion correction, the orientation of each synthesized SP-Nav was determined by combining both the simulated motion with the predicted state of the EKF at each time-point. Two different simulation experiments were performed. The first tested simple 1D motions in each parameter separately and the second tested compound random amplitude motions in all parameters simultaneously. In all experiments, step functions were used to simulate motion (starting at the forth time-point) so that the convergence behavior of the EKF could easily be visualized using

different filter parameters. Both “large” and “small” motions were tested using either a 10 mm/deg or 1 mm/deg step (for the 1D simulation experiment) or constraining the vector norm across all parameters (in mm and deg) to be either 10 or 1 (for the compound motion experiment), respectively. Prior to estimation, random Rician noise was added to each image with various signal-to-noise ratios (SNR). The measurement noise level $\sigma_v^2$ of the EKF was determined empirically for each SNR level using the mean (within brain) signal magnitude estimated from the native 3D SP-Nav volume. Thus, when testing the effect of different “smoothness factors” *S*, only the process noise level $\sigma_v^2$ of the EKF was varied. All simulations were performed on a Dell Precision workstation using Matlab (Mathworks, Inc.).

### 7.3.5 Online in vivo experiments

Three different types of in vivo experiments were performed to test the online performance of the SP-Nav/EKF tracking framework in the 3D IR-SPGR and 3D FSE sequences. Prior to scanning, all subjects provided informed consent in accordance with the University of California, San Diego institutional review board.

#### 7.3.5.1 In vivo validation experiment

The first in vivo experiment was designed to assess the steady-state accuracy of the SP-Nav/EKF motion estimates. The basic procedure consisted of modifying the IR-SPGR sequence (Fig. 7.2a) to collect the same three volumes back-to-back (V1, V2, and V3). During the scan, a highly motivated volunteer was instructed to either remain motionless throughout ("no-motion" trial), or make a single brief motion during the middle of the second volume (V2) and remain in that position until the end of the scan ("motion" trial). No instruction was

given as to what type of motion to perform, only to vary the magnitude and direction of motion from trial to trial. During each trial, prospective motion correction was performed with respect to the reference navigator of the first volume. After the scans were complete, three quantities were estimated for each trial: 1) the steady-state EKF motion estimate, calculated by averaging the online motion estimates during V3, 2) the steady-state error of the EKF motion estimates, calculated offline by registering V1 to V3 using an iterative 3D rigid-body registration algorithm, and 3) the "true" motion of the subject, calculated by combining the steady-state EKF estimate with the steady-state error. Prior to computing these quantities, all motion plots were inspected to verify the subject did not move during the collection of V1 or V3. Each trial of the validation experiment required approximately 24 minutes of scanning and a total of 15 trials were performed (2 "no motion" trials and 13 "motion trials"). The rescan threshold *T* was selected based on data obtained during the two "no motion" trials. The mean $\rho(n)$ during all six volumes of both trials was 0.31, with a minimum of 0.07 and a maximum of 0.68. Thus, to be conservative, the rescan threshold *T* was set to 1 for all subsequent in vivo scans in this study.

#### 7.3.5.2 Repeated staged motion experiment

The second in vivo experiment was designed to assess the performance of the SP-Nav/EKF framework for reducing 3D rigid-body head motion artifacts in the MRI scans themselves under relatively controlled conditions. Three types of scans were performed on a single subject: 1) a scan *without* motion correction where the subject was asked to perform repeated staged motions continuously during the scan (PROMO OFF condition), 2) a scan *with* motion correction where the subject was asked to repeat the same motions as in (1)

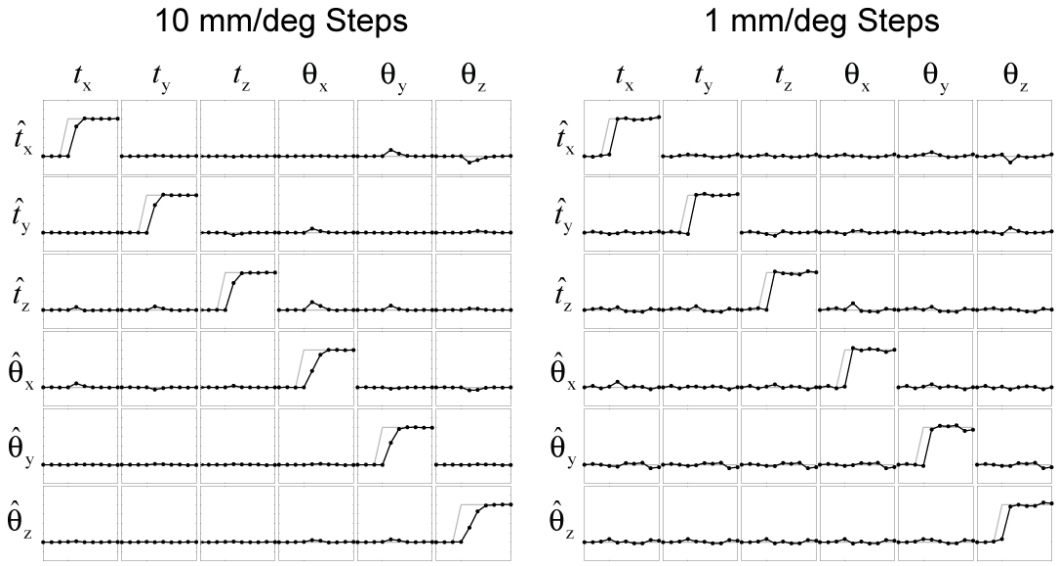


**Figure 7.6**. EKF tracking results for 1D motion steps. The true motion is shown in gray and the estimated motion in black. A total of 6 trials (columns) where used to create each 6 x 6 matrix. Off-diagonal plots indicate the "cross-talk" error of the EKF.

(PROMO ON condition), and 3) a baseline scan *without* motion correction where the subject was asked to stay as still as possible (NO MOTION condition). Two types of staged head motions were performed: 1) "side-to-side" motion and 2) "nodding" motion.

#### 7.3.5.3 Real life experiment

The final in vivo experiment was designed to assess the overall performance of the SP-Nav/EKF framework for reducing 3D rigid-body head motion artifacts in the MRI scans under realistic conditions. To do this, two healthy young males were scanned (ages 10 and 11) with the 3D IR-SPGR sequence with and without PROMO correction twice (total of 4 scans per subject). Young males were recruited because of their known tendency to move during the scan sequence despite being instructed not to. No specific instruction was given to either subject, only to remain "as still as possible".

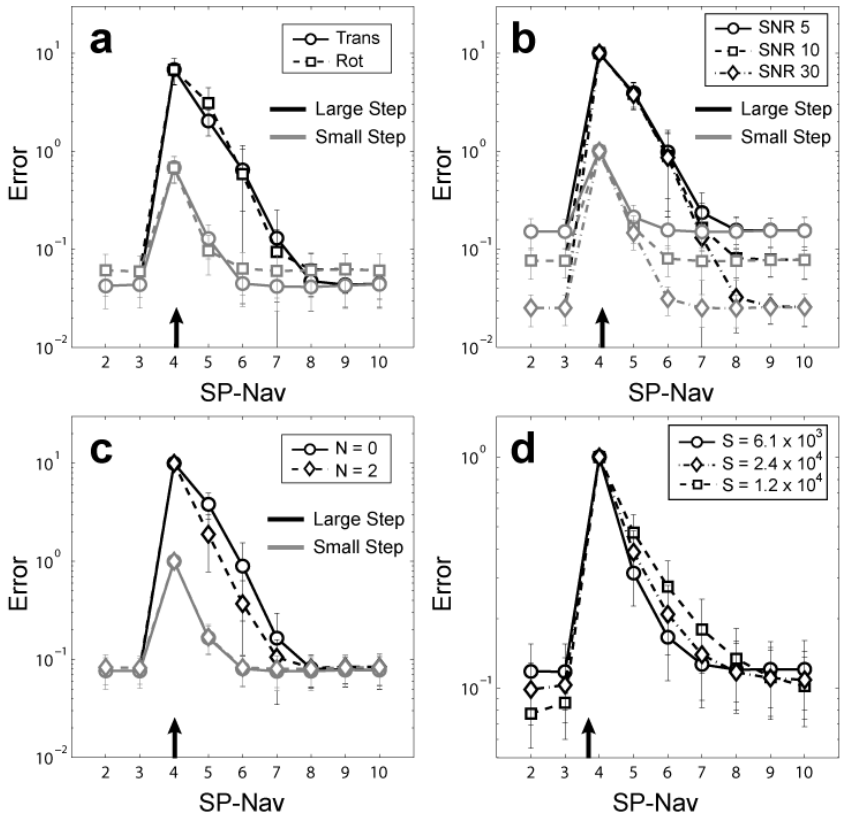


**Figure 7.7**. Average EKF tracking errors (over 500 Monte Carlo runs) for compound random amplitude motion steps plotted on a log scale. (**a**) Translation and rotation error for "large" and "small" motion steps. (**b**) Overall error (norm across all six parameters) as a function of SNR for "large" and "small" motion steps. (**c**) Overall error as a function of EKF iteration (*N*) for "large" and "small" motion steps with an SNR of 10. (**d**) Overall error as a function of "smoothness factor" *S* for "small" motion steps with an SNR of 10. In all plots, the arrow indicates the onset of the motion. Time-point 1 is omitted as the predicted state (motion) of the EKF is zero.

## 7.4 Results

### 7.4.1 Offline simulations

EKF tracking results for the 1D steps along each motion parameter are shown in Fig. 7.6 for both "large" (10 mm/deg) and "small" (1 mm/deg) motion magnitudes with an SP-Nav SNR of 10 (which approximates the actual SNR of the online SP-Navs). The results are shown in "matrix" format where the columns indicate the *simulated* parameter and the rows indicate

the *estimated* parameter. Not surprisingly, the error variance in the estimates due to noise is more apparent for the “small” sub-voxel motions than the “large” motions.

EKF tracking results for compound random amplitude motion steps are shown in Fig. 7.7. For all plots, the average norm error $\pm$ std over 500 Monte Carlo runs are shown. Figure 7.7a shows the norm error for translations and rotations. Figure 7.7b shows the effect of SNR on the overall (norm across all six parameters) EKF tracking error. Figure 7.7c shows the effect of adding additional iterations ($N$) on the overall tracking error for a fixed SNR of 10. Only $N = 2$ iterations are shown because increasing the number of iterations beyond this point had little effect on the tracking results (algorithm had converge to a local minimum). In Fig. 7.7a, b, and c, the “smoothness factor” is set arbitrarily low ($S = 6.1 \times 10^3$) to remove the weight of the “model estimation error” on the Kalman cost function and reducing $S$ any further had minimal effect on the tracking performance. Because only the “data prediction error” is used during estimation, one can interpret the iterated EKF in Fig. 7.7c as a standard image-based least-squares registration with $N$ iterations. Figure 7.7d shows the effect of increasing the “smoothness factor” (i.e., increasing the weight on the “model estimation error”) on the overall tracking error for “small” motions only with a fixed SNR of 10.

### 7.4.2 In vivo validation experiment

Results from the in vivo validation experiment are shown in Fig. 7.8. Online motion estimates for a single representative “motion-trial” are shown in Fig. 7.8a. Note how the subject made a single brief motion during the middle of V2 and remained fixed in this position throughout the remainder of the scan. The steady-state EKF motion estimates are plotted against the "true" motion of the subject for all 15 trials in Fig. 7.8b. The mean absolute steady-state error (MAE) ± std and mean magnitude of the “true” motion across all trials is shown in

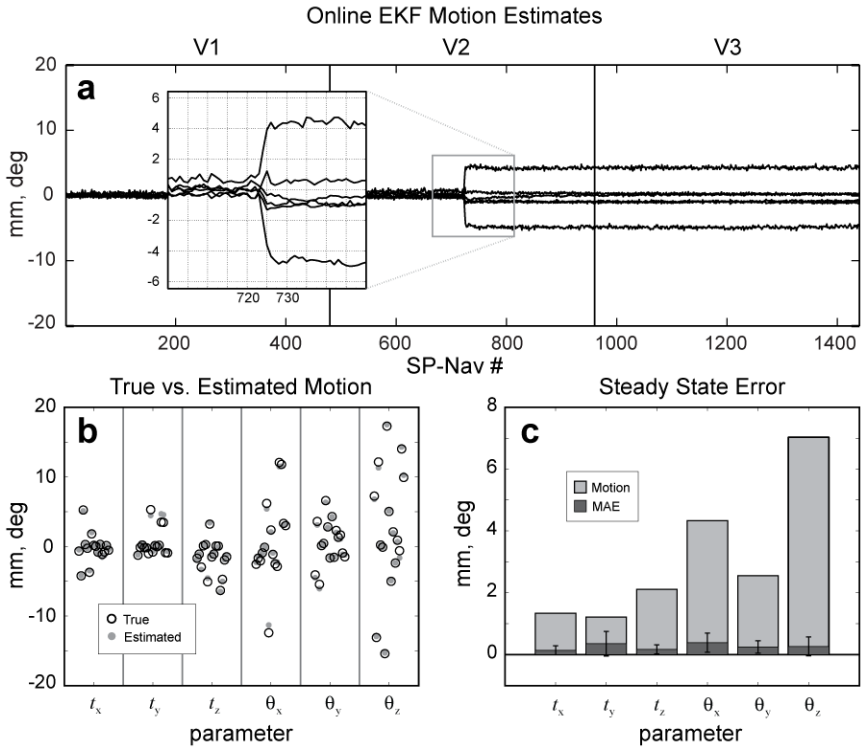


**Figure 7.8**. Results from the in vivo validation experiment. (**a**) Online motion estimates for a single representative "motion" trial. Insert shows a close-up of the tracking estimates during the motion onset interval. (**b**) The "true" vs. steady-state EKF motion estimates over all 15 experimental trials. (**c**) The mean absolute steady-state EKF error (MAE, dark gray) compared with the mean magnitude of the "true" motion (light gray) for each parameter across all trials.

Fig. 7.8c. The MAE ± std was calculated to be: $t_x = 0.14 \pm 0.15$ mm, $t_y = 0.35 \pm 0.39$ mm, $t_z = 0.17 \pm 0.15$ mm, $\theta_x = 0.39 \pm 0.31$ deg, $\theta_y = 0.25 \pm 0.20$ deg, and $\theta_z = 0.27 \pm 0.30$ deg. The mean magnitude of the "true" motion was calculated to be: $t_x = 1.34$ mm, $t_y = 1.22$ mm, $t_z = 2.11$ mm, $\theta_x = 4.33$ deg, $\theta_y = 2.55$ deg, and $\theta_z = 7.03$ deg. The overall steady-state error (mean across all parameters and trials) was 0.26 and the overall magnitude of motion (mean across all parameters and trials) was 3.09, which yields an expected overall steady-state error of less than 10 % of the true motion.

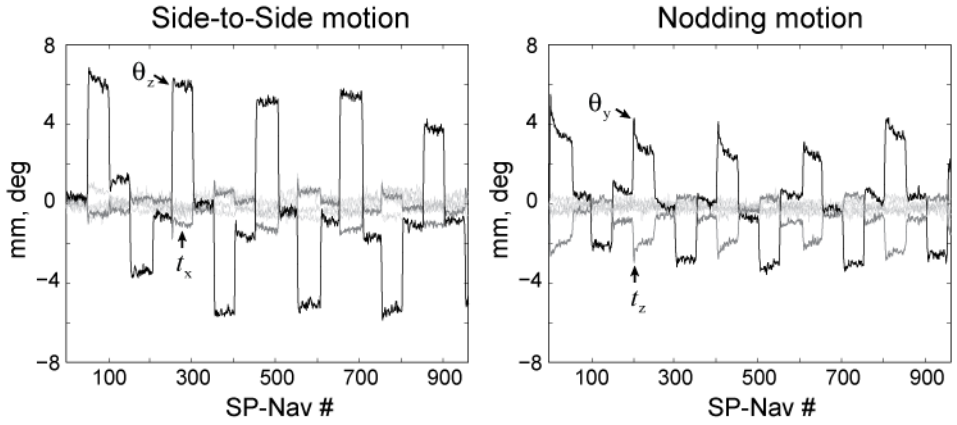


**Figure 7.9**. Example EKF motion estimates for the PROMO ON IR-SPGR scan during the "side-to-side" and "nodding" motion experiments.

### 7.4.3 Repeated staged motion experiment

Online EKF motion estimates obtained during the repeated staged "side-to-side" and "nodding" motion experiments for the two PROMO ON 3D IR-SPGR scans are shown in Fig. 7.9. As shown in the figure, "side-to-side" motion is characterized by rotations around the z-axis and translations around the x-axis, while "nodding" motion were characterized by rotations around the y-axis and translations around the z-axis. Although not shown, similar motion estimates were evident during all other "side-to-side" and "nodding" motion experiments.

The images from the repeated staged motion experiment are shown in Fig. 7.10. In order to compare corresponding slices, all reconstructed volumes were registered and resampled (using high dimensional sinc interpolation) to the NO MOTION 3D FSE volume. As evident in the figure, the PROMO corrected images have significantly reduced motion artifacts for both types of staged motion to a level that is qualitatively similar to the NO MOTION scans.

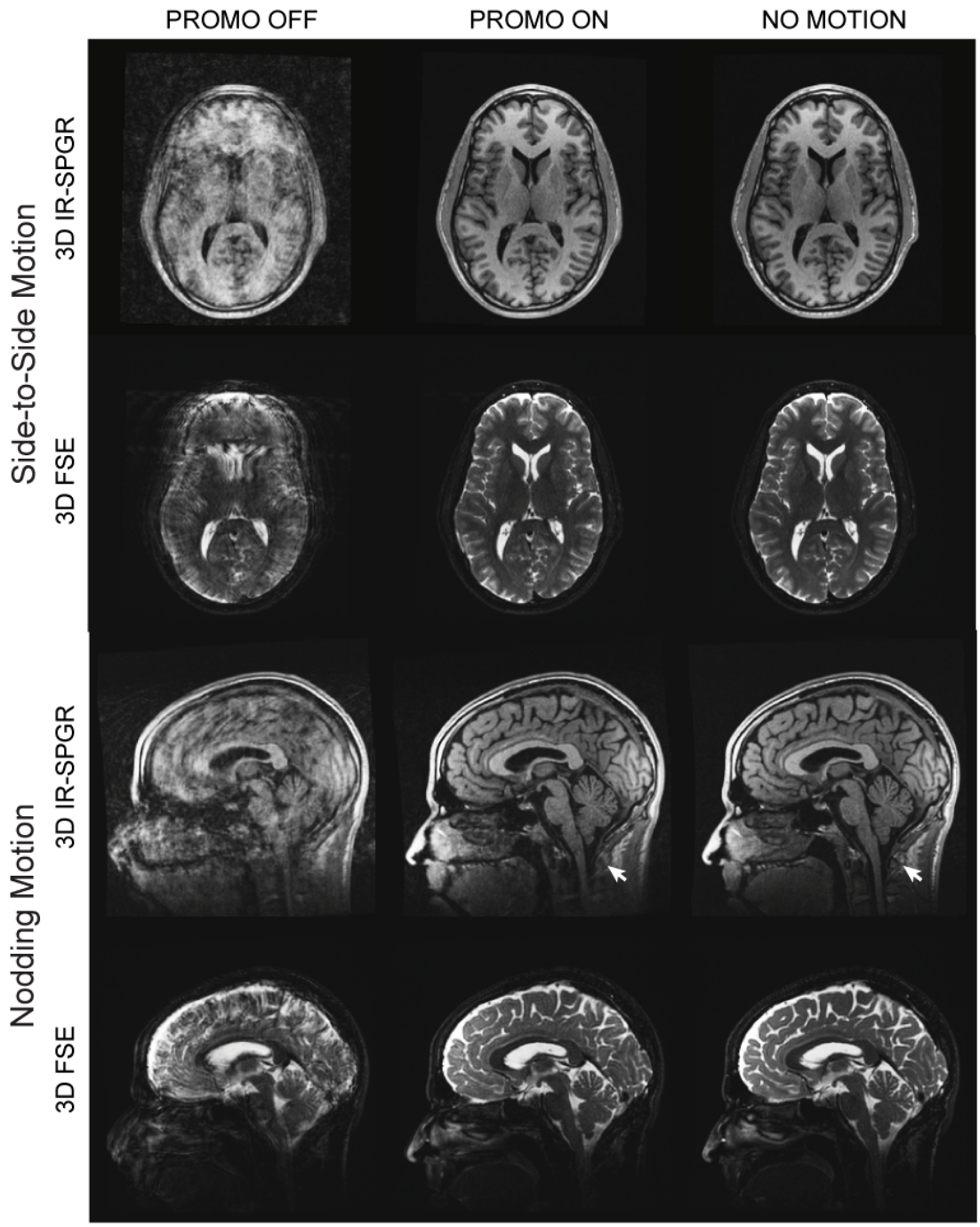


**Figure 7.10**. Reconstructed images for the repeated staged motion experiment. Only a single axial and sagittal slice through the volumes are shown. The number of rescanned *k*-space segments for the PROMO ON scans using a threshold of $T = 1$ were (from top to bottom) 20, 10, 35 and 5, respectively. The two images highlighted with arrows are shown again in Fig. 7.11.

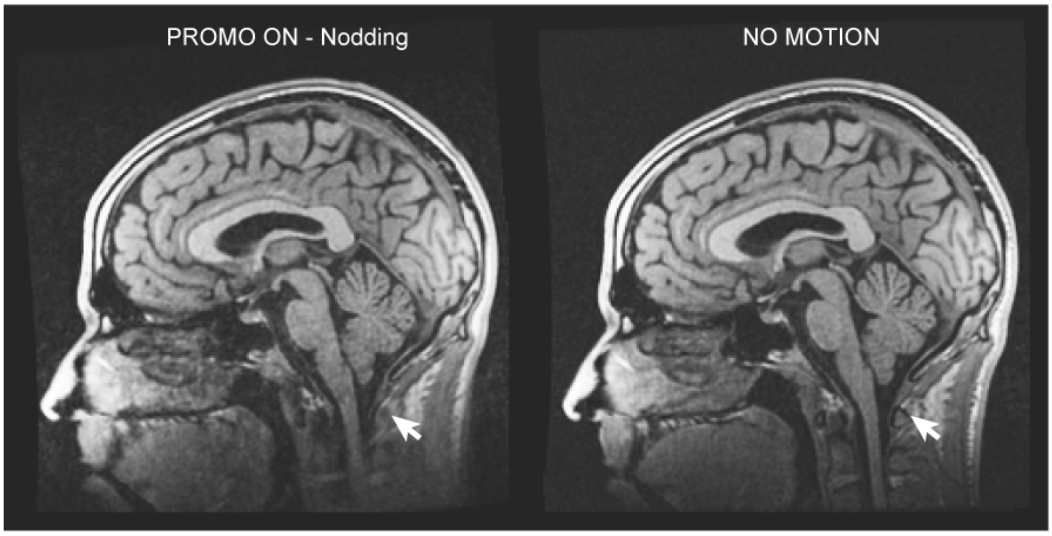


**Figure 7.11**. Comparison of the PROMO ON 3D IR-SPGR scan during "nodding" motion and the NO MOTION 3D IR-SPGR scan. White arrows highlight a region of the neck outside the brain ROI of the EKF, which moved non-rigidly during the scan and is subsequently uncorrected in the image.

A close-up of the PROMO ON and NO MOTION IR-SPGR sagittal slices shown in Fig 7.10 for the "nodding" motion experiment are shown by themselves in Fig. 7.11. The white arrows in the figure highlight an area of the neck outside the EKF brain mask that underwent non-rigid motion during the scan and was subsequently uncorrected in the final image.

### 7.4.4 Real life experiment

Corresponding coronal sections through the PROMO ON and PROMO OFF IR-SPGR scans for each of the two young male subjects are shown in Fig. 7.12. Both sets of PROMO ON and PROMO OFF scans were selected from the set of 4 to have qualitatively similar motion statistics as assessed with the "rescan metric" $\rho(n)$, also included in the figure. Again, the images with PROMO correction have significantly reduced motion artifacts

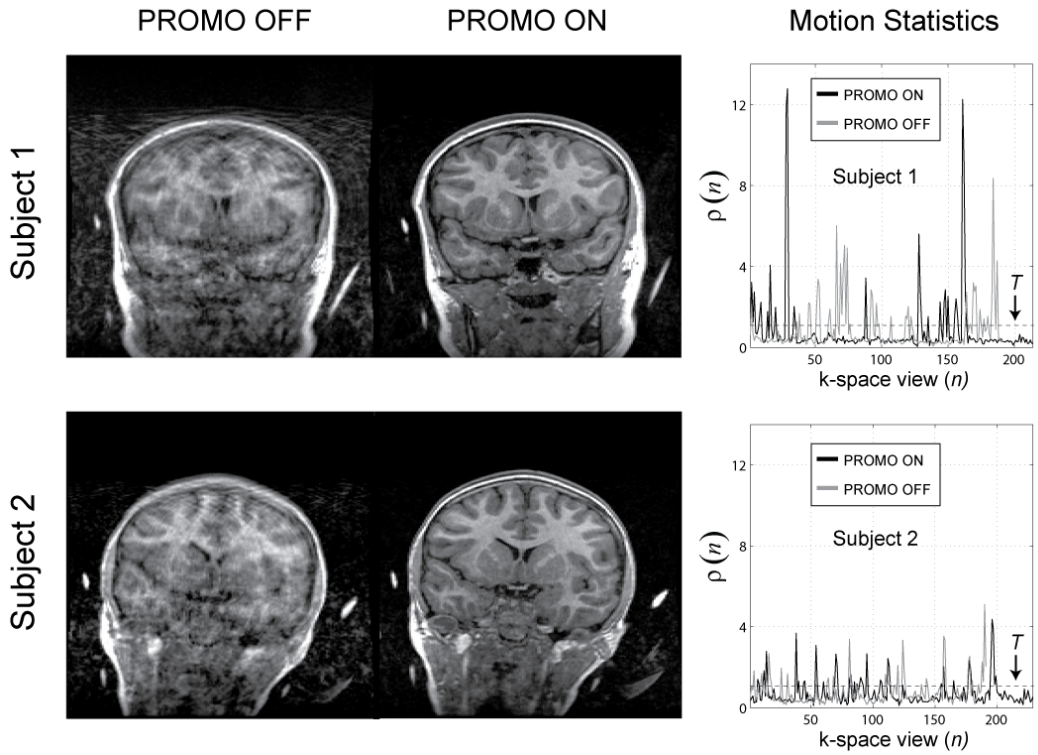


**Figure 7.12**. Real life images taken from two healthy young males with and without PROMO correction along with the "rescan metric" $\rho(n)$.

compared to the images without correction. The number of rescanned *k*-space segments for Subject 1 and Subject 2 using a threshold of $T = 1$ were 23 and 38, respectively.

## 7.5 Discussion

This work describes a new technique for prospective motion correction that utilizes three orthogonal 2D spiral navigator acquisitions (SP-Navs) along with a flexible image-based tracking method based on the EKF algorithm for online motion measurement. A preliminary application of the SP-Nav/EKF tracking framework in 3D IR-SPGR and 3D FSE pulse-sequences demonstrates the effectiveness of the approach for significantly reducing 3D rigid-body motion artifacts prospectively in these sequences.

### 7.5.1 Offline simulations

Offline simulations revealed some important properties of the SP-Nav/EKF framework for rigid-body motion tracking. Figure 7.6 demonstrated how both “large” and “small” 1D translations and rotations in all three degrees of freedom could be estimated with minimal transient “cross-talk” error. The term “cross-talk” error is used here to describe the apparent motion in one parameter due to motion in another (i.e. the off-diagonal plots in Fig. 7.6). While there was a tendency for rotations to have slightly larger “cross-talk” errors than translations, this effect was minimal and in general, both rotations and translations could be estimated with similar accuracy and precision.

Figure 7.7 shows the performance of the SP-Nav/EKF framework for tracking compound random amplitude motion steps using various filter parameters and SNR levels. Consistent with the 1D motion simulation results, Fig. 7.7a shows how translations and rotations could be estimated with similar accuracy and precision. Reducing the SP-Nav SNR increased the overall error due to noise (i.e. the baseline error when in the steady-state), but had little effect on the overall tracking error due to “large” and “small” compound motions, i.e. the filter response times (Fig. 7.7b). Thus, the number of SP-Navs (post motion onset) required to estimate “large” and “small” compound motions was relatively insensitive to SP-Nav SNR. Furthermore, increasing the number of EKF iterations ($N$) at each time-point (which increases the computation time significantly) was generally unnecessary, as it only marginally improved the overall tracking error for “large” compound motions but had no effect on the overall tracking error for “small” compound motions (Fig. 7.7c). An inspection of Fig 7.7a, b and c revealed that on average, 2-3 SP-Navs (post motion onset) were required to estimate “large” compound motions while only about 1-2 SP-Navs were required for

"small" compound motions, regardless of the number of EKF iterations. This result suggests that the majority of the transient SP-Nav/EKF tracking error comes from through-plane motion of the SP-Navs, which is greater for "large" compound motions. Transient tracking errors caused by through-plane motion was also observed using orthogonal 2D orbital navigators (14) and is likely to have contributed substantially to the transient "cross-talk" errors in the 1D simulations. However, as demonstrated in Fig. 7.6 and 7.7, this effect is mitigated when collecting multiple navigators back-to-back such that the through-plane motion component is reduced iteratively in time. The set of 5 SP-Navs played out during the 3D IR-SPGR or 3D FSE sequences should therefore be sufficient even in extreme situations where the patient makes a "large" transient motion during this interval.

Finally, varying the "smoothness factor" *S* (i.e., changing the degree to which the motion model influences the tracking estimates) resulted in a trade-off between increased noise suppression on the one hand (low filter bandwidths with high values of *S*) and reduced tracking error due to transient motion on the other (high filter bandwidths with low values of *S*). This is evidenced in Fig. 7.7d. Because the level of noise suppression was relatively small compared with the increase in overall tracking error, low "smoothness factors" (and no EKF iterations) were used for all subsequent in vivo scans. It should be noted that this finding is not surprising given 1) the large number of measurement voxels in each SP-Nav (effectively about 16,000 after masking) compared to the small number of rigid-body motion parameters to be estimated at each time-point and 2) the image SNR is relatively high (SNR = 10). Both of these factors suggest that the "data prediction error" should contribute more information to the Kalman cost than the "model estimation error". However, it should also be noted that although the model information played a relatively minor role in the current application of the Kalman filter for tracking in the SP-Nav sequence, in applications where 1) there is reduced

information in the measurements through either reduced SNR or number of imaging voxels (e.g., self-navigated head motion tracking in 2D EPI slice data), 2) there are more rapid image-based measurements available online, 3) there are more than six parameters in the state vector (e.g. modeling non-rigid motion or including velocity terms), and 4) there are strong regularities over time in the state parameters (e.g. when tracking cardiac or respiratory motion), increasing the weight on the dynamic model will likely play a more important role during tracking.

### 7.5.2 In vivo validation experiment

The steady-state error in the online SP-Nav/EKF motion estimates was quantified in vivo using real biological staged head motions (Fig. 7.8). In general, the accuracy of the in vivo estimates scaled with the magnitude of motion, with larger head motions leading to larger estimation errors. However, these errors were consistently less than one tenth of the overall magnitude, even for trials that included large compound motions with rotations over 15 deg (Fig. 7.8b and c). While the accuracy of the estimates from a single SP-Nav could not be assessed in vivo, an inspection of the tracking results suggests that the steady-state level of accuracy was reached in about 2-3 SP-Navs, consistent with the offline simulation results (c.f. insert in Fig. 7.8a). It should be noted that the range of motion magnitudes tested in this study was more than double the range used to benchmark the orbital (14), spherical (15) and cloverleaf (18) methods and yet in all trials the error never exceed the 10% level for any parameter and was typically well below this mark. It should also be noted that our validation procedure focused on motions that are more “likely” to be experienced in practice, given the nature of the scanner environment. Thus, not all parameters were tested to an equal extent during the validation experiment because the head coil itself limited some types of motions

from being performed. This is evidenced by the fact that the subject made larger rotations versus translations during the validation experiment (c.f. “true” motion in gray in Fig. 7.8c).

### 7.5.3 Repeated staged motion experiment

Results from the repeated staged motion experiment demonstrated the effectiveness of the SP-Nav/EKF framework for reducing periodic “nodding” and “side-to-side” head motion artifacts in both the 3D IR-SPGR and 3D FSE sequences (Fig. 7.10). Because the EKF was “tuned” to estimate rigid-body motion within the brain ROI, areas outside this region were ignored and subsequently uncorrected in the final images. This is illustrated in Fig. 7.11, which shows a close-up of the PROMO ON 3D IR-SPGR scan during “nodding” motion and the NO MOTION 3D IR-SPGR scan. The area highlighted with a white arrow in the figure corresponds to a region in the neck outside the brain ROI that is uncorrected in the image.

### 7.5.4 Real life experiment

The results from the real life experiments on the two healthy young males again demonstrated the overall effectiveness of the SP-Nav/EKF framework for significantly reducing 3D rigid-body head motion artifacts in 3D IR-SPGR scans under real life conditions (Fig. 7.12). Qualitatively similar motion statistics, as quantified using the “rescan metric” $\rho(n)$, suggests that the improvement in image quality was not due to an overall difference in the level of motion between the two scans (Fig. 7.12).

### 7.5.5 Advantages / limitations

The image-based SP-Nav/EKF tracking framework implemented in this study offers several advantages over existing *k*-space-based orbital (14), spherical (15) and cloverleaf navigator techniques (18). All *k*-space-based navigator methods require precise and reproducible *k*-space sampling trajectories from shot-to-shot such that rotations and translations in image-space can be estimated from *k*-space magnitude and phase information, respectively. Consequently, any effect that violates the assumptions of this Fourier model, such as 1) off-resonance due to magnetic field inhomogeneities and susceptibility differences, 2) gradient instabilities and 3) non-rigid motion of the object, will degrade the accuracy and precision of *k*-space-based rigid-body motion estimates. The SP-Navs, on the other hand, provide reduced sensitivity to motion estimation inaccuracies due to off-resonance by blurring these effects equally in all directions in image-space. Moreover, tracking in image-space allows for masking areas of the object that may corrupt the rigid-body motion estimates. In this study, we show how the EKF can be "tuned" during the "dummy" acquisition period to prevent non-rigid motion of the neck and jaw from corrupting the rigid-body estimates of the brain and skull. This type of masking using a *k*-space-based approach is difficult and requires tuning the RF pulse to excite only the rigid-body tissue component (s). However, although the motion estimates from a single SP-Nav have reduced sensitivity to off-resonance, any slow change in SP-Nav image quality over time due to scanner instabilities or time-varying off-resonance effects will corrupt the SP-Nav rigid-body motion estimates and ultimately reduce the quality of the final reconstructed images.

In terms of time requirements, a single 3-plane SP-Nav can be collected and reconstructed in approximately the same time (48 ms) as a 3-plane orbital navigator (33 ms) (14) and spherical navigator (27 ms) (15), but requires substantially more time than a single

cloverleaf (4.2 ms) (18). Therefore, the cloverleaf method may be advantageous in certain steady-state sequences where there is no intrinsic sequence "dead time" for navigator acquisition. However, in non-steady-state sequences such as 3D IR-SPGR and 3D FSE, a train of SP-Navs can be played out during the intrinsic $T_1$ recovery period of the acquisition without adding to the overall scan time. However, no motion correction is performed during the imaging segment itself, which typically lasts about 2 s. To account for this, corrupted *k*-space segments were rescanned at the end of the sequence depending on whether an online "rescan metric" exceeded a user-specified threshold. In this study, all in vivo scans were performed using a rescan threshold of $T = 1$, derived empirically from repeated no motion scans. This type of rescan procedure should be generally acceptable in most clinical applications, given that the number of rescanned *k*-space segments for the two young (and fairly uncooperative) males who participated in this study only resulted in an additional scan time of 50 s (Subject 1) and 90 s (Subject 2), respectively.

One limitation of the EKF tracking algorithm, as implemented in this study, is the inability to correct (rather than just ignore) non-rigid motion. In principle, however, one can augment the EKF state vector to include higher order motion parameters for nonlinear motion tracking. Velocity and acceleration terms can also be incorporated in the dynamic model when more rapid measurement information is available. For example, Sprincemaille et al. recently applied the linear Kalman filter with first-order constant velocity (CV) dynamics for rapid (~15 ms) real-time separation of cardiac and respiratory waveforms from navigator least-squares motion estimates (30). In general, the flexibility afforded by the dynamic state-space model framework of the EKF should allow for online image-based tracking of many different body parts using various types of measurements including 2D slice information for self-navigated tracking in EPI time-series data (25).

### 7.5.6 Summary

In summary, the results presented in this paper demonstrate the effectiveness of the PROMO motion correction technique for significantly reducing 3D rigid-body motion artifacts prospectively in high-resolution 3D scans. While the current implementation focused on spiral-navigated 3D IR-SPGR and 3D FSE scans, the flexible image-based EKF tracking procedure in PROMO may be useful in other applications such as self-navigated prospective motion correction in 2D EPI time-series data.

## 7.6 Appendix

To describe the online first order iterated EKF algorithm for prospective motion correction in the scanner sequence, let $M(\mathbf{x})$ be a 4 x 4 affine transform matrix that is parameterized by the state variable $\mathbf{x} = [t_x, t_y, t_z, \theta_x, \theta_y, \theta_z]^T$

$$\mathbf{M}(\mathbf{x}) = \mathbf{T}(\mathbf{x})\mathbf{R}(\mathbf{x}), \qquad [7.11]$$

Where

$$\mathbf{T}(\mathbf{x}) = \begin{bmatrix} 1 & 0 & 0 & t_x \\ 0 & 1 & 0 & t_y \\ 0 & 0 & 1 & t_z \\ 0 & 0 & 0 & 1 \end{bmatrix}, \qquad [7.12]$$

and

$$\mathbf{R}(\mathbf{x}) = \begin{bmatrix} c_y c_z & c_y c_z & s_y & 0 \\ -s_x s_y c_z - c_x s_z & -s_x s_y c_z + c_x c_z & s_x c_z & 0 \\ -c_x s_y c_z + s_x s_z & -c_x s_y c_z - s_x c_z & c_x c_y & 0 \\ 0 & 0 & 0 & 1 \end{bmatrix} \quad [7.13]$$

and $c_x$, $c_y$ and $c_z$ are the cosines and $s_x$, $s_y$ and $s_z$ are the sines of the parameters $\theta_x$, $\theta_y$ and $\theta_z$, respectively. Furthermore, let $X; \mathbb{R}^{4\times4} \rightarrow \mathbb{R}^{6\times1}$ be a function which describes the inverse mapping between the affine transform matrix $\mathbf{M}(\mathbf{x})$ and the state vector **x**

$$X\left(\mathbf{M}(\mathbf{x})\right) = \begin{bmatrix} m_{14} \\ m_{24} \\ m_{34} \\ \sin^{-1}(m_{13}) \\ \text{atan2}(m_{23}/\cos(\theta_y), m_{33}/\cos(\theta_y)) \\ \text{atan2}(m_{12}/\cos(\theta_y), m_{11}/\cos(\theta_y)) \end{bmatrix}, \quad [7.14]$$

where $m_{ij}$ is the *ij*-th entry of $\mathbf{M}(\mathbf{x})$ and atan2 is the four quadrant inverse tangent.

Now let $\mathbf{x}_0 = \begin{bmatrix} 0 & 0 & 0 & 0 & 0 & 0 \end{bmatrix}^T$ be the initial state of the EKF at time $k = 0$ and $\mathbf{y}_{\text{ref}} = \text{h}(\mathbf{x}_0)$ be the initial fixed reference SP-Nav. In the ideal online correction scenario, the affine transform matrix $\mathbf{M}(\hat{\mathbf{x}}_{k|k-1})$ associated with the predicted state $\hat{\mathbf{x}}_{k|k-1}$ is then used to update the scanner pulse-sequence at each time-step prior to collecting the measurements $\mathbf{y}_k$. However, to generalize the method in case this condition is not met (e.g., if real-time

communication is interrupted or the previous corrected state $\hat{\mathbf{x}}_{k-1|k-1}$ is not obtained in the time allowed), let $\mathbf{x}_k^{\text{app}}$ be the actual "applied" state used to collect $\mathbf{y}_k$. Now, let ${}^{+}\hat{\mathbf{x}}_{k|k-1} = X\left(\mathbf{M}^{-1}\left(\mathbf{x}_k^{\text{app}}\right)\cdot\mathbf{M}\left(\hat{\mathbf{x}}_{k|k-1}\right)\right)$ be the "adjusted" state that takes into account the potential mismatch between the predicted and "applied" state at time-step *k*. When the predicted state is equal to the "applied" state at each time-step, the "adjusted" state is simply the initial state $\mathbf{x}_0$.

The goal of EKF *correction* is to use the measurements $\mathbf{y}_k$ to refine the predicted state $\hat{\mathbf{x}}_{k|k-1}$ and error covariance $\hat{\mathbf{P}}_{k|k-1}$ at each time-step. Recall, this is accomplished by minimizing the cost

$$C_i\left(\mathbf{x}_k\right) = \left(\mathbf{y}_k - \mathrm{h}\left(\mathbf{x}_k\right)\right)^T \mathbf{R}^{-1}\left(\mathbf{y}_k - \mathrm{h}\left(\mathbf{x}_k\right)\right) + \left(\mathbf{x}_k - \hat{\mathbf{x}}_{k|k-1}^i\right)^T \hat{\mathbf{P}}_{k|k-1}^{-1}\left(\mathbf{x}_k - \hat{\mathbf{x}}_{k|k-1}^i\right), \quad [7.15]$$

using $i = 0, 1, \ldots, N$ iterations. The first order iterated EKF (Gauss-Newton) solution to such an optimization problem is the following update function

$$\hat{\mathbf{x}}_{k|k-1}^{i+1} = \hat{\mathbf{x}}_{k|k-1} + \mathbf{K}_i\left(\mathbf{y}_k - \mathrm{h}\left({}^{+}\hat{\mathbf{x}}_{k|k-1}^i\right) - \mathbf{H}_i\left(\hat{\mathbf{x}}_{k|k-1} - {}^{+}\hat{\mathbf{x}}_{k|k-1}^i\right)\right), \quad [7.16]$$

where ${}^{+}\hat{\mathbf{x}}_{k|k-1}^i = X\left(\mathbf{M}^{-1}\left(\mathbf{x}_k^{\text{app}}\right)\cdot\mathbf{M}\left(\hat{\mathbf{x}}_{k|k-1}^i\right)\right)$, $\mathbf{H}_i$ is the Jacobian of the measurement function $\mathrm{h}(\cdot)$ evaluated at the "adjusted" state ${}^{+}\hat{\mathbf{x}}_{k|k-1}^i$, and $\mathbf{K}_i = \left(\mathbf{H}_i\mathbf{R}^{-1}\mathbf{H}_i^T + \hat{\mathbf{P}}_{k|k-1}\right)^{-1}\mathbf{H}_i^T\mathbf{R}^{-1}$ is the Kalman gain. Details of the derivation of Eq. [7.16] is provided in many texts including Ref. (23) and is omitted here due to space constraints. At the end of all iterations, the *a posteriori*

state $\hat{\mathbf{x}}_{k|k}$ is set to ${}^{+}\hat{\mathbf{x}}_{k|k-1}^{N+1}$ and the *a posteriori* covariance $\hat{\mathbf{P}}_{k|k}$ is set to $\left(\mathbf{I}-\mathbf{K}_{N+1}\mathbf{H}_{N+1}\right)\hat{\mathbf{P}}_{k|k-1}$. Note, when no iterations are performed (i.e. $N = 0$) Eq. [7.16] reduces to the standard EKF. It should also be noted that when predicted state is equal to the "applied" state at each time-step and $N = 0$, the Jacobian $\mathbf{H}_i$ is always evaluated around the initial state $\mathbf{x}_0$ and thus can be calculated once and stored in memory.

To describe the details of the measurement function $\mathrm{h}(\cdot)$, let $y_{ax}$, $y_{sa}$ and $y_{co}$ be the respective 2D axial, sagittal and coronal images of the concatenated reference navigator vector $\mathbf{y}_{\mathrm{ref}} = \left[\mathrm{vec}(y_{ax})^T \quad \mathrm{vec}(y_{sa})^T \quad \mathrm{vec}(y_{co})^T\right]^T$, where the operator $\mathrm{vec}(\cdot);\mathbb{R}^{m\times m} \rightarrow \mathbb{R}^{2m\times 1}$ concatenates a 2D matrix into a 1D vector. Furthermore, let $\mathbf{r}_{\mathrm{ax}}$, $\mathbf{r}_{\mathrm{sa}}$, and $\mathbf{r}_{\mathrm{co}}$ be 4 x M matrices of initial (homogenous) voxel coordinates for $y_{ax}$, $y_{sa}$ and $y_{co}$, respectively. Then, the measurement function $\mathrm{h}(\mathbf{x})$ can be written

$$\mathrm{h}(\mathbf{x}) = \begin{bmatrix} \mathrm{vec}\left(y_{\mathrm{ax}}\left(\mathbf{P}_{\mathrm{ax}}\cdot\mathbf{M}(\mathbf{x})\cdot\mathbf{r}_{\mathrm{ax}}\right)\right) \\ \mathrm{vec}\left(y_{\mathrm{sa}}\left(\mathbf{P}_{\mathrm{sa}}\cdot\mathbf{M}(\mathbf{x})\cdot\mathbf{r}_{\mathrm{sa}}\right)\right) \\ \mathrm{vec}\left(y_{\mathrm{co}}\left(\mathbf{P}_{\mathrm{co}}\cdot\mathbf{M}(\mathbf{x})\cdot\mathbf{r}_{\mathrm{co}}\right)\right) \end{bmatrix}, \qquad [7.17]$$

where $\mathbf{P}_{\mathrm{ax}} = \mathrm{diag}\left([1 \quad 1 \quad 0 \quad 1]^T\right)$, $\mathbf{P}_{\mathrm{sa}} = \mathrm{diag}\left([0 \quad 1 \quad 1 \quad 1]^T\right)$ and $\mathbf{P}_{\mathrm{co}} = \mathrm{diag}\left([1 \quad 0 \quad 1 \quad 1]^T\right)$ are matrices which project the transformed 3D homogenous coordinates onto the respective planes of the reference prior to interpolation. In this study, 2D linear interpolation was used throughout.

## 7.7 Acknowledgements

Funding for this work was provided by GE Healthcare Inc. and the following NIH grants: 1R01AG031224, 1U01AG024904-02, 5 U24 RR021382-04, U54 NS056883-01. Chapter 7, in full, is a reprint of the material as it will appear in the January issue of Magnetic Resonance in Medicine, 2010, entitled: *PROMO: Real-time Prospective Motion Correction in MRI using Image-based Tracking.* Nathan White, Cooper Roddey, Ajit Shankaranarayanan, Eric Han, Dan Rettmann, Juan Santos, Josh Kuperman, and Anders Dale. The dissertation author was the primary investigator and first author of this paper.

## 7.8 References

1. Hajnal JV, Myers R, Oatridge A, Schwieso JE, Young IR, Bydder GM. Artifacts due to stimulus correlated motion in functional imaging of the brain. Magn Reson Med 1994;31(3):283-291.

2. Friston KJ, Williams S, Howard R, Frackowiak RS, Turner R. Movement-related effects in fMRI time-series. Magn Reson Med 1996;35(3):346-355.

3. Cox RW, Jesmanowicz A. Real-time 3D image registration for functional MRI. Magn Reson Med 1999;42(6):1014-1018.

4. Friston KJ, Ashburner J, Frith C, Poline JB, Heather JD, Frackowiak RSJ. Spatial Registration and Normalization of Images. Human Brain Mapping 1995;2:165-189.

5. Jenkinson M, Smith S. A global optimisation method for robust affine registration of brain images. Med Image Anal 2001;5(2):143-156.

6. Korin HW, Felmlee JP, Ehman RL, Riederer SJ. Adaptive technique for three-dimensional MR imaging of moving structures. Radiology 1990;177(1):217-221.

7. Ehman RL, Felmlee JP. Adaptive technique for high-definition MR imaging of moving structures. Radiology 1989;173(1):255-263.

8. Liu C, Bammer R, Kim DH, Moseley ME. Self-navigated interleaved spiral (SNAILS): application to high-resolution diffusion tensor imaging. Magn Reson Med 2004;52(6):1388-1396.

9. Pipe JG. Motion correction with PROPELLER MRI: application to head motion and free-breathing cardiac imaging. Magn Reson Med 1999;42(5):963-969.

10. Firmin D, Keegan J. Navigator echoes in cardiac magnetic resonance. J Cardiovasc Magn Reson 2001;3(3):183-193.

11. Norris DG, Driesel W. Online motion correction for diffusion-weighted imaging using navigator echoes: Application to RARE imaging without sensitivity loss. Magn Reson Med 2001;45(5):729-733.

12. Weih KS, Driesel W, von Mengershausen M, Norris DG. Online motion correction for diffusion-weighted segmented-EPI and FLASH imaging. Magma 2004;16(6):277-283.

13. Fu ZW, Wang Y, Grimm RC, Rossman PJ, Felmlee JP, Riederer SJ, Ehman RL. Orbital navigator echoes for motion measurements in magnetic resonance imaging. Magn Reson Med 1995;34(5):746-753.

14. Ward HA, Riederer SJ, Grimm RC, Ehman RL, Felmlee JP, Jack CR, Jr. Prospective multiaxial motion correction for fMRI. Magn Reson Med 2000;43(3):459-469.

15. Welch EB, Manduca A, Grimm RC, Ward HA, Jack CR, Jr. Spherical navigator echoes for full 3D rigid body motion measurement in MRI. Magn Reson Med 2002;47(1):32-41.

16. Irarrazabal P, Nishimura DG. Fast three dimensional magnetic resonance imaging. Magn Reson Med 1995;33(5):656-662.

17. Wong ST, Roos MS. A strategy for sampling on a sphere applied to 3D selective RF pulse design. Magn Reson Med 1994;32(6):778-784.

18. van der Kouwe AJ, Benner T, Dale AM. Real-time rigid body motion correction and shimming using cloverleaf navigators. Magn Reson Med 2006;56(5):1019-1032.

19. Thesen S, Heid O, Mueller E, Schad LR. Prospective acquisition correction for head motion with image-based tracking for real-time fMRI. Magn Reson Med 2000;44(3):457-465.

20. Zaitsev M, Dold C, Sakas G, Hennig J, Speck O. Magnetic resonance imaging of freely moving objects: prospective real-time motion correction using an external optical motion tracking system. Neuroimage 2006;31(3):1038-1050.

21. Speck O, Hennig J, Zaitsev M. Prospective real-time slice-by-slice motion correction for fMRI in freely moving subjects. Magma 2006;19(2):55-61.

22. Dold C, Zaitsev M, Speck O, Firle EA, Hennig J, Sakas G. Prospective head motion compensation for MRI by updating the gradients and radio frequency during data acquisition. Med Image Comput Comput Assist Interv Int Conf Med Image Comput Comput Assist Interv 2005;8(Pt 1):482-489.

23. Gelb A. Applied Optimal Estimation: MIT Press; 1974.

24. Kalman RE. A New Approach to Linear Filtering and Prediction Problems. Transactions of the ASME--Journal of Basic Engineering 1960;82(Series D):35-45.

25. White NS, Shankaranarayanan A, Han ET, Gaddipati A, Roddey C, Dale A. Prospective motion correction using nonlinear predictive filtering. In: Proceedings of the 15th Annual Meeting of the ISMRM; 2007; Berlin, Germany.

26. Shankaranarayanan A, Han ET, Roddey C, White N, Kuperman J, Santos J, Rettmann D, Schmidt E, Dale A. Motion insensitive 3D T2 and T1-weighted imaging with a real-time, image-based PROspective MOtion correction technique (3D PROMO) and automated re-acquisition of motion-corrupted k-space segments. In: Proceedings of the 16th Annual Meeting of the ISMRM; 2008; Toronto, Canada.

27. Shankaranarayanan A, Roddey C, White N, Han ET, Rettmann D, Santos J, Schmidt E, Dale A. Motion insensitive 3D imaging using a novel real-time image-based 3D PROspective MOtion correction method (3D PROMO). In: Proceedings of the 15th Annual Meeting of the ISMRM; 2007; Berlin, Germany.

28. Roddey C, Shankaranarayanan A, Han ET, White N, Dale A. Motion insensitive imaging using 3D PROspective MOtion (PROMO) correction with region-of-interest tracking.; 2008; Toronto, Canada. Berkeley, USA:ISMRM.

29. Keating B, Roddey J, Deng W, Dale A, White N, Stenger V, Ernst T. 3-D Prospective Motion Correction for MR Spectroscopy. In: 17th Annual Meeting of the ISMRM; 2009; Honolulu, HI.

30. Spincemaille P, Nguyen TD, Prince MR, Wang Y. Kalman filtering for real-time navigator processing. Magn Reson Med 2008;60(1):158-168.

31. Lin C, Bernstein MA. 3D magnetization prepared elliptical centric fast gradient echo imaging. Magn Reson Med 2008;59(2):434-439.

32. Busse RF, Hariharan H, Vu A, Brittain JH. Fast spin echo sequences with very long echo trains: design of variable refocusing flip angle schedules and generation of clinical T2 contrast. Magn Reson Med 2006;55(5):1030-1037.

33. Santos JM, Graham AW, Pauly JM. Flexible Real-Time Magnetic Resonance Imaging Framework. In: EMBS PottAICI, editor; 2004; San Fransicso, CA.

34. Santos JM, Cunningham CH, Lustig M, Hargreaves BA, Hu BS, Nishimura DG, Pauly JM. Single breath-hold whole-heart MRA using variable-density spirals at 3T. Magn Reson Med 2006;55(2):371-379.

35. Bell BM, Cathey FW. The iterated Kalman filter update as a Gauss-Newton method. IEEE Trans Automatic Control 1993;38(2):294-297.

# Chapter 8

# Future Directions: Restriction Spectrum Imaging

## 8.1 Introduction

Diffusion tensor imaging (DTI) (1) is a powerful non-invasive technique for studying brain tissue microstructure *in vivo*. However, a well-known limitation of DTI is the inability to characterize diffusion in complex tissue microstructures (2). Recently, model-based deconvolution techniques have become increasingly popular for resolving multiple fiber orientations in heterogeneous fiber populations (3-6). However, these methods rely on the assumption that the tissue is composed of fibers with identical water restriction properties (i.e. morphology and size scale). Here, we propose a new model-based analysis approach for multiple b-value acquisitions called Restriction Spectrum Imaging (RSI). RSI relaxes the assumption above and models the tissue using a spectrum of both oriented and non-oriented tissue components with different water restriction scales.

## 8.2 Methods

### 8.2.1 Data acquisition

An excised adult male Sprague-Dawley rat brain was immersed for 4 weeks in a 4°C 1mM GdDTPA solution and positioned in a sealed plastic tube filled with Fomblin liquid. Scanning was performed using a 4.7T Bruker scanner equipped with a 3 cm solenoid receiver coil. Pulse-sequence parameters: TR/TE = 650/49 msec, Δ/δ = 23/12 msec, 515 **q**-space directions, $|G|_{max}$ = 380 $mTm^{-1}$, matrix = 64x64x128, 265 μm isotropic voxels, b-max ~32,000 $mm^2$/sec. However, for this study only 123 **q**-space directions were used with b-max = 10,000 $mm^2$/sec. Myelin stained histological sections were obtained and registered to the MRI data as described previously (7).

### 8.2.2 RSI model

Recall, under the linear convolution model the measured diffusion signal in each voxel $S(b,\mathbf{r})$ can be written

$$\frac{S(b,\mathbf{r})}{S_0} = \int R(b,\mathbf{r},\mathbf{x})\, f(\mathbf{x}) d\mathbf{x} + n(b,\mathbf{r}), \qquad [8.1]$$

where $b$ is the diffusion weighting factor, or "b-value", $\mathbf{r}$ is a unit (column) vector indicating the direction of the applied diffusion gradient, $S_0$ is the signal measured with no diffusion weighting (i.e. $S_0 \equiv S(b=0)$), $R(\cdot,\cdot,\mathbf{x})$ is the signal response to a single *ideal* fiber with orientation given by the unit (column) vector $\mathbf{x}$, $f(\cdot)$ is a real-valued function of the unit

sphere describing the fiber orientation density (FOD), and $n(b,\mathbf{r})$ is additive measurement noise.

In RSI, an axially symmetric tensor model (8) is used to characterize diffusion at multiple microscopic length scales. Under this model, the measured diffusion signal can then be written

$$\frac{S(b,\mathbf{r})}{S_0} = \int_{\lambda_\perp}\int_{\mathbf{x}} R(b,\mathbf{r},\lambda_\perp,\mathbf{x}) f(\mathbf{x},\lambda_\perp)\, d\mathbf{x} d\lambda_\perp + e^{-b\lambda_0} + n(b,\mathbf{r}), \qquad [8.2]$$

where $R(\mathbf{q}_i,\lambda_\perp,\mathbf{x}_j) = \exp(-b_i\lambda_\perp)\cdot\exp(-b_i((\lambda_{\|}-\lambda_\perp)(\mathbf{r}_i\cdot\mathbf{x}_j)^2)$ is the signal response with perpendicular and parallel diffusivities $\lambda_\perp$ and $\lambda_{\|}$, respectively, and $\lambda_0$ is the diffusivity of the "free" water component. Note the additional summation over $\lambda_\perp$ in Eq. 8.2, which allows the perpendicular diffusivity to vary across microscopic length scales.

### 8.2.3 Estimation

To fit the model above, we discretize the signal equation using P restriction scales $\lambda_\perp = \{\lambda_1,\lambda_2,...,\lambda_P\}$ and use a spherical harmonic (SH) parameterization for the fiber orientation function $f(\mathbf{x}) = \sum^K \beta_k Y_k(\mathbf{x})$. This leads to a simple linear model of the normalized signal $\mathbf{S} = \left[\mathbf{R}(\lambda_1) \quad \mathbf{R}(\lambda_2) \quad \cdots \quad \mathbf{R}(\lambda_P) \quad e^{-\mathbf{b}\lambda_0}\right]\boldsymbol{\beta} + \mathbf{n}$, where the *ik*-th element of the matrix $\mathbf{R}(\lambda_j)$ is $\mathbf{R}_{ik}(\lambda_j) = \int R(\mathbf{q}_i,\lambda_j,\mathbf{x})Y_k(\mathbf{x})d\mathbf{x}$ and the parameter vector $\boldsymbol{\beta}$ has $(K\times P)+1$ elements.

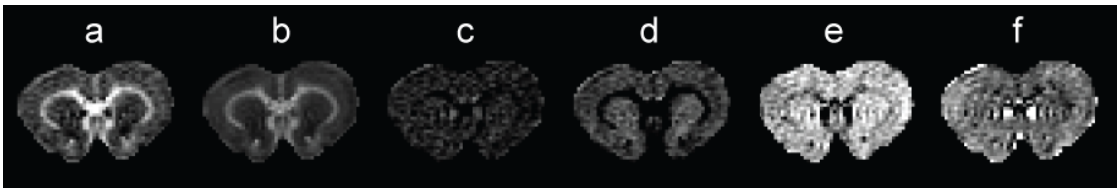


**Figure 8.1.** RSI restriction maps showing the volume fraction of spins at different microscopic length (restriction) scales (from left to right in mm$^2$ /sec). (a) $\lambda_\perp = 1\times10^{-5}$, (b) $\lambda_\perp = 2.4\times10^{-5}$, (c) $\lambda_\perp = 5.8\times10^{-5}$, (d) $\lambda_\perp = 1.4\times10^{-4}$, (e) $\lambda_\perp = \lambda_{||}$ (tissue isotropic), and (f) $\lambda_0 = 2\lambda_{||}$ (free water). Images (a-d) have oriented structure, while (e,f) are isotropic.

Here, we use a maximum SH order of 4 (thus $K = 15$), set $\lambda_{||} = 3.4\times10^{-4}$ mm$^2$/sec (which was estimated from the data), $\lambda_0 = 2\lambda_{||}$, and use 5 restriction scales for $\lambda_\perp$ (P = 5). Maximum a posteriori estimates of the parameters $\boldsymbol{\beta}$ were obtained using Tikhonov regularization.

## 8.3 Preliminary Results

RSI "restriction maps" showing the volume fraction of spins at various microscopic length (restriction) scales are shown in Fig. 8.1 for a coronal slice through the genu of the corpus callosum. Maps correspond to the 0-th order (isotropic) SH parameter estimates, normalized to sum to 1. The first 4 images (a-d) correspond to oriented diffusion, while the last 2 images (e,f) correspond to isotropic diffusion. Note, highly restricted spins at fine microscopic length scales are predominantly located in white matter (a,b), while spins at courser length scales are mainly seen in gray matter (d). Also, note the separation between the tissue isotropic (e) and free water spins (f). Fiber orientation distributions (FODs) at each restriction scale can also be estimated with RSI using the higher order SH. An example of this is shown in Fig. 8.2 at corresponding scales to those in Fig. 8.1 (a-d). FOD reconstructions are shown for a single voxel in the striatum (c) along with corresponding myelin stain images showing the striated myeloarchitecture in this region (d). Note that the fiber orientation is

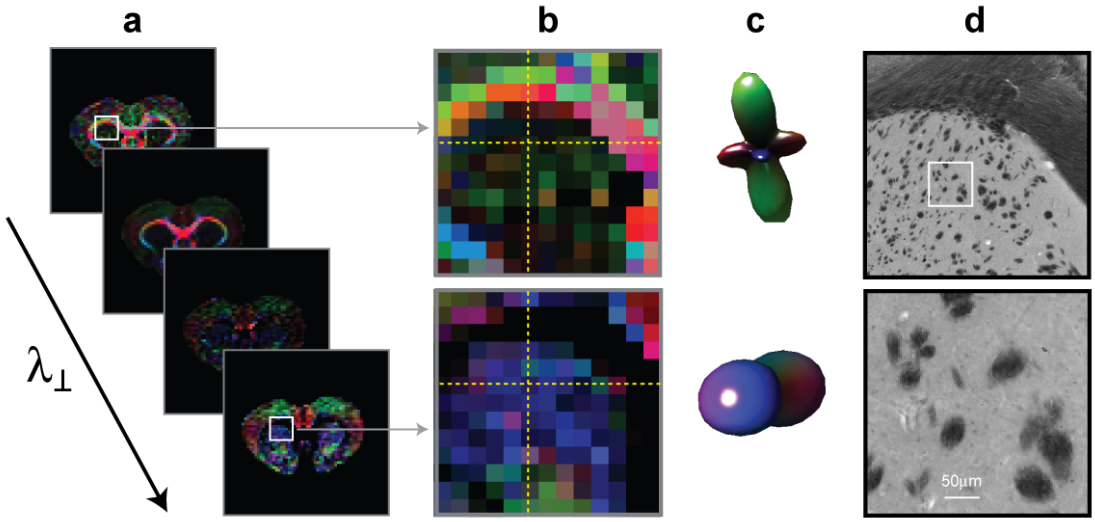


**Figure 8.2.** RSI direction maps for the oriented diffusion components. (a) RGB colormaps indicating the primary fiber direction (FOD maximum) at each restriction scale. (b) close-up sections of the striatum for the highest (top) and lowest (bottom) restriction levels. (c) 3D fiber-orientation distributions (FODs) for the voxel highlighted in (b) with the FOD corresponding to the highest restriction scale on top and the lowest restriction scale on bottom. (d) histological section images showing the corresponding myeloarchitecture in this region.

dependent on the restriction scale with mainly mediolateral and anterioposterior directionality for the highest restriction scale (top row) and rostro-caudal (through-plane) orientation for the lowest restriction scale (bottom row). This may potentially reflect separated spin diffusion in and around striatal gray and white matter compartments.

## 8.4 Discussion

Restriction spectrum imaging (RSI), presented here, is a new model-based analysis strategy for multiple b-value acquisitions designed to differentiate tissue components with dissimilar morphologies and size scales on the basis of their water diffusion characteristics. Both volume fraction and orientation information can be extracted at each microscopic length/restriction scale using simple linear estimation methods. As such, RSI provides a new computationally efficient framework for studying complex neuroarchitectures in the brain and

may allow for improved *in vivo* characterization of neuromorphology in healthy and pathological tissue. Diffusion at the finest length scale most likely stems from the restricted water pool within the intracellular space, while diffusion at courser length scales most likely stems from hindered diffusion in the extracellular space representative of the intrinsic tourtosity. Current work is focused on validating these later claims and studying the conditions under which intracellular/restricted water is sufficiently modeled with a diffusion tensor.

## 8.5 Acknowledgements

Funded by grants from the NIH (R01-EB00790, U24-RR021382) and the Norwegian Research Council. Chapter 8, in full, is part of a presentation at the 17th Annual Meeting of the International Society of Magnetic Resonance in Medicine (ISMRM) in 2009, entitled: *"Restriction Spectrum Imaging (RSI): A New Approach for Resolving Complex Tissue Microstructures with Diffusion MRI"*, Nathan White, Trygve B. Leergaard, Alex de Crespigny, and Anders Dale. The dissertation author was the primary investigator and first author of this abstract, and the material is currently being prepared for submission for publication.

## 8.6 References

1. Basser PJ, Mattiello J, LeBihan D. Estimation of the effective self-diffusion tensor from the NMR spin echo. J Magn Reson B 1994;103:247-254.

2. Le Bihan D, Poupon C, Amadon A, Lethimonnier F. Artifacts and pitfalls in diffusion MRI. J Magn Reson Imaging 2006;24(3):478-488.

3. Alexander DC. Maximum entropy spherical deconvolution for diffusion MRI. Inf Process Med Imaging 2005;19:76-87.

4. Dell'Acqua F, Rizzo G, Scifo P, Clarke RA, Scotti G, Fazio F. A model-based deconvolution approach to solve fiber crossing in diffusion-weighted MR imaging. IEEE Trans Biomed Eng 2007;54:462-472.

5. Jian B, Vemuri BC. Multi-fiber reconstruction from diffusion MRI using mixture of Wisharts and sparse deconvolution. Inf Process Med Imaging 2007;20:384-395.

6. Tournier JD, Calamante F, Gadian DG, Connelly A. Direct estimation of the fiber orientation density function from diffusion-weighted MRI data using spherical deconvolution. Neuroimage 2004;23:1176-1185.

7. White NS, Leergaard TB, Bolstad I, Bjaalie JG, D'Arceuil H, de Crespigny A, Dale AM. Quantitative histological validation of fiber-orientation distributions based on high-angular resolution diffusion imaging.; 2008; Proc 16th Annual Meeting of the ISMRM, Toronto, Canada.

8. Hsu EW, Mori S. Analytical expressions for the NMR apparent diffusion coefficients in an anisotropic system and a simplified method for determining fiber orientation. Magn Reson Med 1995;34:194-200.

# Chapter 9

# Conclusion

## 9.1 Conclusion

The focus of this dissertation was to tackle some of the most pressing practical limitations for in vivo quantitative magnetic resonance imaging of the human brain. In Chapter 5, my colleagues and I presented what we believe to be the first direct quantitative histological validation of neuronal fiber orientation distributions in brain tissue. In this study we demonstrated that accurate fiber orientations can be extracted from diffusion MRI data with an intrinsic angular error of about 5 degrees. However, with that said, there remain some important questions left unanswered. For example, as the method employed for estimating fiber orientations (spherical deconvolution) relies on a model for the diffusion signal, to what extent to the results depend on the model assumptions? If we were to vary the assumed ADC, for example, could we get an even stronger match to the histoarchitecture. Also, how do other multi-directional diffusion MRI techniques such as Q-ball and Diffusion Spectrum Imaging stack up compared to spherical deconvolution? How do these techniques fair in more complex tissue architectures, for example in regions with three or more principle fiber orientations?

Having validated the diffusion MRI derived neuronal fiber orientations in Chapter 5, in Chapter 6 we presented a study into the optimal (maximally efficient) diffusion MRI

acquisition for in vivo quantification of the fiber orientation distribution. The results were again based on the assumption of a fixed ADC that were derived from in vivo measurements. If we were, however, to allow for a spectrum of ADCs to be fit to the data (i.e. the model presented in Chapter 8), what might be the optimal parameter settings for resolving the corresponding fiber orientations at the various microscopic length scales? Because, the spectrum model can also be formulated in a linear unbiased sense, a similar approach could in principle be used to derive the optimal combination of b-values and diffusion directions for fitting this more informed model.

In Chapter 8, a model for the diffusion MRI signal was presented which allows for a spectrum of neuronal fiber orientation distributions to be extracted from each voxel at various microscopic length scales. Although we fit for a range of different length-scales, we found that fiber orientations at two scales dominated: one at a fine length-scale with a corresponding slow ADC (i.e. restricted), and one at a course length-scale with a faster ADC consistent with the transport of water in the extracellular space. This finding is further consistent with a large body of evidence pointing to a multi-exponential (slow and fast) decay of the diffusion NMR signal in biological tissue samples. Taken together these findings suggest that one can in principle separate the orientation structure of the intra and extracellular water diffusion pools with their relative volume fractions. If so, some interesting inferences could be made. For example, the volume fraction of the intracellular component could be used to derive spatial maps of the cellular (fiber) density, a potentially valuable biomarker for studying various neural pathologies. Likewise the volume fraction and the specific ADC value at the course scale could provide insight into pathologies and physiological conditions affecting the tortuosity of diffusion in the extracellular space, such as cell swelling. However, future scientific study is needed to address these questions in more detail. In particular, as the

majority of these studies were conducted in ex vivo fixed tissue, it will be highly desirable to perform these investigations in the human brain in vivo. More sophisticated biophysical models taking into account cell permeability, axon diameters, and other structural and physiological properties will also likely play an important role in future diffusion MRI investigations of brain tissue microstructure, allowing researchers to ask the harder questions and possibly providing them with the tools necessary to help answer them.